π^0 ELECTROPRODUCTION OF THE $\Delta(1232)$ RESONANCE AT HIGH MOMENTUM TRANSFERRED

By

Maurizio Ungaro

A Thesis Submitted to the Graduate

Faculty of Rensselaer Polytechnic Institute

in Partial Fulfillment of the

Requirements for the Degree of

DOCTOR OF PHILOSOPHY

Major Subject: Physics

Approved by the
Examining Committee:

Paul Stoler, Thesis Adviser

Gary Adams, Member

James Napolitano, Member

Daniel Sperber, Member

Rensselaer Polytechnic Institute
Troy, New York

November 2003
(For Graduation December 2003)

π^0 ELECTROPRODUCTION OF THE $\Delta(1232)$ RESONANCE AT HIGH MOMENTUM TRANSFERRED

By

Maurizio Ungaro

An Abstract of a Thesis Submitted to the Graduate

Faculty of Rensselaer Polytechnic Institute

in Partial Fulfillment of the

Requirements for the Degree of

DOCTOR OF PHILOSOPHY

Major Subject: Physics

The original of the complete thesis is on file
in the Rensselaer Polytechnic Institute Library

Examining Committee:

Paul Stoler, Thesis Adviser

Gary Adams, Member

James Napolitano, Member

Daniel Sperber, Member

Rensselaer Polytechnic Institute
Troy, New York

November 2003
(For Graduation December 2003)

CONTENTS

LIST OF TABLES

LIST OF FIGURES

ACKNOWLEDGMENT

I would like to thanks my parents and my brother (I have to do it in italian): grazie mamma e papa' per la forza che continuamente mi avete trasmesso col vostro esempio e la vostra fede. Grazie anche per la pazienza che mi avete dimostrato in questi cinque anni. Robbi grazie per essere un grande uomo.

It's been an honor to have worked with my advisor Paul Stoler. It is an honor to share with him our passion for physics. He (and Janet) have also been my family here, close to me and helpful when it mattered the most.

I'd like to thank my friend Steve and the hockey bunch.

Thank you Kelly.

Thank you Rich.

Thanks Jimmy for the good time at the pubs.

I want to thank my friends Angela And Joachim and Mina and Matt.

Thanks to:

Valery

Elton

Stepan

Volker

Mark Ito

for their invaluable help.

Thanks to my friends Dennis and Christine for their support.

Thanks to the JLAB Computer Center.

CHAPTER 1
Single pion electroproduction

1.1 The unpolarized cross section formalism

The cross section for the unpolarized one-photon-exchange process, illustrated in Fig.1.1, can be written as

$$\frac{d\sigma}{dW dQ^2 d\Omega^*_{\pi^0}} = \Gamma \frac{d\sigma}{d\Omega^*_{\pi^0}}$$

where Γ is the virtual photon flux factor, and $\frac{d\sigma}{d\Omega^*_{\pi^0}}$ is the π^0 differential cross section due to virtual photons.

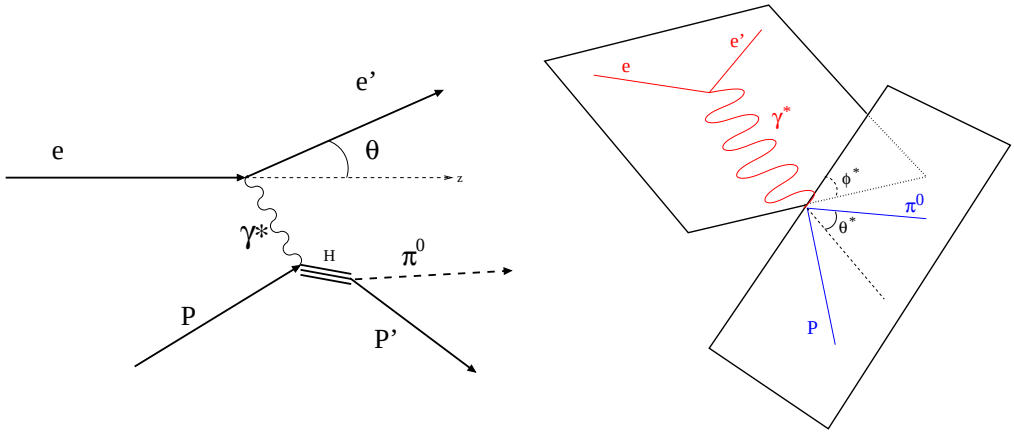

Figure 1.1: Schematics of π^0 electroproduction. The $z-axis$ is oriented along the beam line. On the right the definitions of the angles ϕ^* and θ^*.

The relevant 4-vectors are:

e_μ : incident electron, $e_\mu = (E, 0, 0, E)$. The beam energy for this experiment was $E = 5.754$ GeV.

e'_μ : scattered electron

P_μ : target (incident proton)[1], $P_\mu = (M_p, 0, 0, 0)$

P'_μ : scattered proton

q_μ : virtual photon, $q_\mu = e_\mu - e'_\mu$

H_μ : outgoing hadrons mass, $H_\mu = q_\mu + P_\mu$

x_μ : missing particle, $x_\mu = H_\mu - P'_\mu$

so that

$$\begin{aligned} W = \sqrt{\mathbf{H}^2} \quad &\leftarrow \text{ hadron invariant mass} \\ Q^2 = -\mathbf{q}^2 \quad &\leftarrow \text{ mass square of the virtual photon} \\ \epsilon = (1 + 2\frac{|\vec{q}|^2}{Q^2}\tan^2\frac{\theta}{2})^{-1} \quad &\leftarrow \text{ polarization of the virtual photon} \end{aligned}$$

Γ is the virtual photon flux

$$\Gamma(W, Q^2) = J(W, Q^2)\,\frac{\alpha}{2\pi^2}\frac{E'_e}{E_e}\frac{W^2 - M_p^2}{2M_p}\frac{1}{Q^2}\frac{1}{1-\epsilon} \tag{1.1}$$

J is the Jacobian for the variables transformation $(E_{e'}\,, \Omega_{e'}) \rightarrow (W\,, Q^2)$

$$J(W, Q^2) = \frac{\partial(W, Q^2)}{\partial(E_{e'}, \Omega_{e'})} = \frac{W}{2E_e E_{e'} M_p}$$

For unpolarized beam and target $\frac{d\sigma}{d\Omega^*_{\pi^0}}$can be factorized as follows:

$$\frac{d\sigma}{d\Omega^*_{\pi^0}} = \frac{2Wp^*_{\pi^0}}{W^2 - m_P^2}\left(\sigma_T + \epsilon_L\sigma_L + \epsilon\sigma_{TT}sin^2\theta^*_{\pi^0}cos2\phi^*_{\pi^0} + \sigma_{LT}\sqrt{2\epsilon_L(\epsilon+1)}sin\theta^*_{\pi^0}cos\phi^*_{\pi^0}\right)$$

where $*$ refers to c.m. quantities (i.e. $p^*_{\pi^0}$ is the momentum of π^0 in the center of mass).

[1] M_p is the mass of the proton.

CHAPTER 2
Experimental apparatus

The e1-6 experiment took place in the Hall-B of the **T**homas **J**efferson **N**ational **A**ccelerator **F**acilit (TJNAF). The **C**ontinuous **E**electron **B**eam **A**ccelerator **F**acility (CEBAF) provides an electron beam to three end stations (experimenta Hall A, B and C). The schematics of the accelerator and the experimental halls is illustrated in Figure 2.1.

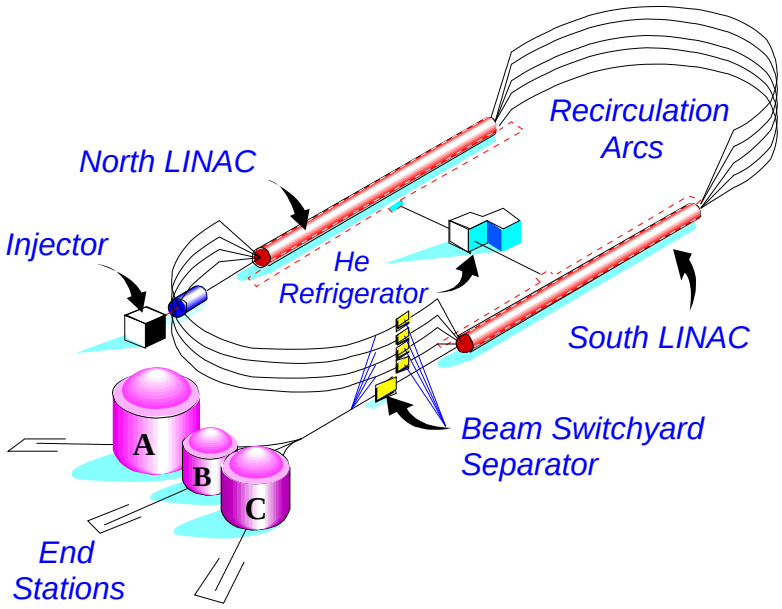

Figure 2.1: The CEBAF accelerator and the three experimental halls.

What follows is a description of the accelerator and the detector used in Hall-B.

2.1 CEBAF

CEBAF is composed (see Figure 2.1) by two identical linear accelerators (LINAC) and nine bending arcs, so that the beam is recirculated five times (2.8 miles) before being delivered to the halls.

The main characteristics of the accelerator are:

- Maximum energy of electron beam: ~ 6 GeV.
- duty-cicle: 100%
- geometric emittance: $< 10^{-9}$ mrad.
- momentum spread $\Delta p/p$ (4σ): 10^{-4}
- maximum beam current: 200 mA
- beam polarization: $\sim 70\%$.
- size of beam at the target: < 0.5 mm.

A 45 MeV electron beam is delivered in the accelerator by a superconductive RF injector. The beam is then accelerated in the LINAC by 20 superconducting radiofrequency cavities (SRF), each one composed by five cells whose average acceleration gradient of 10 Mev/meter.

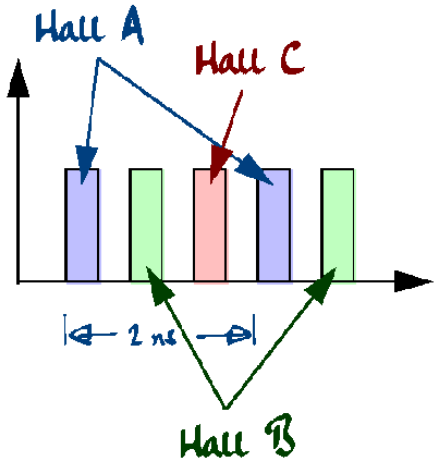

Figure 2.2: The beam delivery structure. Each hall get an electron bunch every 2 ns.

CEBAF can deliver to each hall an integer multiple of 1/4 of the final energy, because the beam can be extracted at each pass. The RF structure of the cavities

is 1.5 GHz and allows simltaneous electron bunches in all the halls in 2 ns intervals illustrated in Figure 2.2.

2.2 The CLAS detector

Inside Hall-B there is the **C**EBAF **L**arge **A**cceptance **S**pectometer (CLAS) shown in Figure 2.3. CLAS is divided in six identical and independent sectors. The azimuthal coverage of CLAS is nearly 4π while the polar acceptance ranges from 8^0 to 140^0 for charged particles and 8^0 to 45^0 for neutral particles.

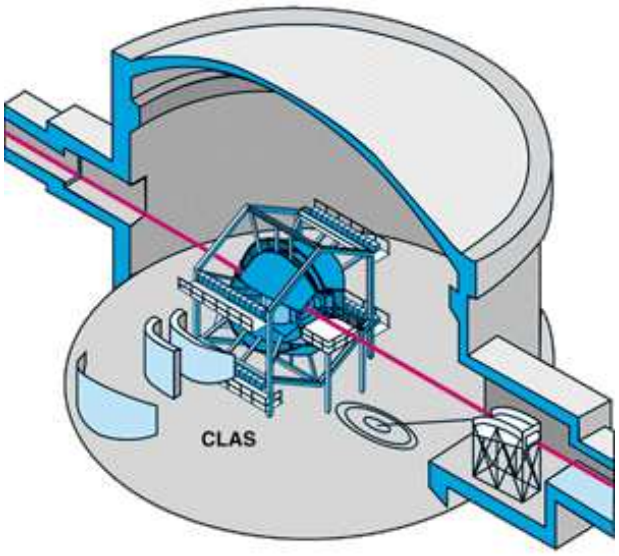

Figure 2.3: Section of Hall-B. The beam is represented by the red line. The hall diameter is 20 meters.

In Figure 2.4 are shown various components of CLAS. Charged particles are bent by a toroidal magnetic field which acts only on the polar angle, leaving the azimuthal angle unchanged.

In the e1-6 configuration Each sector was composed by:

- Three layers of Drift Chambers (DC), from 8^0 to 140^0, determine the trajec-

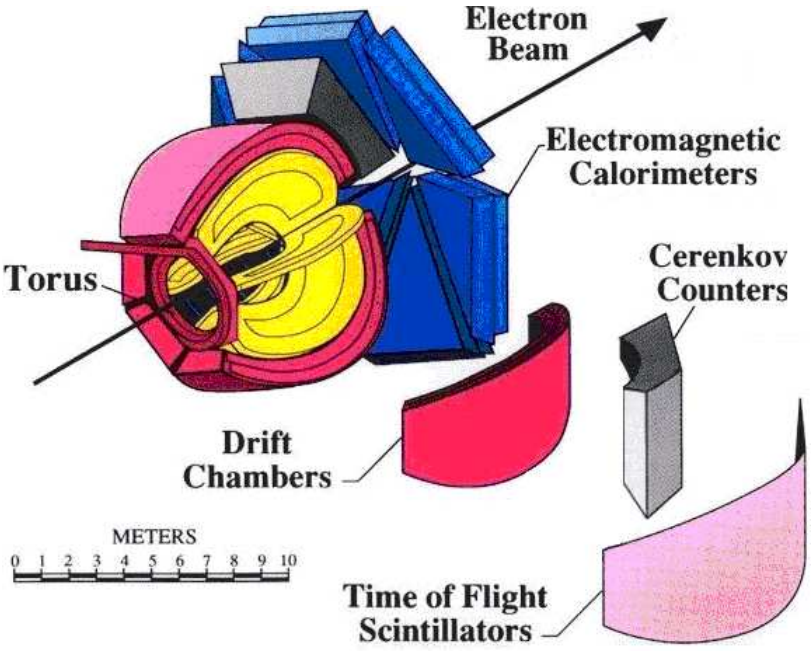

Figure 2.4: Section of Hall-B. The beam is represented by the red line. The hall diameter is 20 meters.

tories of charged particle, therefore their momentum using the curvature ρ in a known magnetic field:

$$B\rho = \frac{p}{q} \tag{2.1}$$

- A Čerenkov counter (CC), from 8^0 to 45^0, provide electrons/pions separation.
- A system of scintillator counters, 8^0 to 140^0, measure the Time Of Flight (TOF) of charged particles.
- An Electromagnetic Calorimeter (EC), from 8^0 to 45^0, is used for identifying electrons and neutral particles.
- A minitorus is used to direct the Møller electrons into the beam dump.

Each components is discussed below.

2.3 The torus magnet

The torus magnetic field allows momentum reconstruction by deflecting the charged particles according to (2.1). The toroidal configuration presents advantages illustrated in Table 2.1 if compared with the soleinoidal one (often used in e^+e^- colliders) or the dipolar one.

CONFIGURATION	SOLENOIDAL	DIPOLAR	TOROIDAL
	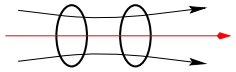	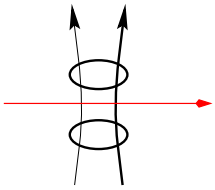	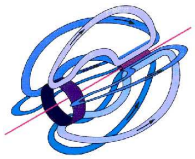
θ range	+	+	++
ϕ range	+++	- -	-
p resolution	- -	++	++
Particle identification	+	++	++
Zero field on target	- -	-	++
Open structure	- -	+	++

Table 2.1: Pro and con of three types of magnet configuration. The red line represents the beam.

The toroidal configuration can generate a magnetic field stronger in the forward region where the most energetic particles are detected, so that the momentum

resolution results homogeneous. It leaves a considerable amount of space (with zero magnetic field) around the target, which is important when the target comes with its own magnetic field structure. The particles are deflected only in θ. The acceptance in ϕ is limited by the coils.

The magnet (see Figure 2.5) is made of six groups of 80 superconducting coils each, with a corrent of 10 kA capable of producing a 2 Tesla magnetic field.

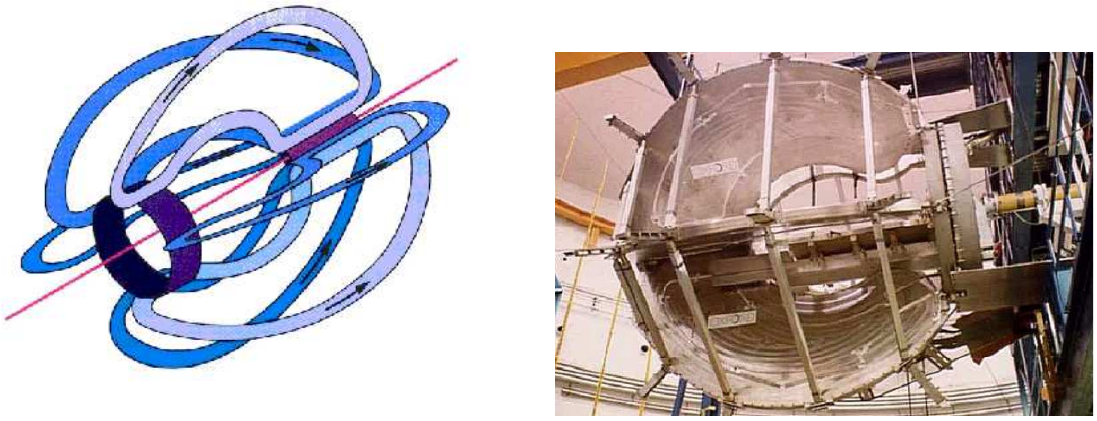

Figure 2.5: The torus magne

The coils technology is based on **C**able **I**n **C**ircuit **C**onductor, or CICC. Inside the coil the cable is made by 30% of liquid helium, which main advantages are the stability against temperature variations and the relatevily small helium reservoir (compared to systems that refrigerates by thermal immersion). The cryogenic system circulates with a 2.8 athmosphere pressure, with a refrigerating power of 200 Watts.

The metal infrastructure has to support the weight of the coils (around 6 tons) and the force between two neighbor coils (attractive or repulsive) which can reach dozen of tons per meter.

2.4 Drift Chambers

To calculate the momentum from (2.1) the curvature ρ must be measured. In CLAS there are three regions of Drift Chambers for this measurement.

The first region, shown in Figure 2.6, is located inside the torus coils. Its radius is about 0.5 meters. The second region is between the coils (inside the magnetic field), and the third region external to them.

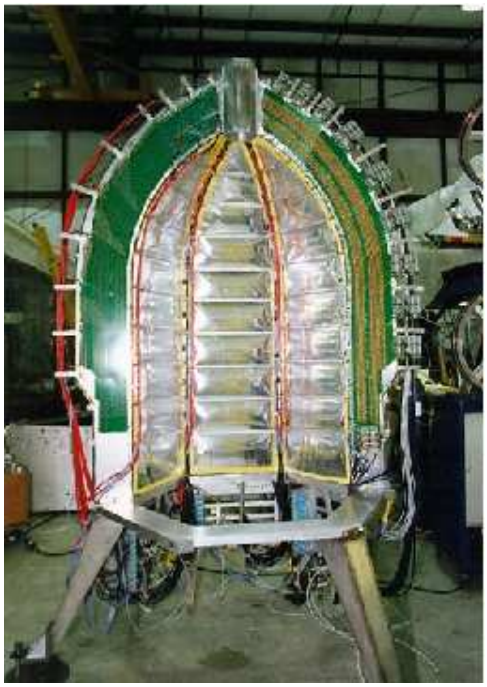

Figure 2.6: The torus magne

Each region is organized in two superlayers. The first superlayer (axial) has the wires along the magnetic field lines and the other one (stereo) at an angle of 6^0 with them. The angle is chosen to optimize the ϕ measurement. The superlayers in region 1 are divided in 4 layers each, the superlayers in region 2 and 3 are divided in 6 layers each.

Each layer consist in sense wires, each surrounded by six field wires to form an hexagonal cell as in Figure 2.7, where the field inside one cell (in region three) [13] is

also shown. A layer of guard wires surrounding each superlayer, tuned to simulated an infinite grid of cell like the one inside the layers, insures that the electric field is homogeneous.

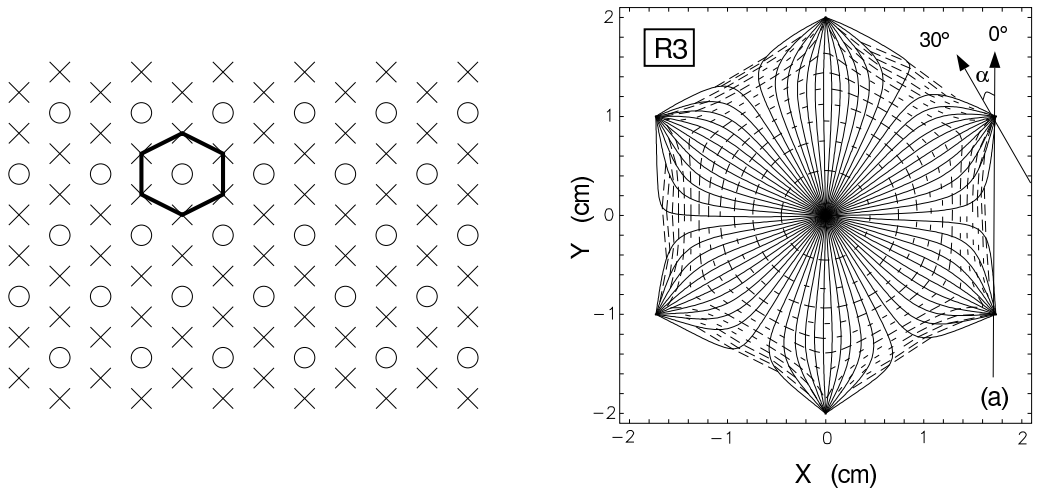

Figure 2.7: The "honeycomb" pattern of the drift chamber layers. Left: the sense wire ∘ surrounded by the field wires ×. Right: the field configuration inside one cel of region three (solid lines). The dashed lines are isochrones, or track positions with same drift time.

The sense wires are made of tungsten, 20 μm in diameter, and are plated with gold. The field wires are made of aluminum, 140 μm in diameter, to minimize multiple scattering. The gas used inside the chambers is a $90\% - 10\%$ mixture of argon and CO_2. The argon is chosen for its drift velocity (at least 4 cm/μsec), while the carbon dioxide defend the system against ionization avalanches up to several hundreds volts.

The track reconstruction is made in two stages. In the first step, called Hit Based Tracking, the hits within a superlayer are recognized as belonging to a track segment (see Figure 2.8). Different track segments from different supelayers are then linked to form a track. The linking is made by a comparison with a lookup table resulted from simulations.

In the second step, called Time Based Tracking, the drift time measured in each cell is converted into distance from the center, therefore the position around the sense wire is calculated. The trajectory is fitted to these positions as in Figure 2.8

[22] and this fit gives the momentum of the track. Figure 2.9 shows an example of track reconstruction.

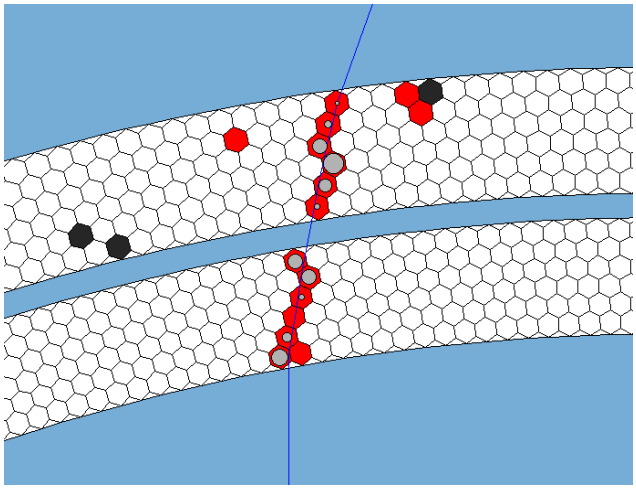

Figure 2.8: The torus magne

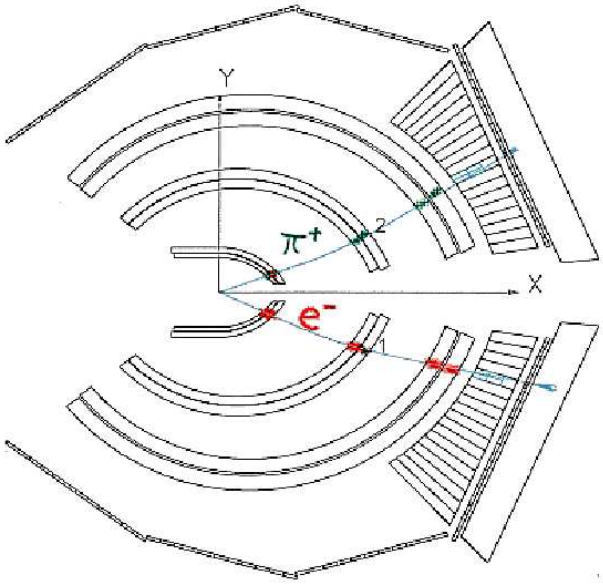

Figure 2.9: The torus magne

2.5 The Čerenkov detector

When the negative pions are not relativistic it is possible to distinguish between electrons and pions by measuring the time of flight, but for larger momenta the Čerenkov is necessary to do the separation. This separation is needed at a trigger level.

In CLAS there is a Čerenkov (CC) detector for each sector [1]. Each one, illustrated in Figure 2.10, cover the polar angle up to 45^0 and consists of 36 optical modules. The optic of each module was design to focus the Čerenkov light into a Winston collector cone leading into a PMT as shown in Figure 2.11. The 36 PMTs are located in the shadow of the torus coils, so that the acceptance is not affected by them. The gas chosen for the system was the perfluorobutane C_4F_{10}, which has a

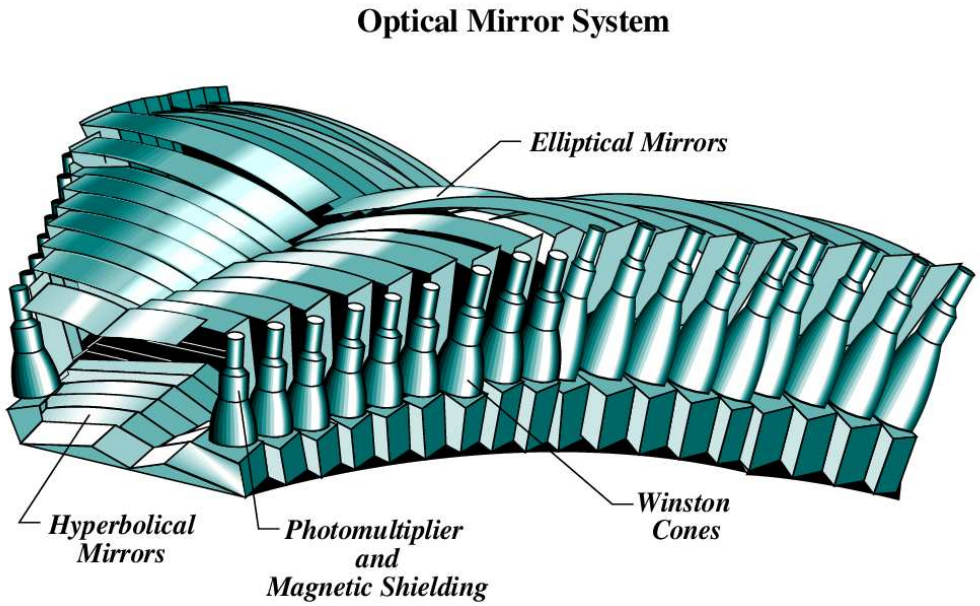

Figure 2.10: The torus magnet

refraction index of 1.00153. With the C_4F_{10}, electrons release Čerenkov light when their momentum is larger than 9 MeV (i.e. always in CLAS) while the threshold for pions is $\sim$ 2.5 GeV.

Figure 2.12 shows the single photoelectron peak position for one of the PMTs.

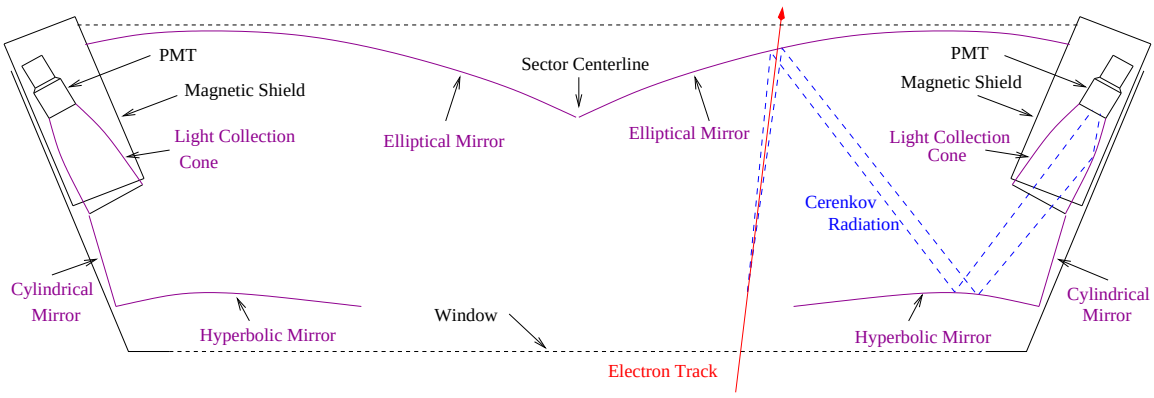

Figure 2.11: The torus magnasdasssssssssssssssssssssssssssssssssssssssssssssssssssssssssssssssssssssssssssssssssse

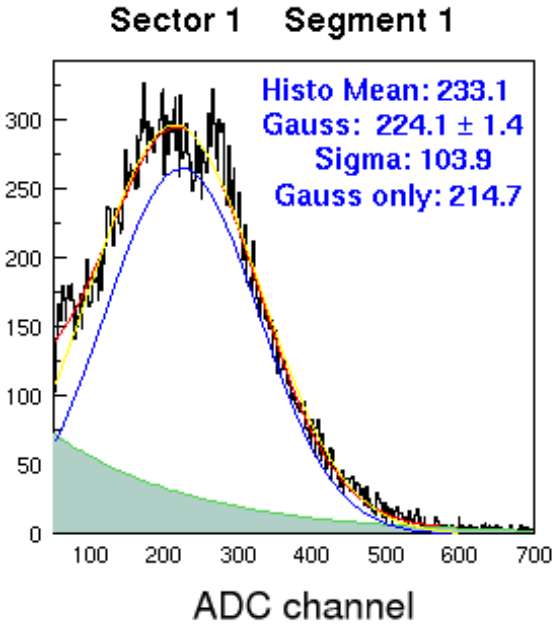

Figure 2.12: The torus magne

2.6 The Time of Flight system

The time of flight (TOF) information is used for the identification of the charged particles, as described in Section 3.5. The average time resolution of the TOF is $\sigma \sim 160$ psec [30], and it allows the separation of pions and kaons up to momenta of ~ 2 GeV (see Figure 3.6).

The TOF structure for each sector is illustrated in Figure 2.13. It consists four panels of scintillators bars (for a total of 57 scintillators in each sectors) varying in length from 32 to 450 cm. The PMTs, light collectors, voltage dividers and cables are placed in the torus coils shadow, so that the acceptance is not affected by them. The active region covers the polar angle from 8^0 to 142^0, for a total area of 206 m^2.

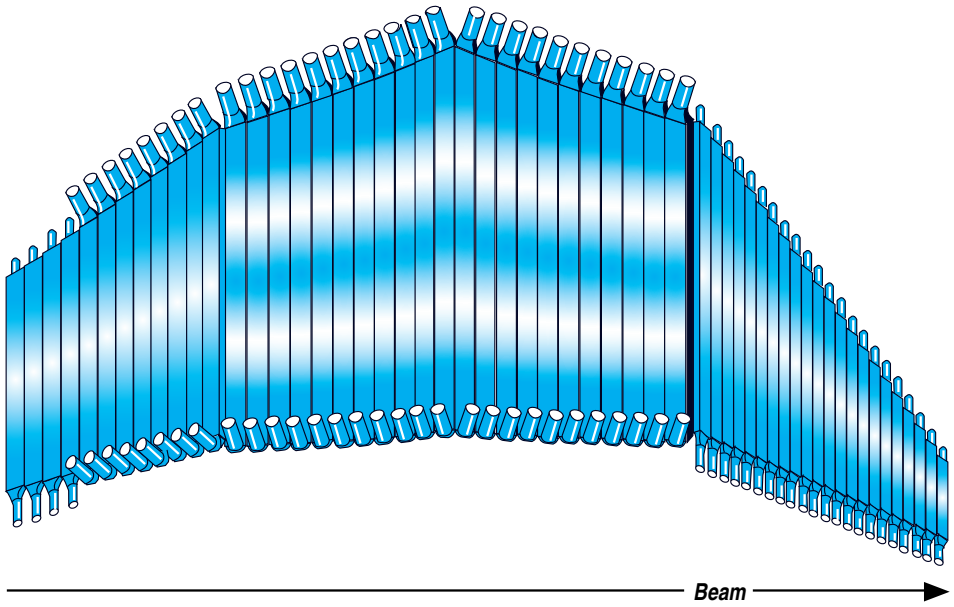

Figure 2.13: The torus magne

The light is collected by the guide illustrated in Figure 2.14. The readout electronics is crucial for the time resolution. The TDC chosen to perform the time

to digital conversion was the Lecroy 1872A Mod 100. The Lecroy was set to a 50 psec/count, which allows a range up to 200 nsec.

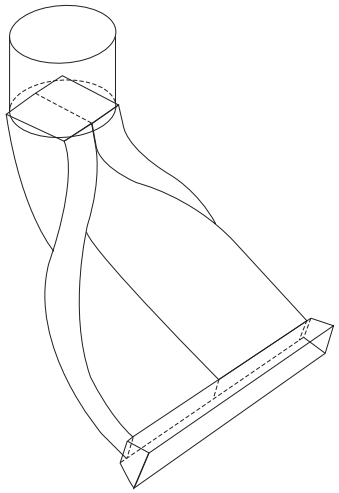

Figure 2.14: The torus magne

In Figure 2.15 the schematics for a single scintillator bar is shown.

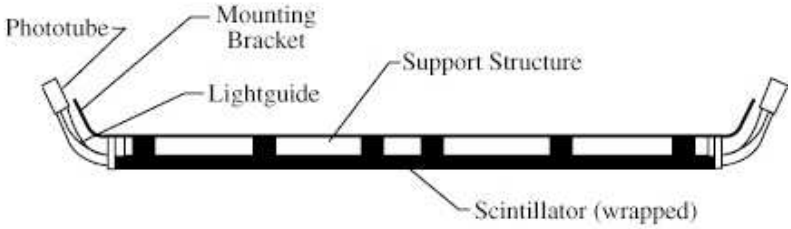

Figure 2.15: The torus magne

2.7 The forward calorimeter

The forward electromagnetic calorimeter (EC) [3] covers in each sector the polar angle from 8^0 to 45^0. It is composed by 39 layers of scintillator bars alternated with lead sheets. The bars are rotated by 120^0 in each successive layer (see Figure 2.16). There is a total of 40 cm of scintillator and 8 cm of lead for each module, so that the energy shower of an electron deposited in the scintillator amount to $\sim 1/3$ of the total energy. The total thickness is 16 radiation lengths.

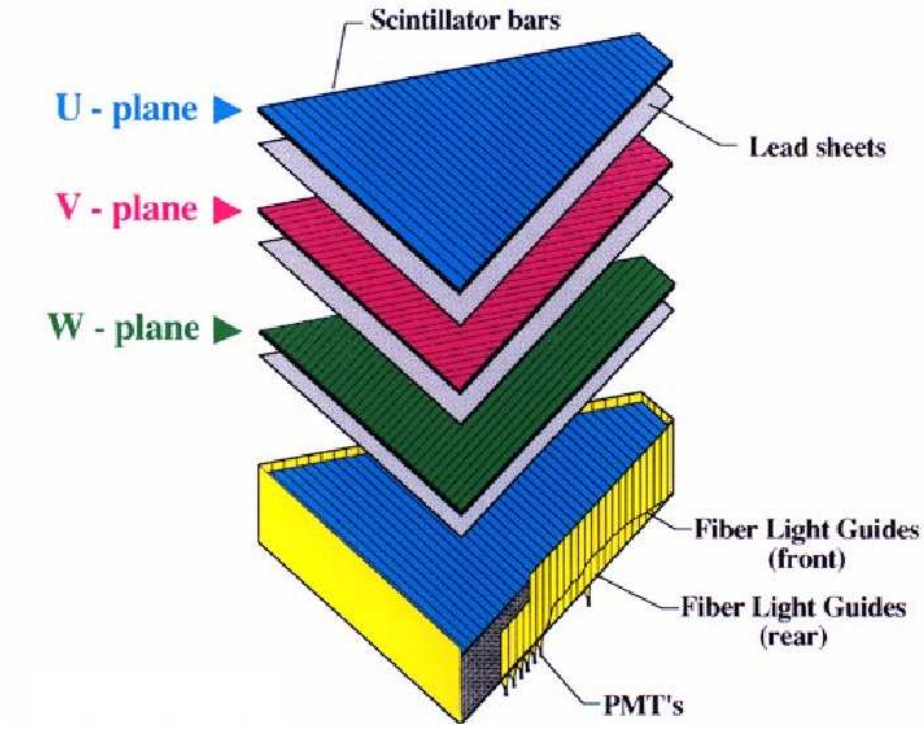

Figure 2.16: The torus magne

The bars make three groups (of 13 layers each) of bars with the same direction. Each group is divided in INNER and OUTER parts, whose scintillator signals are summed together and collected with light guides in two PMTs as described in Figure 2.17.

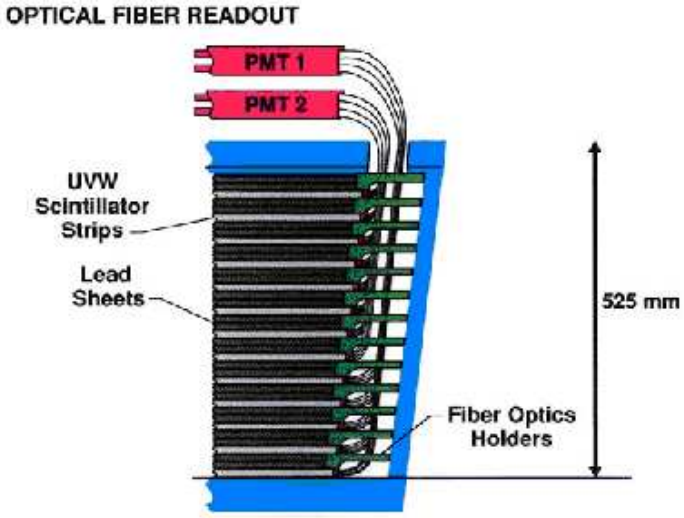

Figure 2.17: The torus magne

The EC is used for the following tasks:

- Detection and triggering of electrons. The analog sum from one sector is used (usually in coincidence with the Čerenkov) as trigger for CLAS.
- Separation of electrons and pions above momenta of ~ 2.5 GeV. See Figure 3.2 for an example of such separation.
- Detection of photons with energy above 200 MeV. This allows DVCS measurement, and π^0 and η detection via their 2γ decay.
- Neutron detection. The timing information of the EC allows $\gamma - N$ separation with an efficiency $> 50\%$.

Figure 2.18 show a GEANT simulation of the EC response to a 2.4 GeV electron [3]. Figure 2.19 shows a real event in the EC.

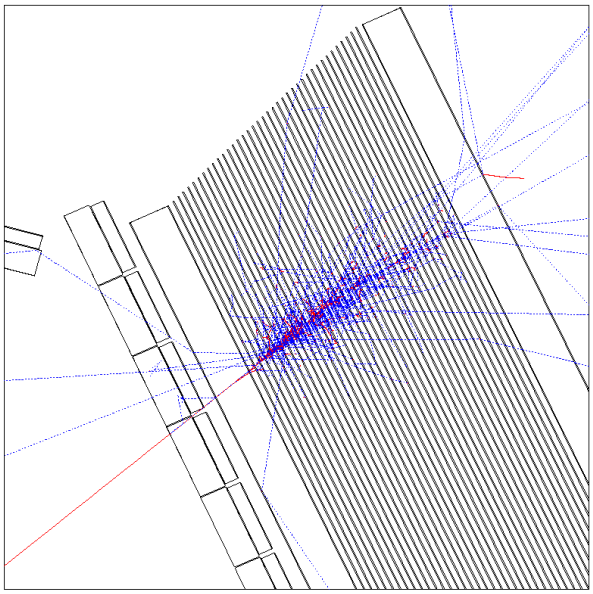

Figure 2.18: The torus magne

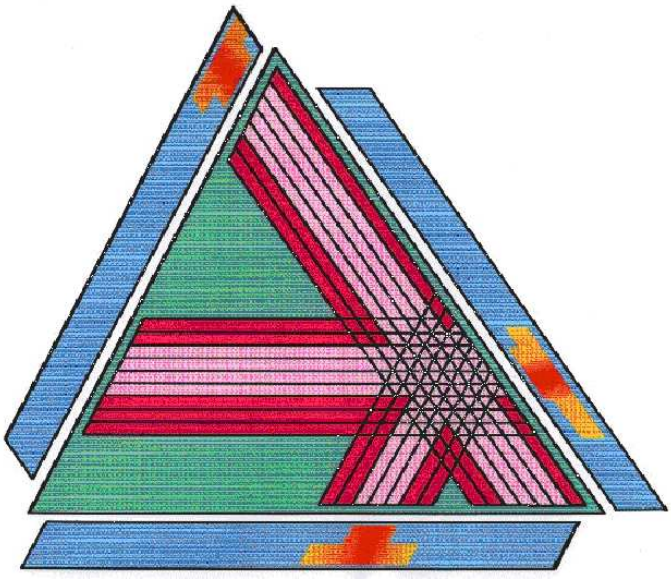

Figure 2.19: The torus magne

CHAPTER 3
Data processing

3.1 Data format

3.1.1 Bos Banks

3.1.2 Reconstruction Code

3.1.3 SEB and PID

3.1.4 Binary DST

3.2 Calibrations

3.2.1 RF correction

3.3 Cooking

3.4 Electron identification

Only 1/3 of the triggers during the initial data processing have reconstructed negative tracks, and out of these only 1/3 are identified as containing an electron. In this identification, there is still a pion contamination problem mainly due to Čerenkov inefficiencies. The *candidate electron* of this analysis is:

- Any reconstructed PART bank electron[1].
- Any reconstructed EVNT bank electron.
- Any negative unknown PART bank particle if there is no PART bank electron.
- Any negative unknown EVNT bank particle if there is no EVNT bank electron.

There are 6 ID cuts defining a *good electron* starting from a *candidate electron* based on its momentum p, its signal in the Čerenkov *nphe*, its signals in the forward calorimeter (total energy EC_{tot}, inner energy EC_{in}, outer energy EC_{out}) and its position on the EC (x, y):

- Čerenkov cut
- minimum p cut
- EC_{tot}/p versus p cut
- EC_{out}/p vs EC_{in}/p cut
- EC_{in} / EC_{tot} cut
- x_{EC} vs y_{EC} cut

3.4.1 Čerenkov signal cut

A threshold for the signal in the Čerenkov detector is necessary to eliminate electronic noise and the fact that pions produce Čerenkov light when their momentum is above 2.4 GeV.

[1]See section 3.1.3 for the meaning of PART and EVNT bank

The signal is turned in *number of photoelectrons* (nphe) and then multiplied by 10 by the reconstruction code. Fig.3.1 shows the cut used:

$$\text{nphe} > 2.5$$

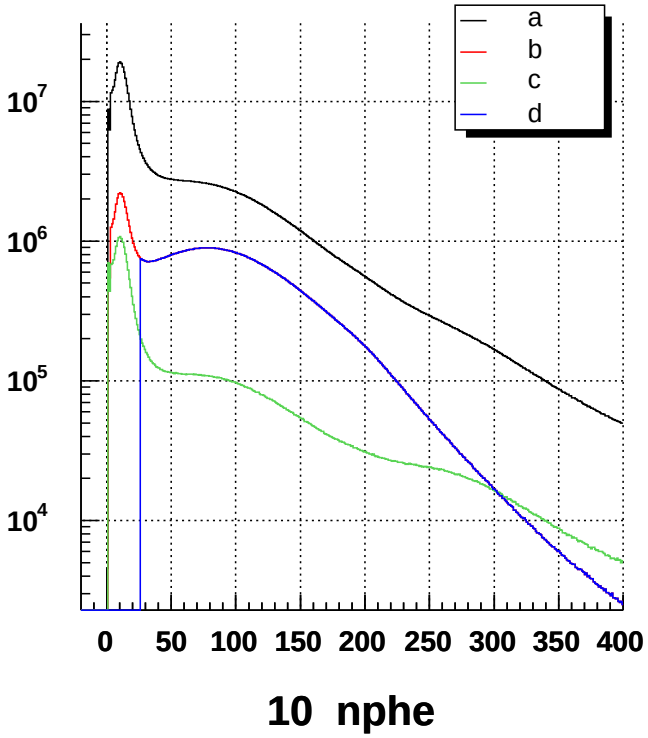

Figure 3.1: The CC signal threshold cut: 10 nphe.
(a) all electrons. (b) electrons with all other ID cuts (aside from Čerenkov cut) applied. One can see that the signal at 100 ($\sim$ 10 nphe) is enhanced. (c) electrons with all other ID anti cuts (aside from Čerenkov cut) applied. This events corresponds to the pions and the noise. (d) electrons with all ID cuts applied.

3.4.2 Total energy in the calorimeter

In the momentum range detected at CLAS, when going through the forward calorimeter charged pions are minimum ionizing particles, while electrons shower with a total energy deposition E_{tot} proportional to their momentum P. Hence E_{tot}/P

should be constant. In reality this ratio shows a slight momentum dependance as it is illustrated in Figure 3.2 where the E_{tot}/P distribution is plotted versus P. This distribution was sliced along P and each slice is fitted with a gaussian distribution, giving the mean and sigma as a function of p:

$$\bar{p} = \bar{p}(p)$$
$$\sigma = \sigma(p)$$

A second order polynomial is fitted to those distributions and events are accepted if they occur within 3 σ around $\bar{p}$, i.e. if

$$\bar{p} - 3\sigma \leq E_{tot}/P \leq \bar{p} + 3\sigma$$

The cut is shown in Figure 3.2 as dotted red lines. See Appendix A.1.2 for the numerical values of the parameters.

3.4.3 Minimum p cut

A study [12] of the inclusive cross section at various beam energies in CLAS results in a low momentum cut p_{min} depending on the calorimeter low total threshold (in millivolt) of the trigger discriminator:

$$p_{min}\ (\text{MeV}) = 214 + 2.47 \times EC_{threshold}(\text{mV})$$

Such a threshold was 172 mV for e1-6 therefore the minimum momentum cut is fixed at:

$$p_{min} = 0.64\ \text{GeV}$$

The cut is shown in Figure 3.2 as a vertical line.

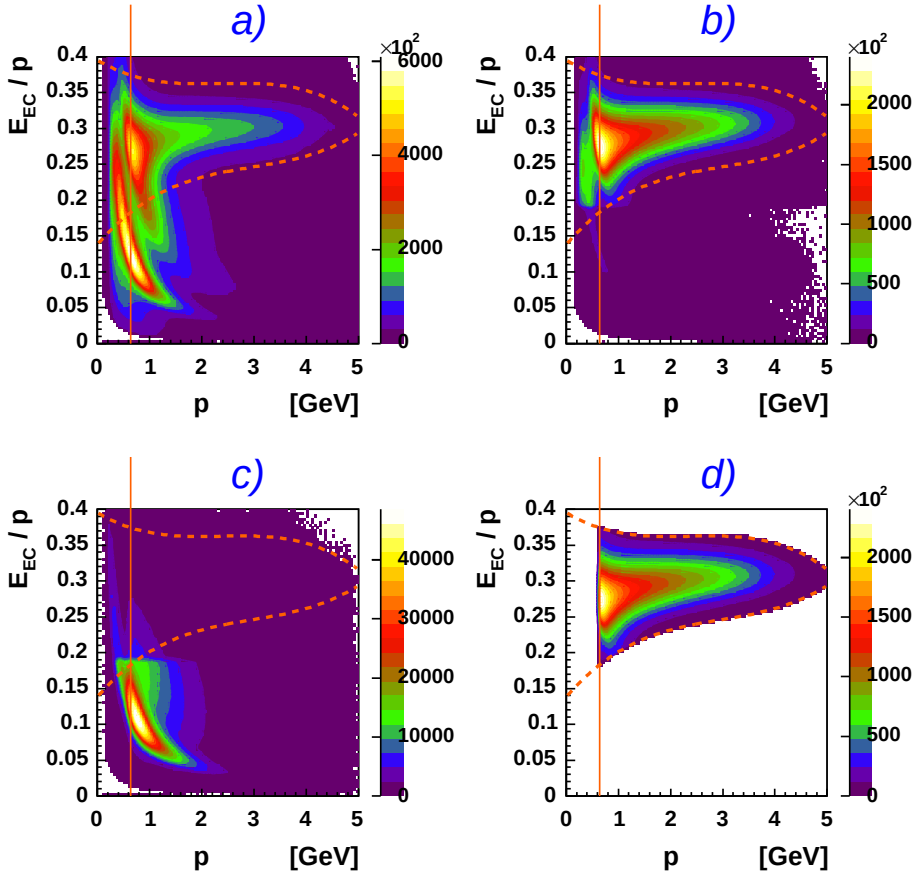

Figure 3.2: E_{tot} and p_{min} cut. For minimum ionizing particles E_{tot} is constant so they show as an hyperbole. The vertical line represents the p_{min} cut. The remaining two dashed lines are the $\bar{p} \pm 3\sigma$ cuts. (a) all electrons. (b) electrons with all other ID cuts (aside from E_{tot} and p_{min} cuts) applied. The band corresponding to minimum ionizing particles disappear almost completely. (c) electrons with all other ID anti cuts (aside from E_{tot} and p_{min} cuts) applied. This events corresponds to minimum ionizing particles and background. (d) electrons with all ID cuts applied.

3.4.4 EC_{out}/p vs EC_{in}/p cut

The outer EC is 5/3 times bigger than the inner EC therefore pions, which do not shower and are minimum ionizing, release a small quantity of energy in the outer and inner part in the ratio 5 : 3. On the other hand electrons release a lot more more energy because they shower. Moreover, due to showering, electrons release more energy in the inner part than in the outer part.

The quantity E_{in}/p is plotted versus E_{out}/p in Figure 3.3. One can see the pions along the cyan line $y = \frac{5}{3}\,x$ and the electrons on the right part of the red line, which represents the cut and assumes the form

$$y = 0.19 - x$$

A bug in the reconstruction code sometimes gives a wrong (zero) values for E_{in}, E_{out}. For those events, this cut was not applied.

3.4.5 E_{in}/E_{out} cut

Electrons release more energy in the inner part of the calorimeter than in the outer part because of the shower conformation. This can be seen in Figure 3.4 where E_{in}/E_{out} is plotted against p.

By looking at the plot, a low threshold cut on E_{in}/E_{out} is introduced at 40%:

$$E_{in}/E_{out} \geq 0.4$$

The cut is shown in the figure as an horizontal red line.

3.4.6 Track position cut

Electrons that shower near the edges of the calorimeter will not loose all their energy in the detector because the shower is truncated. Hence their energy cannot be properly reconstructed.

For this reason a fiducial cut is introduced on the track coordinates x, y of the electrons at the EC plane. The cut is illustrated in Figure 3.5.

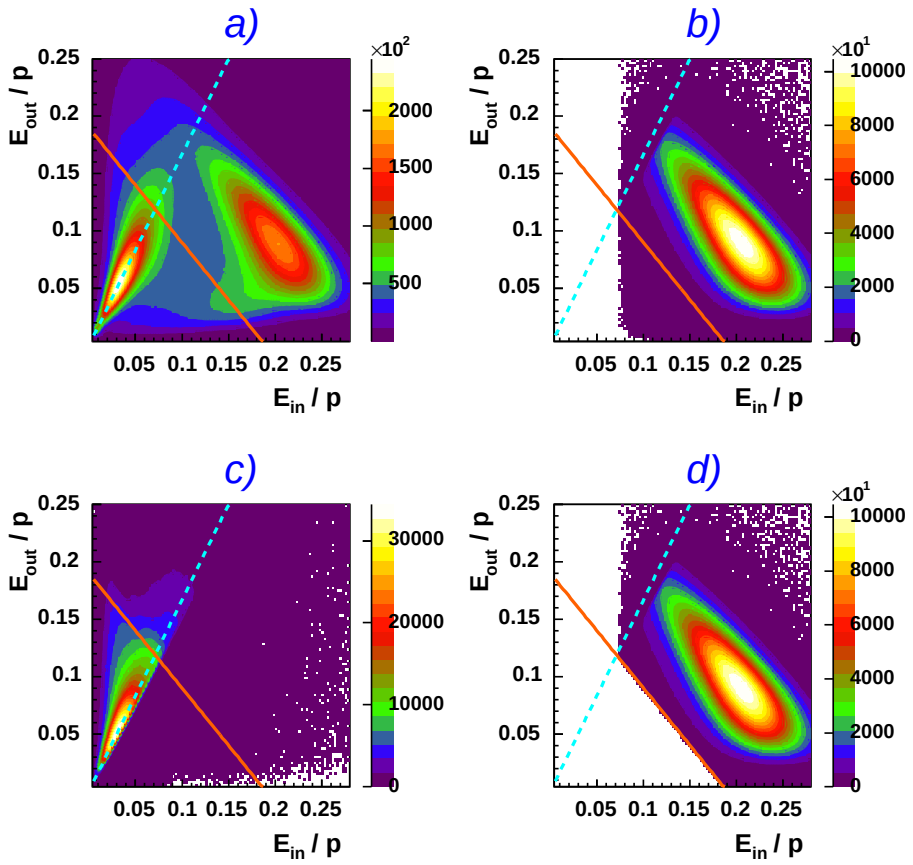

Figure 3.3: EC_{out}/p vs EC_{in}/p cut. (a) all electrons. (b) electrons with all other ID cuts (aside from EC_{out}/p vs EC_{in}/p cut) applied. The band corresponding to minimum ionizing particles disappear almost completely. (c) electrons with all other ID anti cuts (aside from EC_{out}/p vs EC_{in}/p cut) applied. This events corresponds to minimum ionizing particles and background. (d) electrons with all ID cuts applied.

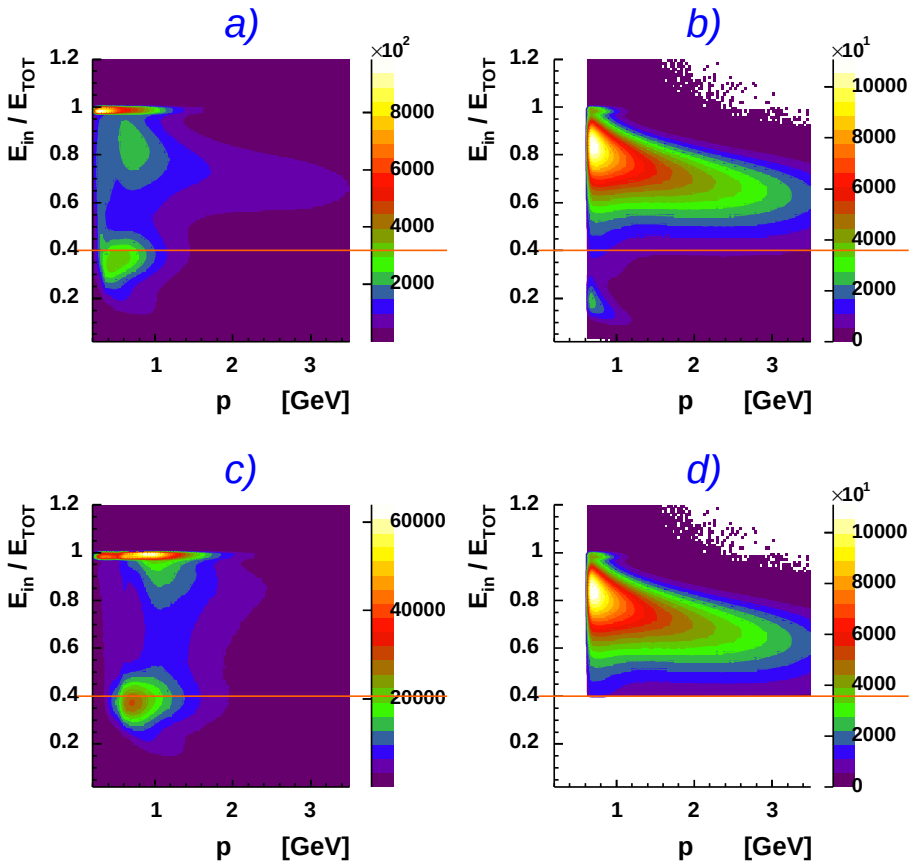

Figure 3.4: The E_{in}/E_{tot} cut. Particles that are stopped in the inner part (hence have small energy) have $E_{in} = E_{tot}$ so they show up at $E_{in}/E_{tot} = 1$. Most of these are cut out with the ID cuts. (a) all electrons. (b) electrons with all other ID cuts (aside from E_{in}/E_{tot} cut) applied. (c) electrons with all other ID anti cuts (aside from E_{in}/E_{tot} cut) applied. Minimum ionizing particles are enhanced here. They release comparable energy in the inner and outer part. Since the inner part is 3/8 of the total calorimeter, they peaks in this plot at $3/8 = 0.375\%$. (d) electrons with all ID cuts applied.

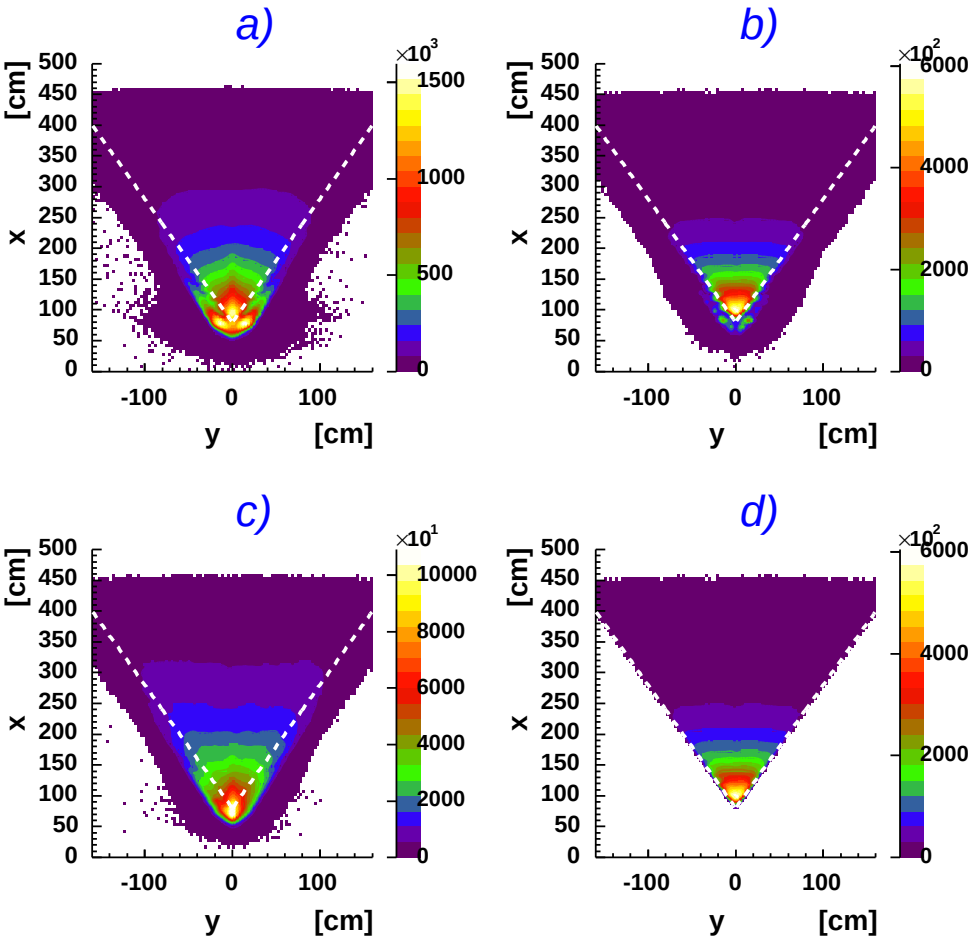

Figure 3.5: x, y cut. (a) all electrons. (b) electrons with all other ID cuts (aside from E_{in}/E_{tot} cut) applied. The x, y cut is chosen so that it encompass the electrons in this plot. (c) electrons with all other ID anti cuts (aside from E_{in}/E_{tot} cut) applied. (d) electrons with all ID cuts applied.

3.5 Proton Identification

During the event reconstruction tracks are labelled by particle type depending on their **speed**, their **momentum** and how they bend in the magnetic field.

The momentum of the track is calculated during the event reconstruction with a tracking procedure [22]. To determine the speed of the track, a start time T_0 is calculated as follows:

$$T_0 = T_{el} - \frac{\ell}{c} - \frac{z - z_0}{c}$$

where T_{el} is the RF corrected (see section 3.2.1) electron time from TOF measurement, z is the vertex position of the electron track, ℓ is the pathlength of the electron track from its vertex to its TOF hit, z_0 is the z position of the center of the target[2] and c is the speed of light. The startime is used as the reference for all the remaining tracks in the event.

The speed β for each track with pathlength ℓ and TOF time T is therefore calculated as

$$\beta = \frac{v}{c} = \frac{\ell}{T - T_0}$$

In Figure 3.6 is plotted beta versus momentum for all particles after the electron particle ID. One can clearly see bands corresponding to pions, kaons, protons, even deuterons.

The calculation of the mass of the track M (referred as TOF Mass) is straightforward from β and p:

$$M^2 = \frac{p^2(1 - \beta^2)}{\beta^2}$$

M is quantity upon which the software reconstruction is based to determine the particle ID.

In the main torus configuration of e1-6 running period negative particles bend toward the beam line and positive particles bend away from it. Every outbending EVNT or PART track in each event is considered a *proton candidate*.

M is plotted for the candidates in Figure 3.7 where the y-axis is logarithmic. One can see a well defined proton peak.

[2]For this experiment $z_0 = -4$ cm.

For the proton, the default cut is $0.8 \leq M \leq 1.2$.

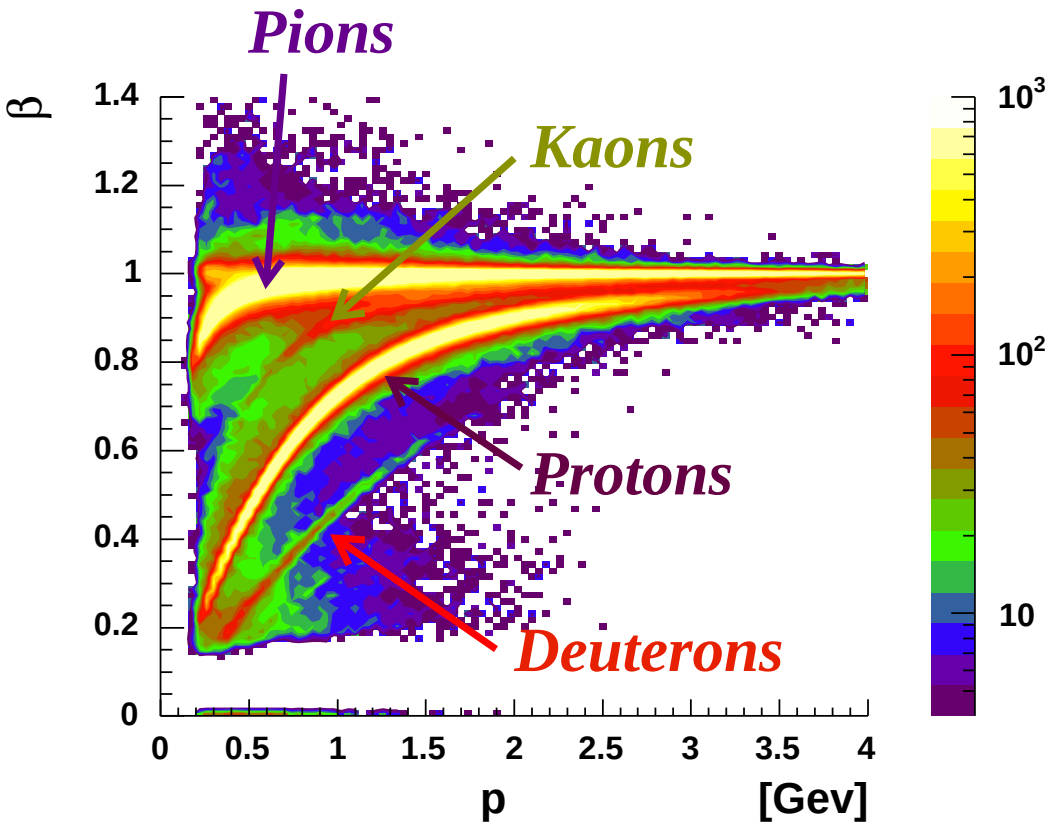

Figure 3.6: β versus momentum for all particles in e1-6 running period. Bands corresponding to pions, kaons, protons and deuterons are visible. Electrons have $\beta = 1$ by definition.

The proton ID has been redone relaxing the default cut. Kinematic constrains will get rid of possible ambiguities between protons and other particles and background.

The cut used in this analysis, illustrated in Figure 3.7, is simply:

$$0.6 \leq M \leq 1.6$$

and it is illustrated in Figure 3.7.

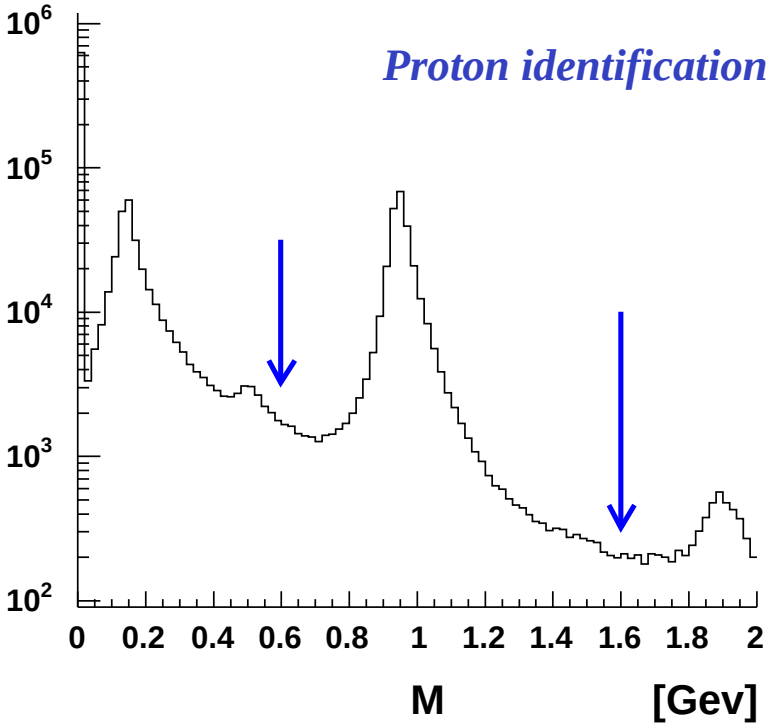

Figure 3.7: TOF mass spectra for CLAS. Starting from massless particles are visible: electrons (zero mass), pions, kaons, protons and finally deuterons.

3.6 Vertex correction and cut

For each track found with the reconstruction code, a vertex (x, y, z) is calculated from the intersection of that track with the midplane[3] of the corresponding sector. If during the experiment the beam was note centered at $(0, 0)$ an offset is introduced in the vertex calculation.

This happened [19] during the e1-6 running period as one can see in Figure 3.8, where the events on the window[4] downstream of the target were selected to fix the z position as reference.

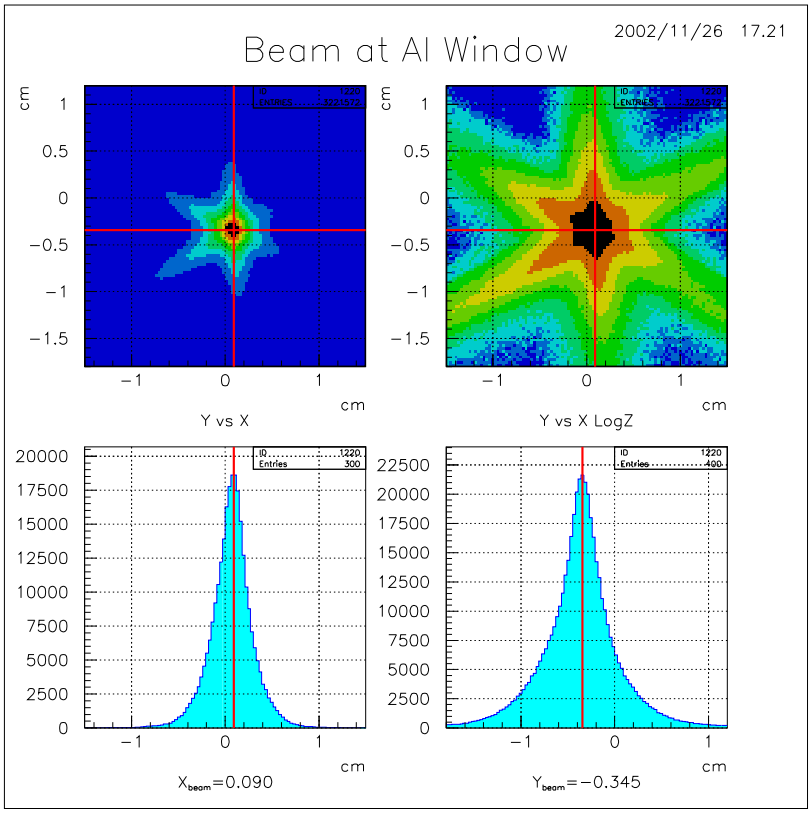

Figure 3.8: Top: y versus x position of the vertex at the window. Upper right: same as upper left, except plotted logarithmically. One can see that the beam spot was slightly shifted from $(0, 0)$. Bottom: the x (left) and y (right) distributions which leaded to the x_0 and y_0 calculation.

[3]The midplane of a sector is defined by the plane that divide that sector in half and contains the beamline $(0, 0, z)$.

[4]A window was placed at $z = 0$ to help these kind of studies and to be a z-position reference.

The obtained values for the beam position are:

$$\begin{aligned} x_0 = &\quad 0.090 \quad cm \\ y_0 = &\quad -0.345 \quad cm \end{aligned}$$

To correct the vertex position it is sufficient to shift the midplanes so that they contain the correct beamline $(0.09, -0.345, z)$ and recalculate the intersection of the tracks with the new planes. This is illustrated in Figure 3.9.

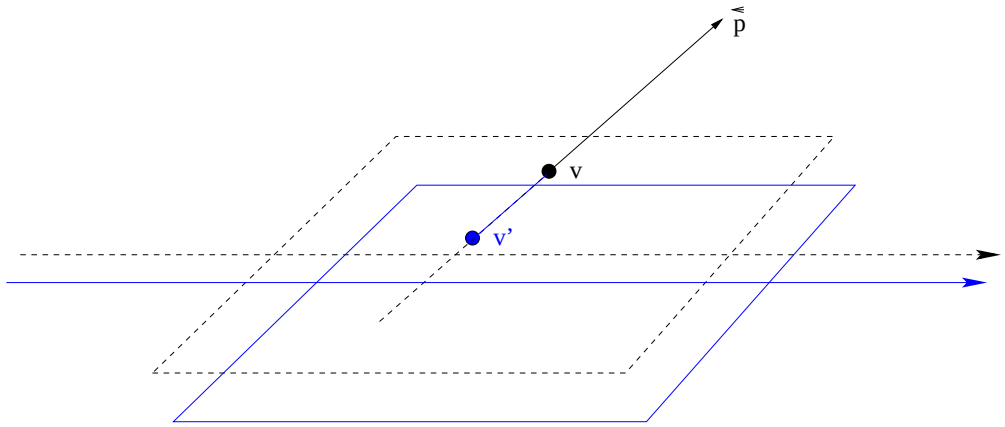

Figure 3.9: The vertex correction. The dashed plane is the original midplane containing the wrong beamline $(0, 0, 0)$. The point v is the intersection of the track (straight line along momentum $\vec{p}$) with this plane. The solid blue plane represents the corrected midplane containing $(0.09, -0.345, z)$. The correction algorithm simply intersect the same track with the corrected midplane.

The effect of the correction on the electron z position sector by sector is shown in Figure 3.10.

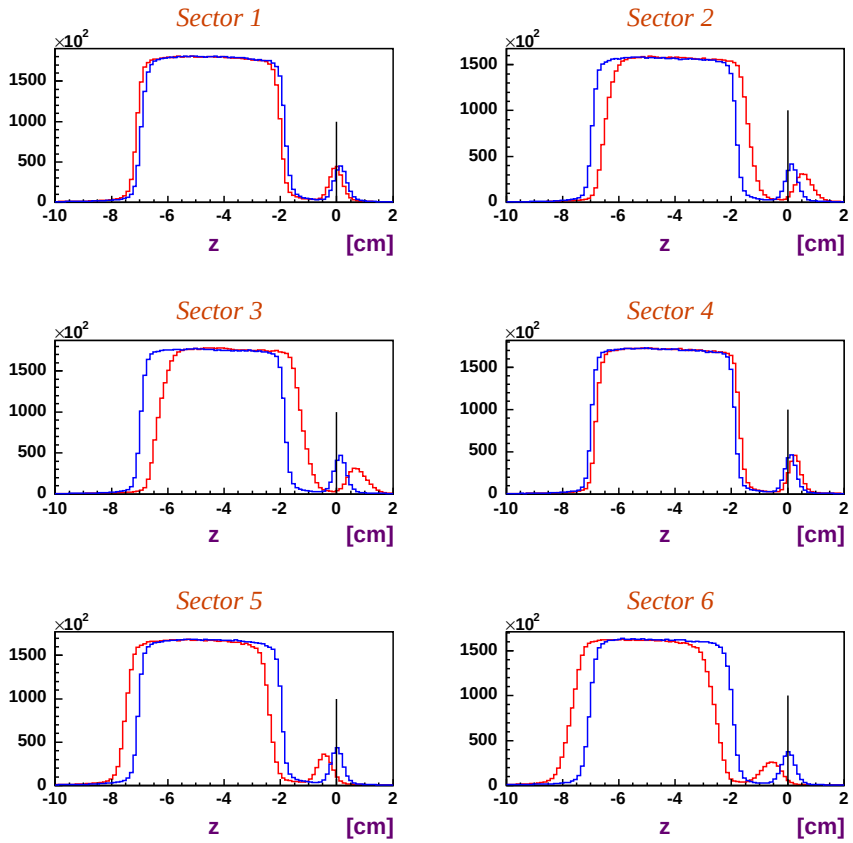

Figure 3.10: The vertex correction effect on electron z distributions for each sector. Black: before correction. Blue: after correction. Similar effects on the other particles are observed.

The vertex resolution at this point is good enough to introduce a cut on the z vertex of electron and protons in order to select events inside the target cell as follows:

$$-8\,cm \leq z \leq -0.8\,cm \tag{3.1}$$

Furthermore the electron and proton vertices are required to be coincident along the z axis within the reconstruction resolution, so an additional cut on $\Delta z = z_{electron} - z_{proton}$ ensures that the electron and proton z vertex positions lie within

1.6 cms:

$$|\Delta z| < 1.6\,cm \tag{3.2}$$

Figure 3.11 illustrates the effect of the vertex correction on Δz integrated over all sectors and both the 3.1 and 3.2 cuts.

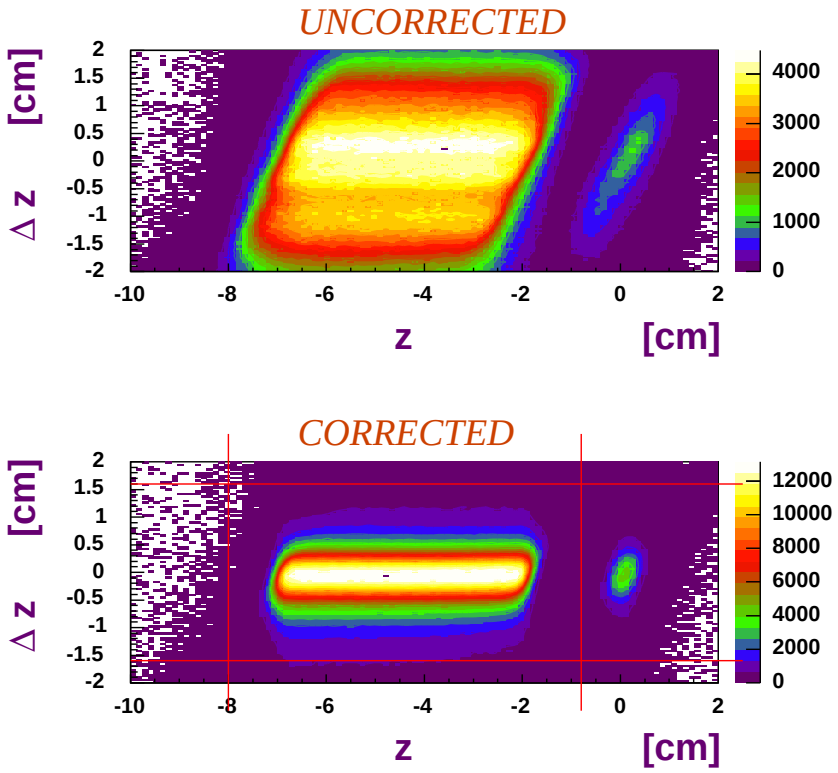

Figure 3.11: Δz versus $z_{electron}$ uncorrected (top) and corrected (bottom) for all sectors. The distortions disappear with the correction and the resolution improves.

3.7 Electron Fiducial cuts

A fiducial cut on electrons is introduced to constrain regions of phase space where CLAS response peaks at its maximum and remains rather smooth. The Čerenkov detector presents a drop in optical efficiency (see Figure 3.12) which is not simulated by the Montecarlo, therefore these regions have to be removed.

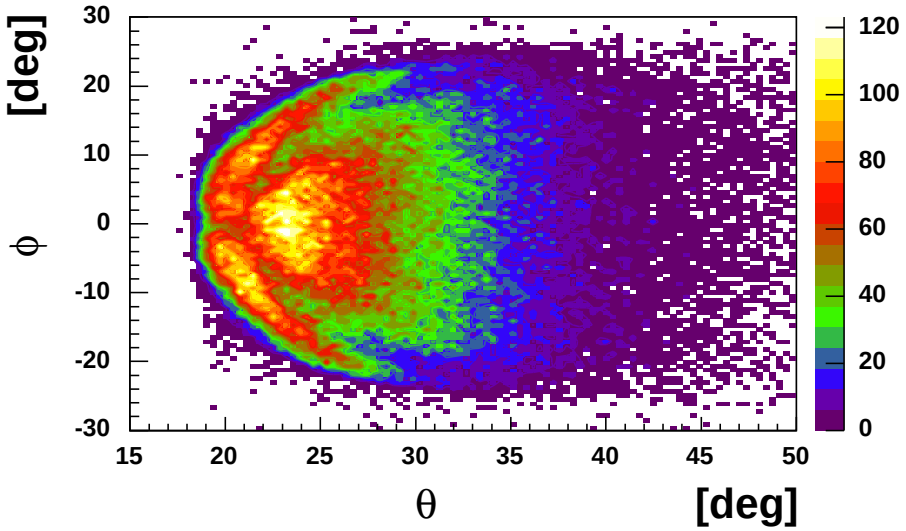

Figure 3.12: ϕ versus θ for sector 1 electrons before the electron particle ID. The Čerenkov optical inefficiencies (denoted by the arrows) are clearly visible.

Drift chamber and time of flight inefficiencies (dead or inefficient wires, dead phototubes) cause holes and depletions in the acceptance. While most of these symptoms appears in the GSIM simulation, some do not. Furthermore the boundaries of all these regions differ when comparing actual data and simulation.

3.7.1 ϕ boundaries

For each sector, an empirical cut on ϕ is introduced as a function of theta and momentum:

$$\phi \;\leq\; \Delta\phi\,(\theta, p)$$

which is aimed to define regions of phase space whose distributions are flat in ϕ. After careful study [24], the mathematical form of the cut depends on 6 parameters C_i and assumes the form:

$$\begin{aligned} \Delta\phi &= C_4\,(\sin(\theta - \theta_{cut}))^{\,E} \\ E &= C_3\,p^{\,C_5} \\ \theta_{cut} &= C_1 + \frac{C_2}{p + C_6} \end{aligned}$$

A ϕ vs θ distribution was plotted for 10 different momentum bins from 1.6 to 4.6 GeV. Figure 3.13 shows one example ($p = 2.2 - 2.5$ GeV) of such distributions.

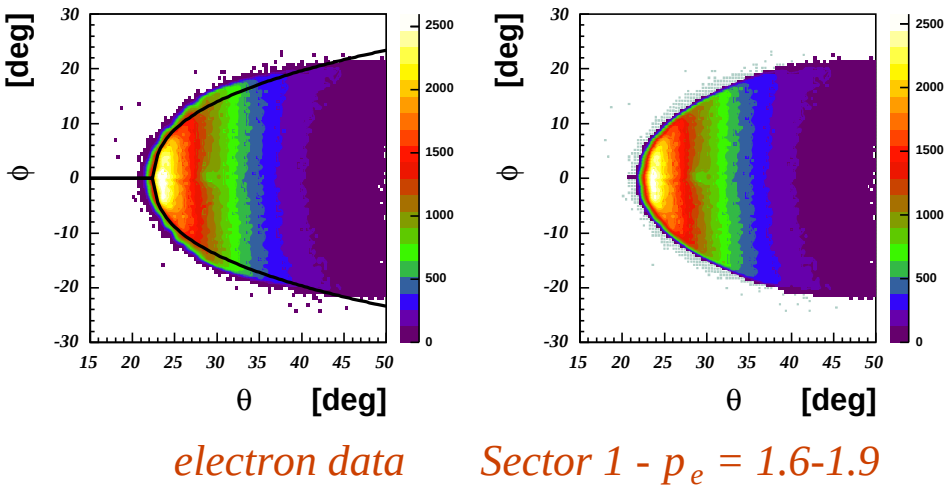

Figure 3.13: ϕ versus θ for sector 1 and $p = 2.2 - 2.5$ GeV. Left: before fiducial cut. Right: after fiducial cut (contour).

The ϕ distributions are also plotted for θ slices one degree wide as in Figure 3.14 and the C_i parameters are adjusted empirically.

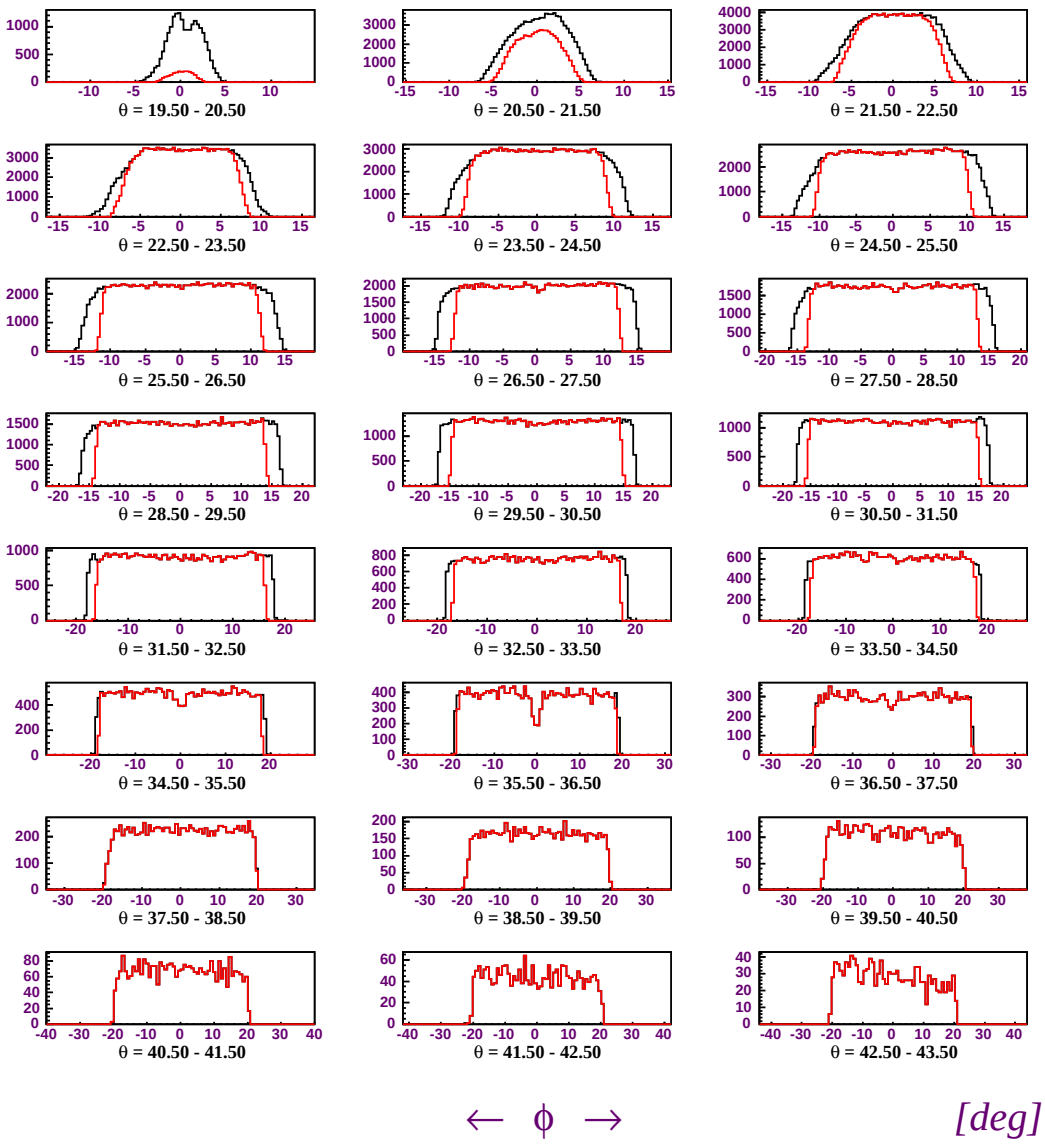

Figure 3.14: ϕ distributions (sector 3) for different θ and $p = 1.9 - 2.2$ GeV. Black: before fiducial cut. Red: after fiducial cut. Čerenkov inefficiency (section 3.11) is responsible for some irregularities at $\phi = 0$ (for example at $\theta = 35.5^0 - 36.5^0$) while drift chamber and time of flight inefficiency (section 4.2.3) causes ϕ asymmetry (for example at $\theta = 42.5^0 - 43.5^0$).

Table 3.1 shows the 6 parameters obtained. Figure 3.15 shows the fiducial cut as a function of p, θ and ϕ for sector 1.

Sector	C_1	C_2	C_3	C_4	C_5	C_6
1	12.0	20.0	0.32	32.0	0.416667	0.14
2	//	20.7	0.36	34.0	//	//
3	//	20.2	0.32	32.0	//	//
4	//	20.5	0.32	32.0	//	//
5	//	20.5	0.29	32.0	//	//
6	//	20.0	0.32	32.0	//	//

Table 3.1: The 6 parameters for electron fiducial cut for each of the 6 sectors. Only C_2, C_3, C_4 are sector dependent.

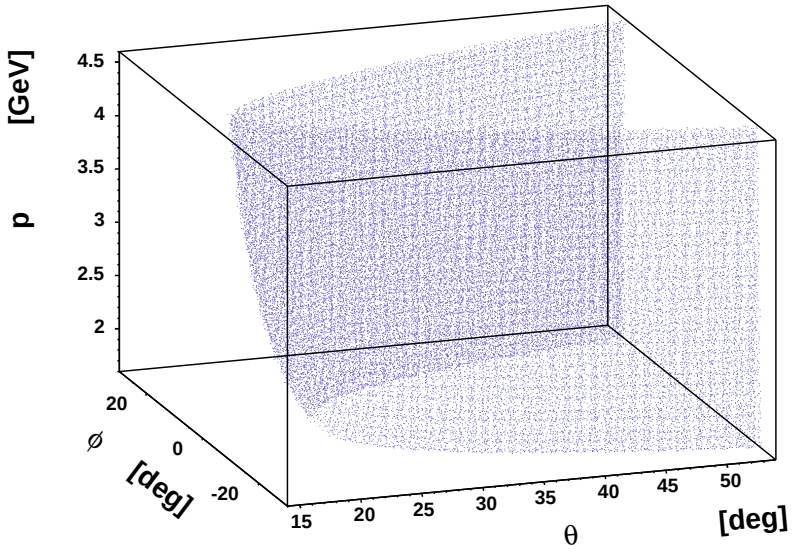

Figure 3.15: The electron fiducial cut for sector 1. The cut starting point moves back as the momentum increases (and θ decreases). This causes the cut to narrow up with momemtum because electrons are detected near the lower edges of the detectors.

3.7.2 θ versus momentum cuts

Sector 2, 5 and 6 present holes and depletions (mainly because of dead time of flight paddles) which are taken care of with the cuts shown in Figure 3.16 where θ is plotted versus p.

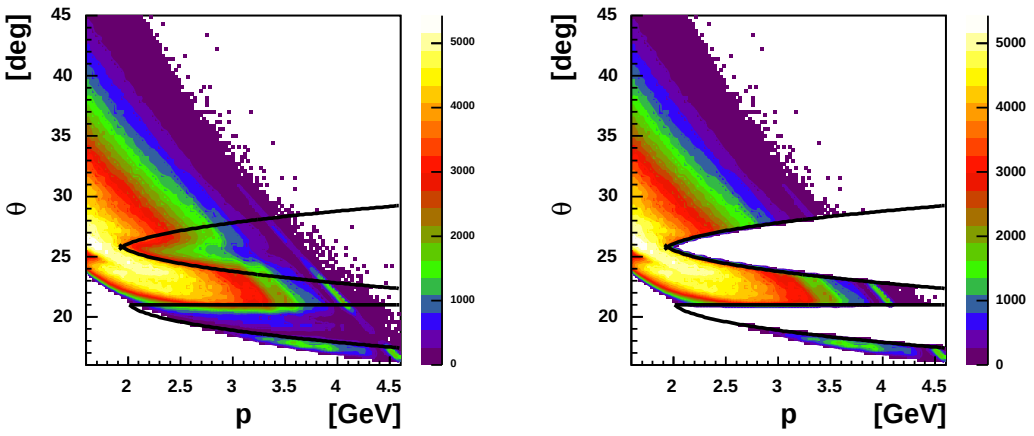

Figure 3.16: θ versus p for sector 5. Two depletions are clearly visible and cut out.

A summary of all the cuts used for the electron fiducial cut can be found in Appendix A.1.4. Figure 3.17 shows the effects of the fiducial cuts on sector 6 ϕ versus θ distribution.

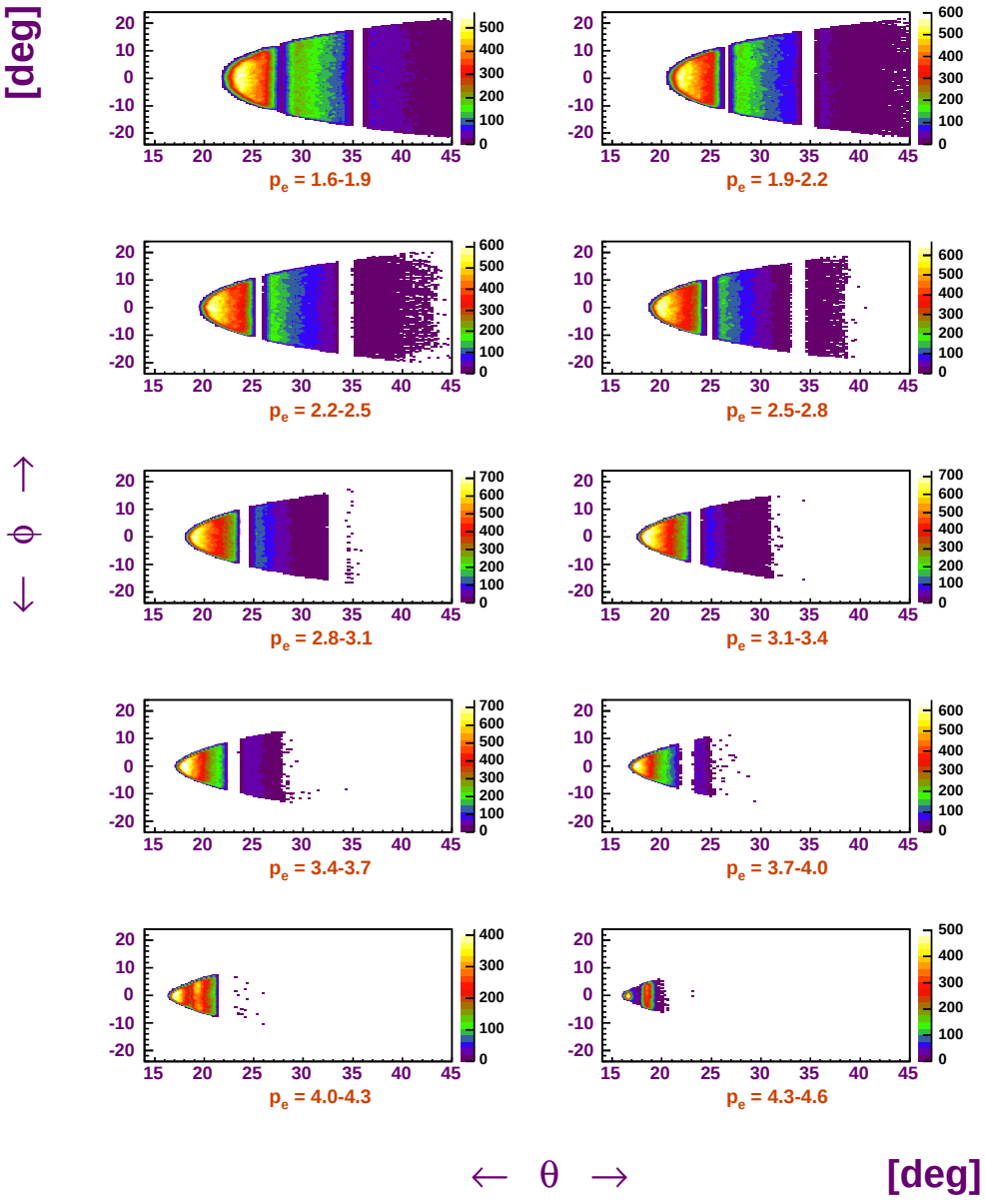

Figure 3.17: ϕ versus θ distribution for sector 6 after fiducial cuts. The θ versus p cuts are reflected on this plane as vertical bands.

3.8 Proton Fiducial cuts

Protons present low efficiency regions as well as electrons. Their detection and reconstruction close to boundaries or dead channels is not well understood.

The holes and depletions are treated with the same way as it was done for the electrons. The depletions present as curved bands in ϕ versus θ plots shown below (Figure 3.18 and Figure 3.21) because they are function of momentum and the binning chosen (which is correct for determine the ϕ boundaries) is not fine enough to exploit this dependance in the plots.

Unlike the electron case, the ϕ boundaries are asymmetric, as shown in Figure 3.18.

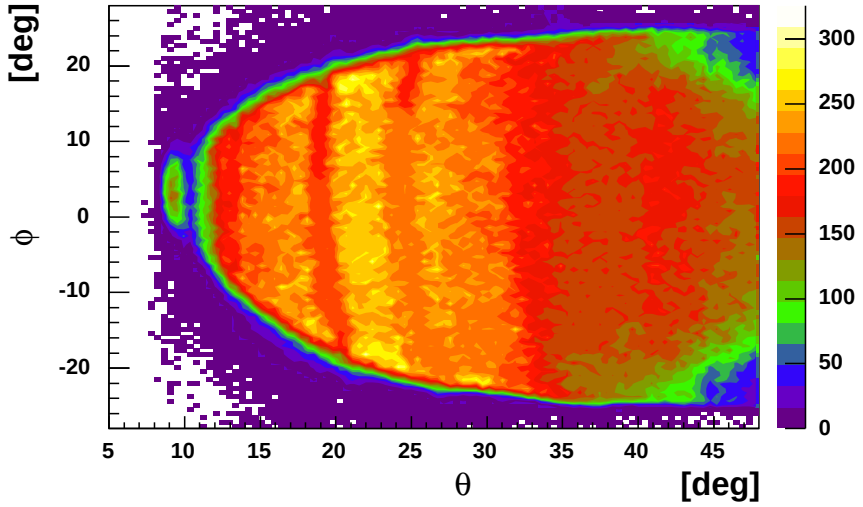

Figure 3.18: ϕ versus θ for sector 5. The momentum ranges from 0.9 to 1.6 GeV. The distribution is ϕ-asymmetric. Depletions along ϕ similar to the electron case are visible.

3.8.1 ϕ boundaries

In order to evaluate ϕ boundaries the momentum has been divided into five bins equally spaced from 0.9 to 4.4 GeV. The momentum dependance of the fiducial cut is not as strong as it was for the electrons, so a fewer number of bins are necessary.

For each momentum bin the ϕ distributions were divided in θ intervals of 1 degree and fitted with a trapezoid function [23]. The fit gives as output the ϕ lower and upper limits in which the ϕ distribution is flat. See Figure 3.20. These limits will determine the fiducial cut.

The trapezoid function is shown in Figure 3.19 and assumes the form

$$y = \begin{cases} 0 & if & & x \leq & p_1 - p_0 \\ p_4(x - p_1 + p_0)/p_0 & if & p_1 - p_0 & < x \leq & p_1 \\ p_4 & if & p_1 & < x \leq & p_2 \\ p_4(-x + p_2 + p_3)/p_3 & if & p_2 & < x \leq & p_2 + p_3 \\ 0 & if & p_2 + p_3 & < x & \end{cases}$$

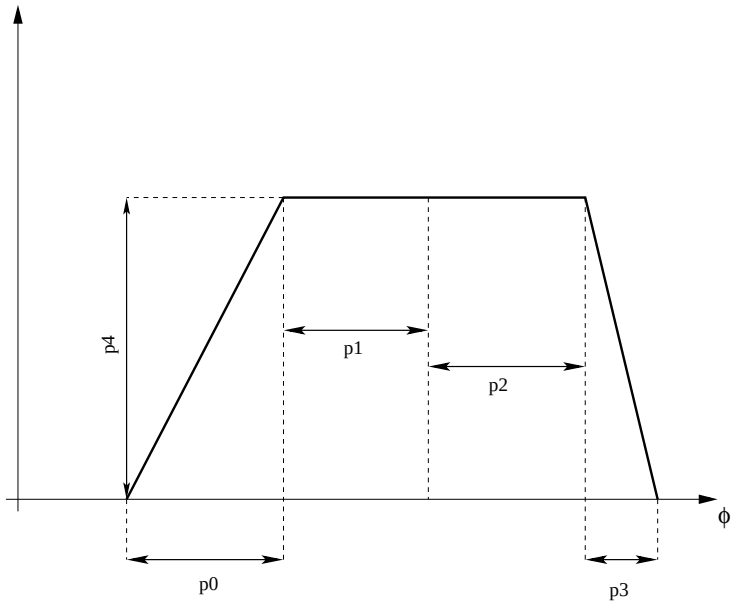

Figure 3.19: The trapezoid function used for the ϕ fit. The parameters p_1 and p_2 determine the fiducial cut lower and upper limits.

The trapezoid fit gives the parameters p_1 and p_2 described above for each θ considered in each momentum bin. These parameters are respectively the ϕ_{MIN} and ϕ_{MAX} wanted and form a $\phi(\theta)$ distribution.

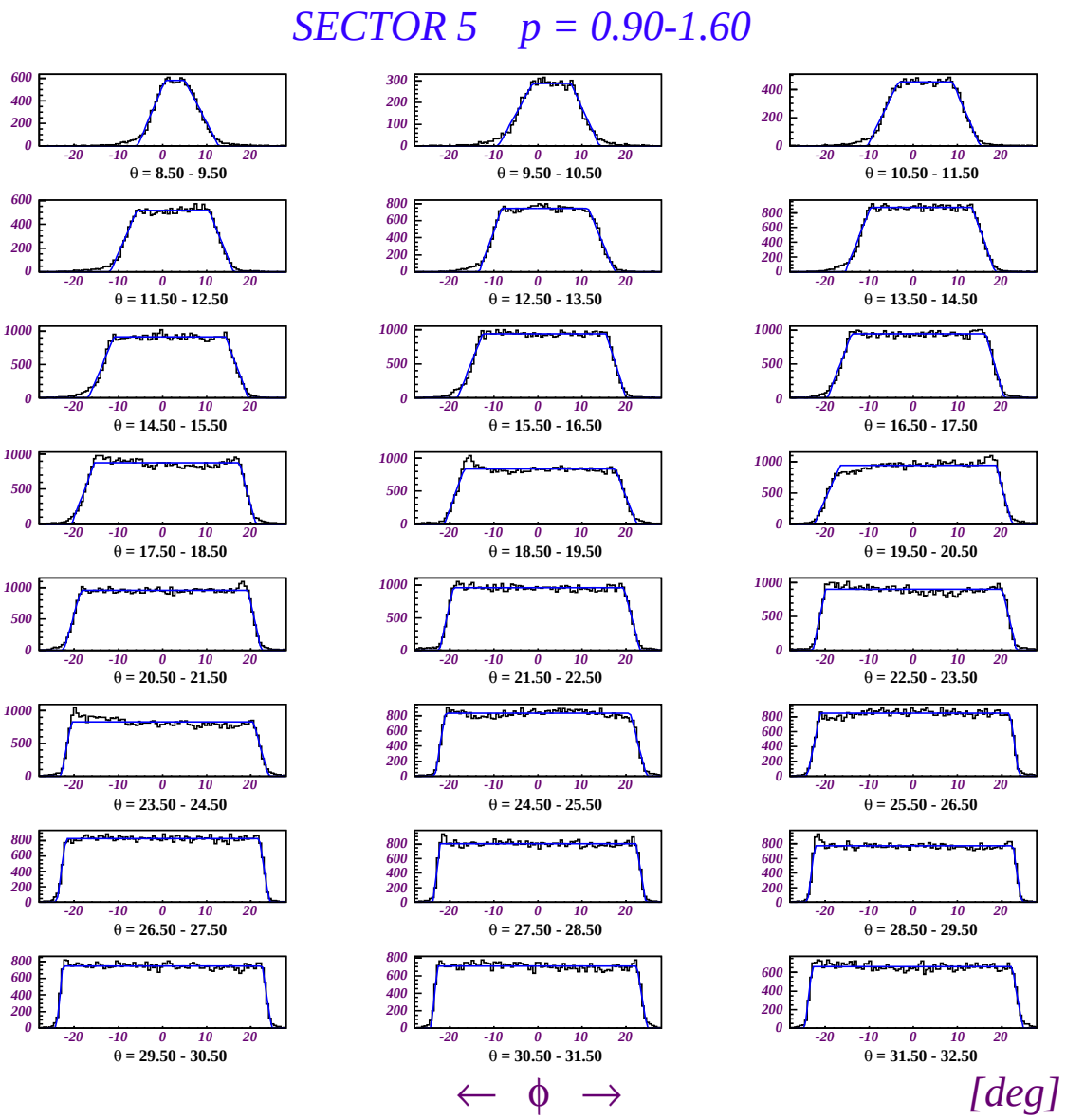

Figure 3.20: Trapezoid fit for sector 5. The limits of the flat ϕ region of each fit will determine the fiducial cut.

In order to parametrize such a function, the parameters are fitted as a function of θ with a fourth order polynomial

$$\phi_{MIN} = a_0 + a_1\theta + a_2\theta^2 + a_3\theta^3 + a_4\theta^4$$
$$\phi_{MAX} = b_0 + b_1\theta + b_2\theta^2 + b_3\theta^3 + b_4\theta^4$$

Figure 3.21 shows the calculated ϕ_{MIN} and ϕ_{MAX} and the resulting fit for sector 5 and momentum range 0.9 to 1.6 GeV.

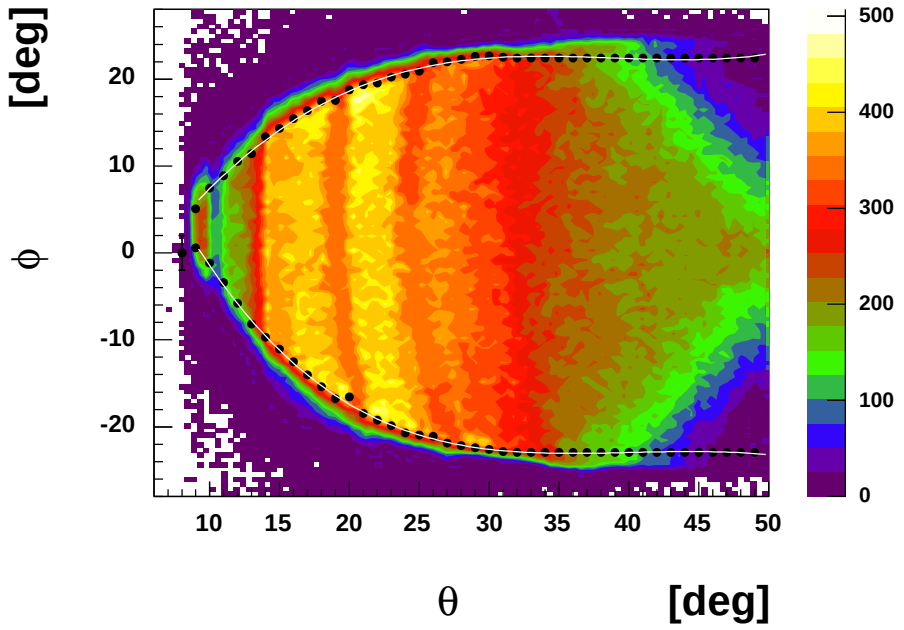

Figure 3.21: Result of the trapezoid fit for sector 5. The proton momentum ranges from 0.9 to 1.6 GeV. The black points are the parameters p_1 (negative ϕs) and p_2 (positive ϕs) for each θ slice considered as shown in Figure 3.20. The white line is a fourth order polynomial fit to the black points.

The parameters just found are momentum dependent, since a fit is made for each momentum bin.

$$\begin{aligned} a_i &= a_i(p) \\ b_i &= b_i(p) \end{aligned} \qquad i = 0..5$$

In order to exploit the momentum dependance each of these parameters is fitted as a function of p with a second order polynomial as shown in Figure 3.22.

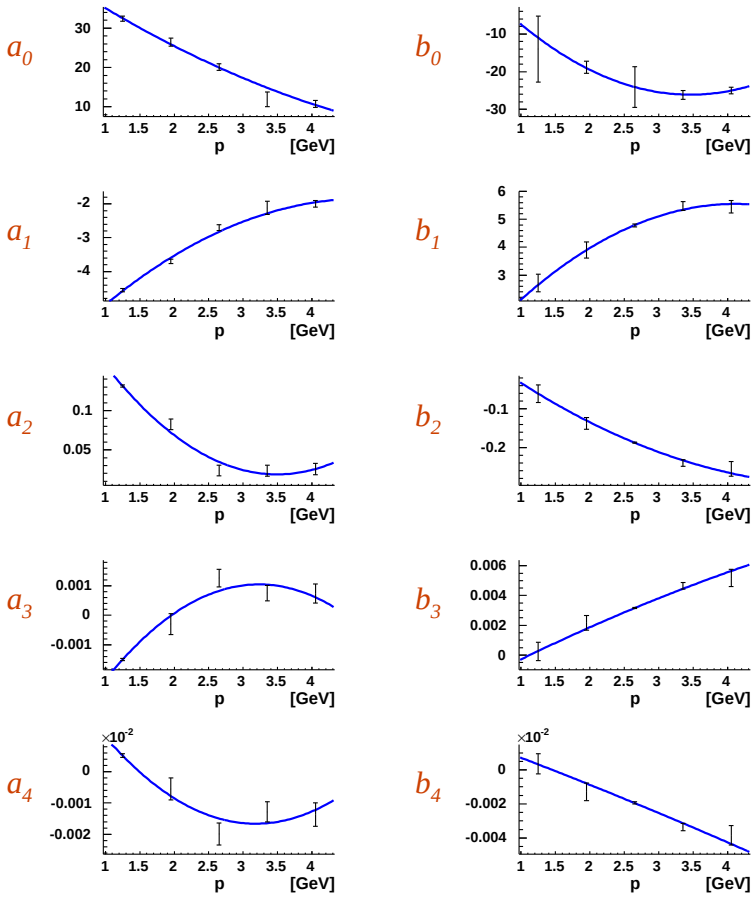

Figure 3.22: Sector 5 parameters fit. Each of the parameters is fitted as a function of the proton momentum with a second order polynomial.

The overall fiducial (shown for sector 5 in Figure 3.23) cut is finally determined, in each sector, by the limits:

$$\phi_{MIN} = \sum_{i=0}^{5} a_i(p)\,\theta^i$$
$$\phi_{MAX} = \sum_{i=0}^{5} b_i(p)\,\theta^i$$
$$\phi_{MIN} \leq \phi \leq \phi_{MAX}$$

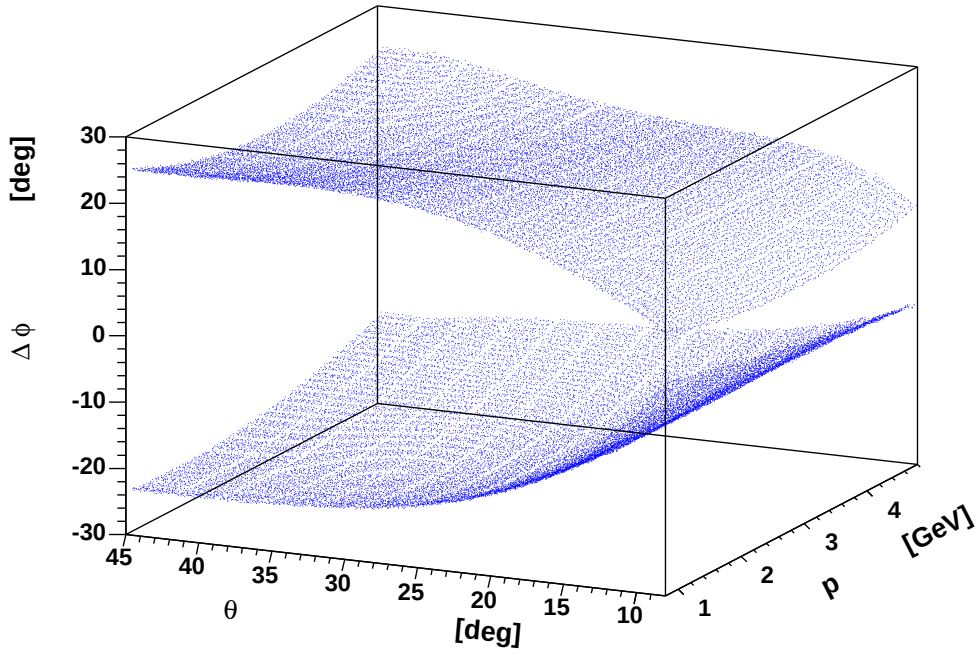

Figure 3.23: Sector 5 $\Delta\phi$ fiducial cut as a function of θ and ϕ.

3.8.2 θ versus momentum cuts

Sector 2, 3, 5 and 6 presents holes and depletions which are taken care of with the cuts shown on Figure 3.16 where θ is plotted against the momentum p.

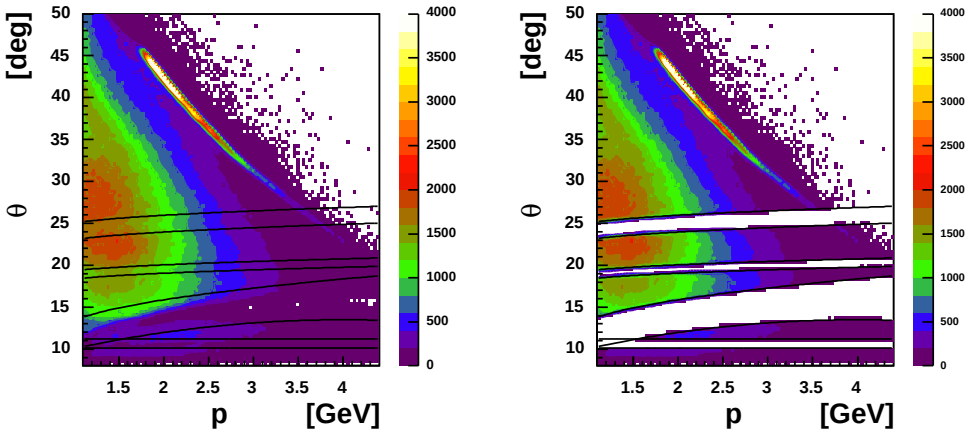

Figure 3.24: θ versus p for protons sector 5. A depletion is clearly visible and cut out.

A summary of all parameters can be found in Appendix A.1.5.

The effect of the fiducial cut on sector 5 is shown in Figure 3.25.

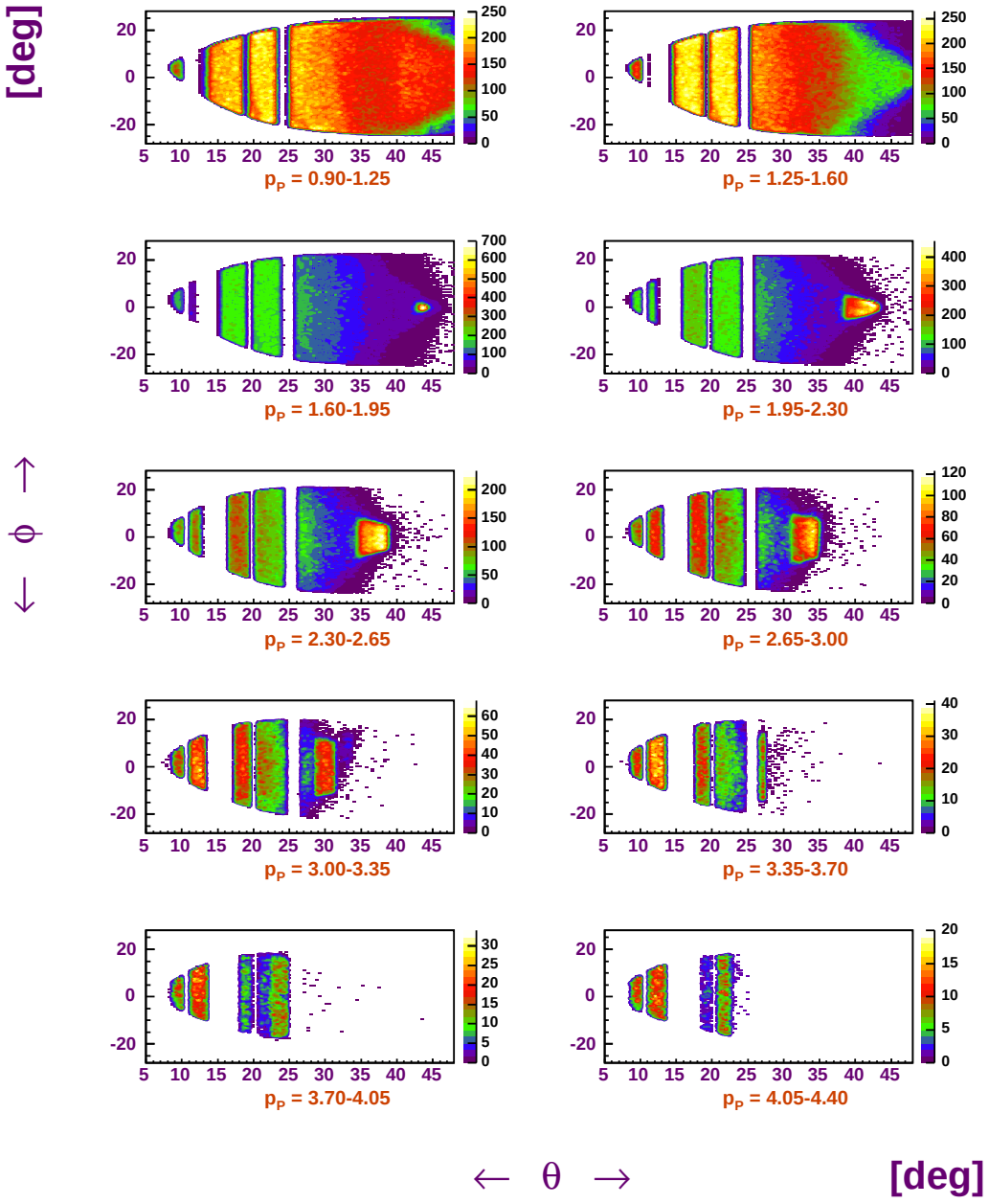

Figure 3.25: Sector 5 ϕ versus θ after fiducial cut. The empty bands in this sector are unfortunate because the forward ones occur where many protons interested to us are expected. Compare with Figure 3.18 or Figure 3.21 to appreciate the cutoff of the depletions. Notice the momentum dependance of

3.9 Kinematic corrections

The kinematic corrections presented here are based on the elastic kinematics and the incident electrons beam energy value. Both these matters are important therefore discussed below.

After selecting elastic events, systematics are found on electron and proton angles and on electron momentum. No significant error is found on proton momemtum.

3.9.1 Beam Energy measurement

The beam energy value chosen for this analysis is the result of measurements from Hall A, which has two means of computing the beam energy:

- ***e, P* method:** it is based on the angle measurement in the two bodies $^1H(e, e'P)$ kinematics.
- **"arc" method:** it is based on the use of a section of the beam transport line as a magnetic spectometer.

Both these method are used during Hall-A experiments.

During e1-6 data acquisition time such a measurement was taken on 2/11/2002 (during this experiment) and it gave as results:

$$\begin{array}{cc} e, P & 5754.41 \pm 1.76 \quad \text{GeV} \\ ARC & 5754.4 \pm 1 \quad \text{GeV} \end{array}$$

Based on the above, the beam energy value chosen for this analysis is:

$$E = 5.7544 \ \text{GeV}$$

3.9.2 Elastic selection

The $eP \rightarrow e'\,P'$ elastic reaction is useful for many purposes. The constraint allows one to determine systematic errors and corrections, on one or more variables.

The hadronic mass of the $P\pi^0$ system is close to M_P, so one can assume that those corrections hold for the $\Delta(1232)$ kinematics as well as they do for the elastic kinematics. Furthermore the elastic cross section is helpful to address eventual normalization issues.

The Bethe Heitler (B.H.) process $eP \to eP\gamma$ discussed in 3.10 is included in elastic eP events, and cuts are determined to select only low energy (soft) photons.

I present here a series of cuts for e1-6 data to achieve exclusive elastic selection after electron and proton particle ID.

W cut

The first cut, illustrated in Figure 3.27 a), is on W, the outgoing hadron mass, which for elastic scattering is the mass of the proton. A gaussian is fitted to the W distribution for each sector and 3 σ around the mean determine the W cut.

$M_x(eP)$ cut

The second cut is on the missing mass of the outgoing $e\,P$ system. See Figure 3.27 b). No particles except B.H. photons are produced during elastic scattering, therefore the missing mass must be zero. A gaussian is fitted to the $M_x(P)$ distribution for each sector and 3 σ around the mean represents the $M_x(EP)$ cut.

$\Delta\theta$ cut

The elastic constraint allow us to determine the proton angle in the lab θ^P_{calc} using only the outgoing electron angle and energy. This calculation is independent of the incident electron energy and therefore it is independent of pre-radiative effects shown on the Figure 3.26 a). The third cut is on $\Delta\theta = \theta^P_{meas} - \theta^P_{calc}$ (Figure 3.27 c) where

$$\tan\theta^P_{calc} = \frac{1}{(1+\frac{E'}{M_P})\tan\frac{\theta_{e'}}{2}}$$

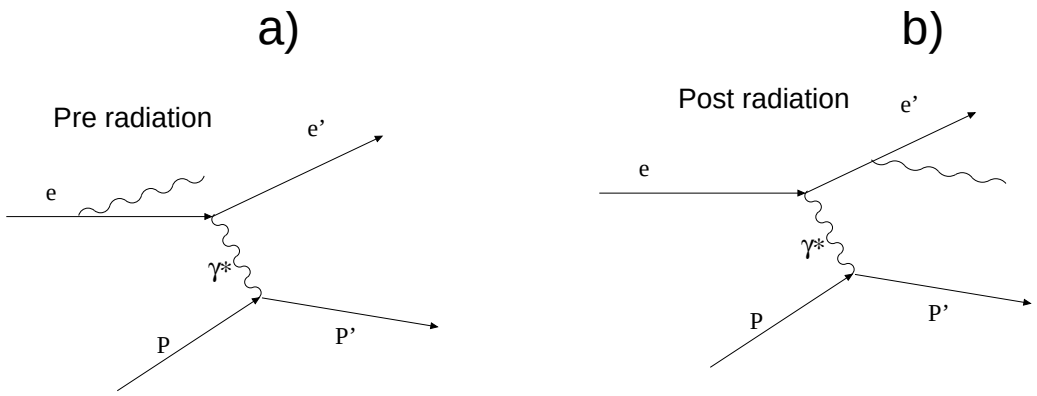

Figure 3.26: Radiative elastic events. a) pre-radiation. A photon is emitted by the incoming electron. b) post-radiation. A photon is emitted by the outgoing electron.

A gaussian is fitted to the $\Delta\theta$ distribution for each sector and 2 σ around the mean represents the $\Delta\theta$ cut.

$\Delta\theta_2$ cut

The elastic constraint allow us to determine the proton angle in the lab θ^P_{calc2} using only the incident electron energy and the outgoing electron angle. Assuming that the scattered electron doesn't change direction when it emits a photon (peaking approximation), this calculation is independent of the outgoing electron energy and therefore it is independent of post-radiative effects shown on Figure 3.26 b).

The fourth cut is on $\Delta\theta_2 = \theta^P_{meas} - \theta^P_{calc2}$ (Figure 3.27 d) where

$$\tan\theta^P_{calc2} = \frac{1}{(1 + \frac{E}{M_P - E + E\cos\theta_{e'}})\tan\frac{\theta_{e'}}{2}}$$

A gaussian is fitted to the $\Delta\theta_2$ distribution for each sector and 2 σ around the mean represents the $\Delta\theta_2$ cut.

$\Delta\phi$ cut

The fifth and final cut is on the difference between the electron and proton azimuthal angle $\Delta\phi$ (Figure 3.27 e). Both electrons and protons, in the peaking approximation and for elastic events, lie in the same plane therefore $\Delta\phi$ must be equal to π.

A gaussian is fitted to the $\Delta\phi$ distribution for each sector and two σs around the mean represents the $\Delta\phi$ cut.

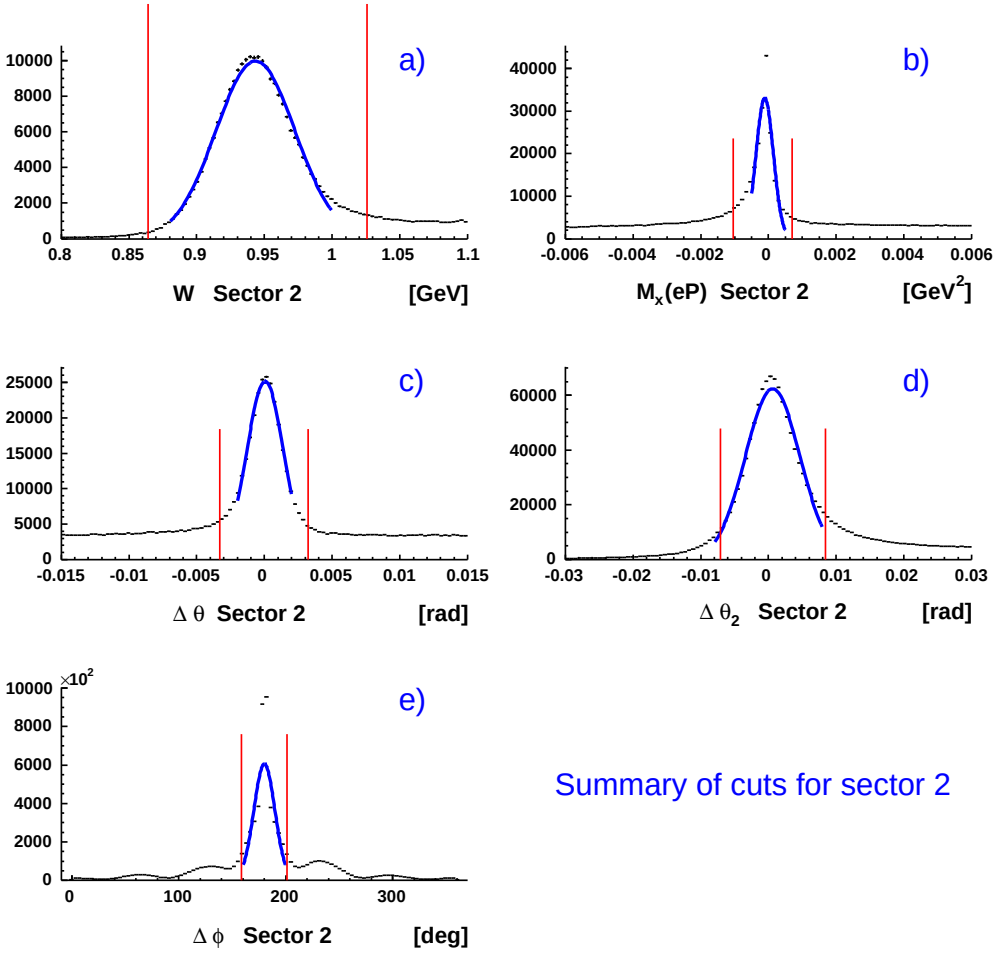

Figure 3.27: The cuts for elastic selection for sector 2. (a) W mass cut. (b) Missing (eP) mass cut. (c) $\Delta\theta$ cut. (d) $\Delta\theta_2$ cut. (e) Coplanarity cut.

3.9.3 Angle corrections

The θ angles of electrons and protons present an incorrect ϕ dependence due mainly to misalignments of the drift chambers. This error can be easily seen by looking at elastic events. In particular one can calculate the predicted beam energy E_{calc} using the angles of electron and proton with the formula

$$E_{calc} = M_P - \frac{M_P}{tan(\theta_e/2)\, tan\theta_P} \tag{3.3}$$

and look at the difference between E_{calc} and the nominal beam energy $\Delta E = E_{nom} - E_{calc}$ as a function of ϕ (see Figure 3.28).

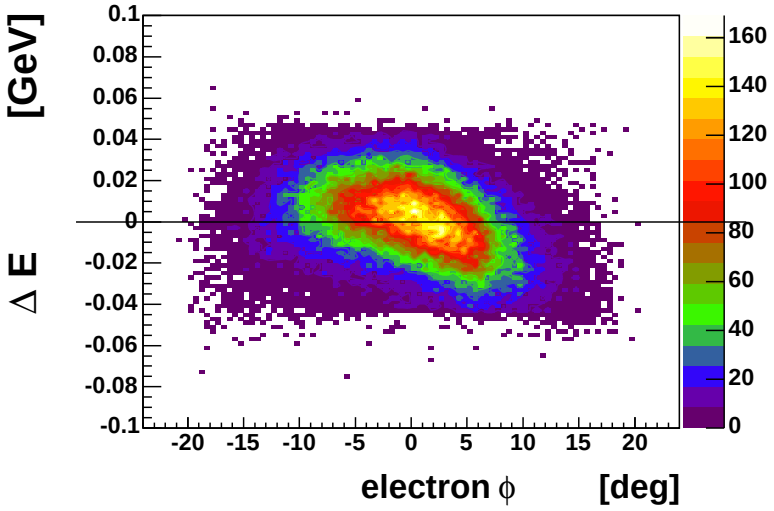

Figure 3.28: ΔE as a function of ϕ for electrons in sector3. One can see distortions as big as 30 MeV.

It turns out that the distortion is small, averaged around 0.4 mrad (0.02 degrees) and peaking at 1 mrad (0.06 degrees). However the momentum correction is based on the angle measurement. Furthermore, the boost in the $\Delta^+(1232)$ c.m. system amplifies small deviations, so the angles measurement have to be as precise as possible.

One can use (3.3) to calculate a correction. For example, one can assume that

the electron angle reconstruction is correct and calculate a correction for the proton. Or vice versa.

In the present work, it was assumed that the angle distortion comes from a DC misalignment, therefore gives similar effect on all particles. Under this assumption, all particles have (the same) systematic error on their angle measurement,

In order to calculate the correction, the theoretical correlation (3.3) between the lab angles of the electron and proton is used. Such correlation is shown in Figure 3.29.

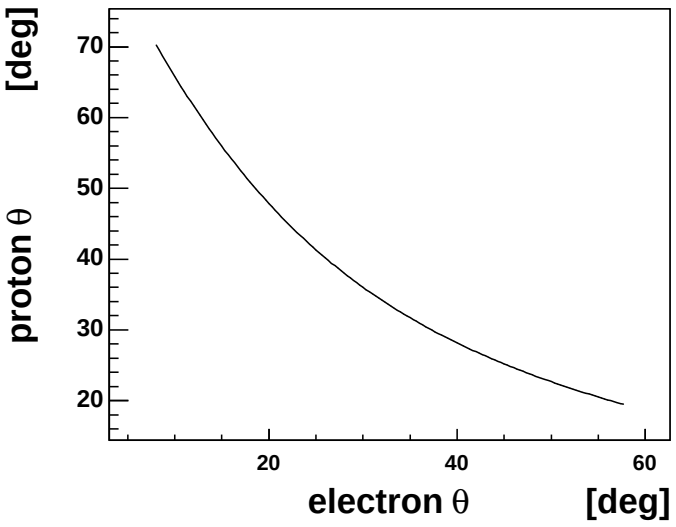

Figure 3.29: The constraint of elastic scattering: proton θ versus electron θ for elastic scattering for a 5.754 GeV beam energy.

During the experiment, the measured angle P deviates from this curve as indicate in Figure 3.30 which is a zoom of Figure 3.29. To calculate the corrections $\Delta\theta_e$ and $\Delta\theta_p$ the point **C** of the curve closest to **P** is found with an algorithm that minimize the radius of a circle with center in **P** intersecting the curve.

The corrections $\Delta\theta_e$ and $\Delta\theta_p$ for electron and proton found with this algorithm are then combined together and plotted for different θ slices in Figure 3.31. Notice that, since the correction is the same for all particles, at this point electron and proton loose their identities and "θ" is θ_e or θ_p.

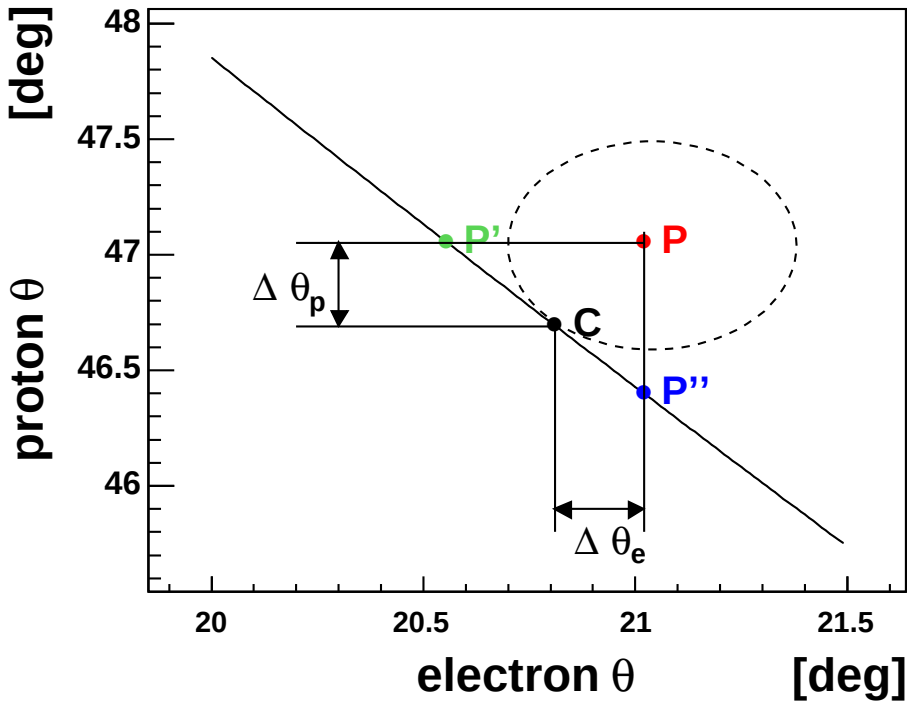

Figure 3.30: The angle correction algorithm. A measured angles of electron and protons (red point P) does not lie in the theoretical curve. The circle with center in P intersecting the curve and with minimum radius is found. Its intersection with the curve is the point C, the point of the curve closest to P. Notice that the x and y scales are different so that the circle looks like an ellipse.

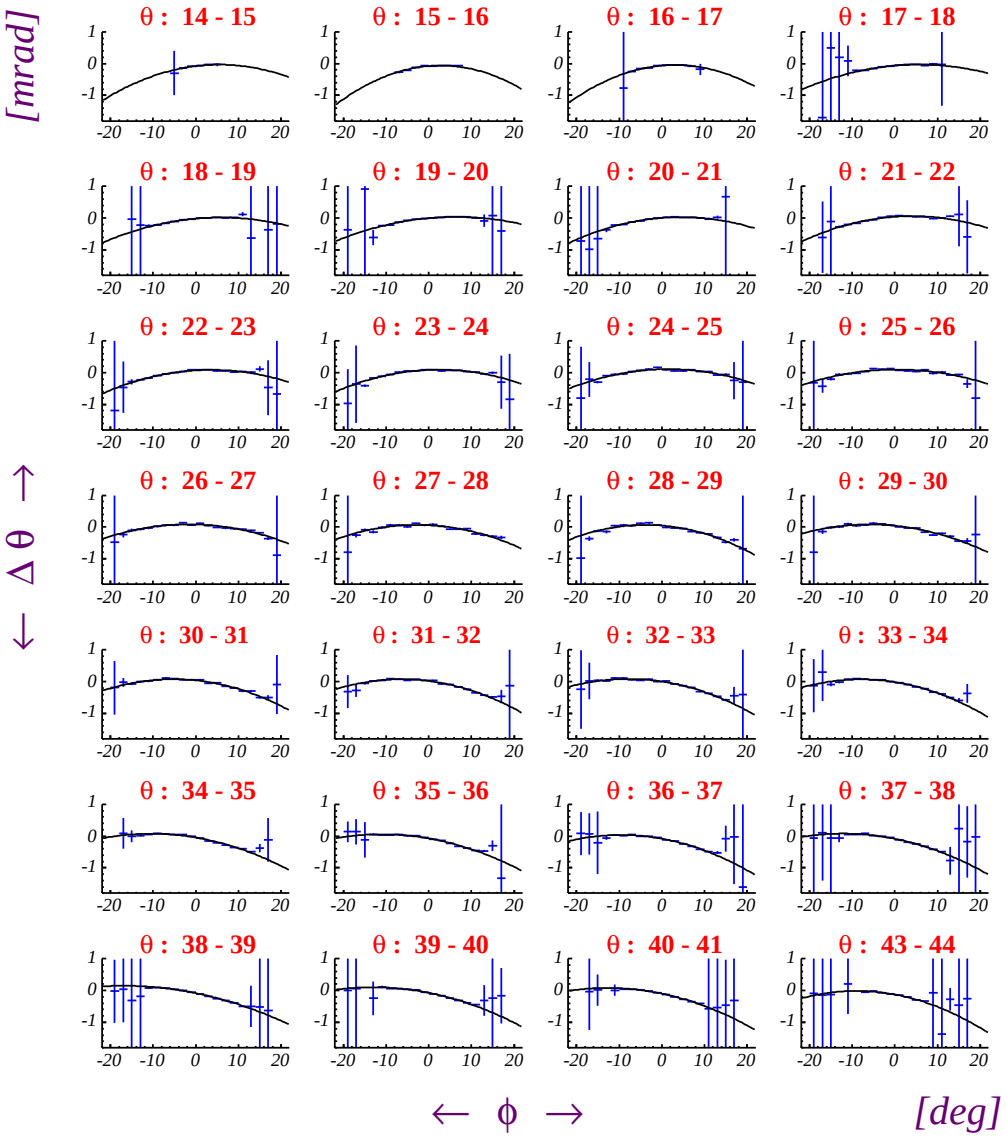

Figure 3.31: The combined angle correction $\Delta\theta$ for electron and proton for different θ slices. Each slice is fitted with a second order polynomial (black curve).

The correction is fitted with a second order polynomial, yielding three parameters for each θ slice considered:

$$a = a(\theta)\,,\ b = b(\theta)\,,\ c = c(\theta)$$

Each of the three parameters is then plotted as a function of θ in Figure 3.32. When calculating the parameters for a given θ an interpolation is used, shown in the figure in red.

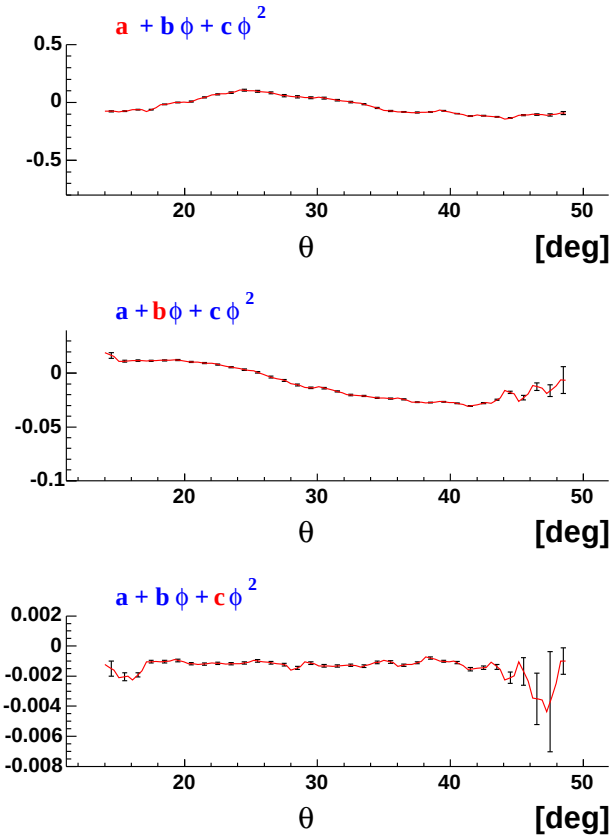

Figure 3.32: Angle correction parameters as a function of θ for sector 1. The red line is the linear interpolation of the points.

The overall angles correction $\Delta\theta$ is

$$\Delta\theta = a(\theta) + b(\theta)\,\phi + c(\theta)\,\phi^2$$

To check to quality of the correction the ΔE distribution (like the one in Figure 3.28) is plotted against ϕ before and after the correction for each sector. Figure 3.33 show the mean of the ΔE distribution.

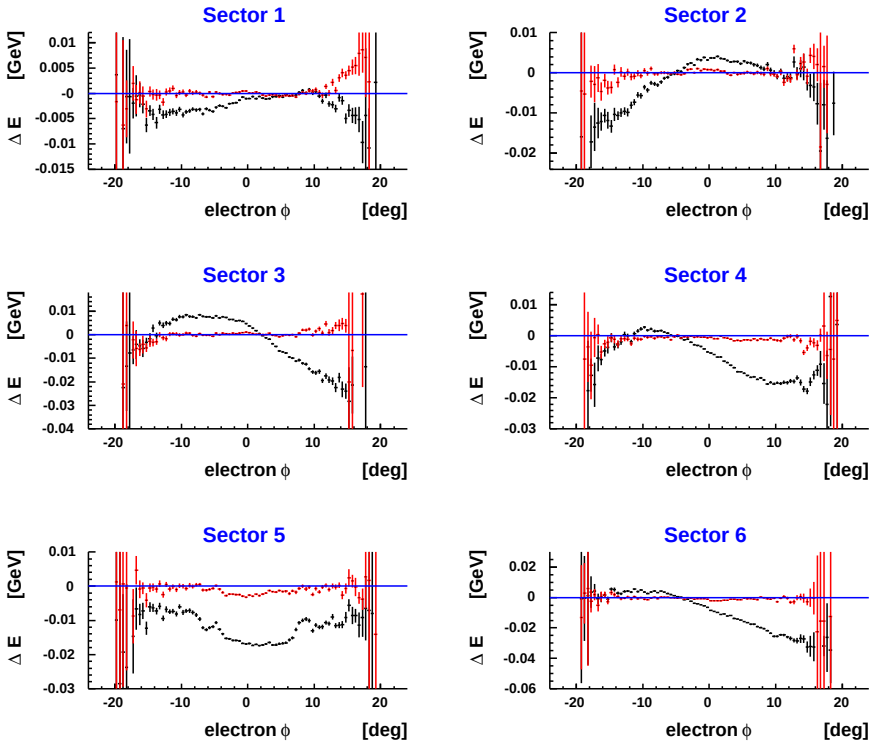

Figure 3.33: ΔE as a function of ϕ for each sector. Black: before correction. Red: after correction.

3.9.4 Momentum corrections

Drift chamber misalignment and an inaccurate magnetic field map are the main reasons why the reconstruction of the momentum is sligtly incorrect. This is reflected on quantities like W or missing mass. For example for elastic events the W distribution is distorted as seen in Figure 3.34 where it is plotted against the electron azimuthal angle in the laboratory system after angle corrections.

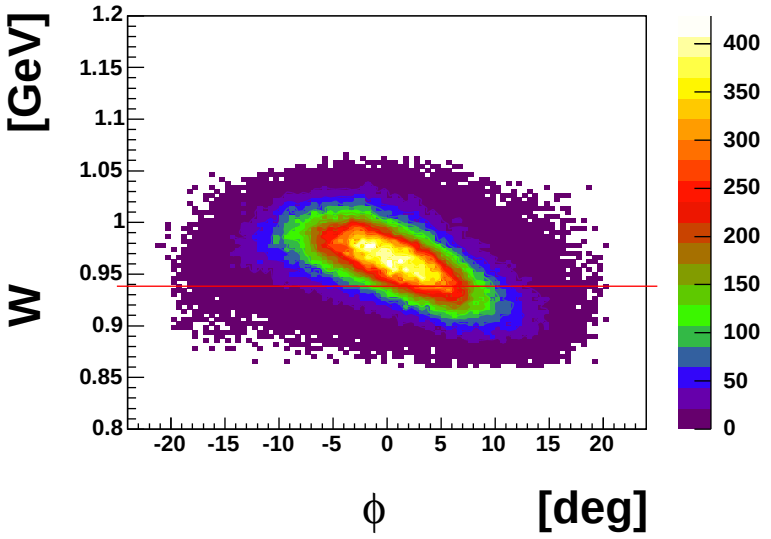

Figure 3.34: W distribution as a function of electron ϕ for elastic events after angle corrections. The red line is the mass of the proton.

The distortion turns out to depend upon ϕ and θ of the electron (and not on its momentum). Recall that for elastic events the θ and the momentum p are highly correlated[5]. Such distortion is sector dependant and needs to be corrected.

The empirical correction discussed below is based upon the elastic kinematics The mass of the $\Delta(1232)$ is close enough to the one of the proton to fairly justify applying the correction for pion electroproduction in the Δ region because the phase spaces do not differ a lot.

[5]This is not true for other reactions, where the distortion is also momentum dependent.

The quantity

$$\Delta p = p_{meas} - p_{calc} = p_{meas} - \frac{E}{(1 + E(1 - \cos\theta)/M_P)}$$

where E is the beam energy, is extracted and plotted versus ϕ for different θ slices in Figure 3.36 for sector 3. Δp is the wanted correction. Notice that Δp depends only upon the scattered electron angle.

Each Δp distribution is fitted with a third order polynomial, giving the parameters as a function of θ:

$$a = a(\theta)\,,\ b = b(\theta)\,,\ c = c(\theta)\,,\ d = d(\theta) \tag{3.4}$$

Each parameter is then fitted with a 10th order polynomial to exploit the θ dependance. The fits for sector 3 are shown in Figure 3.35.

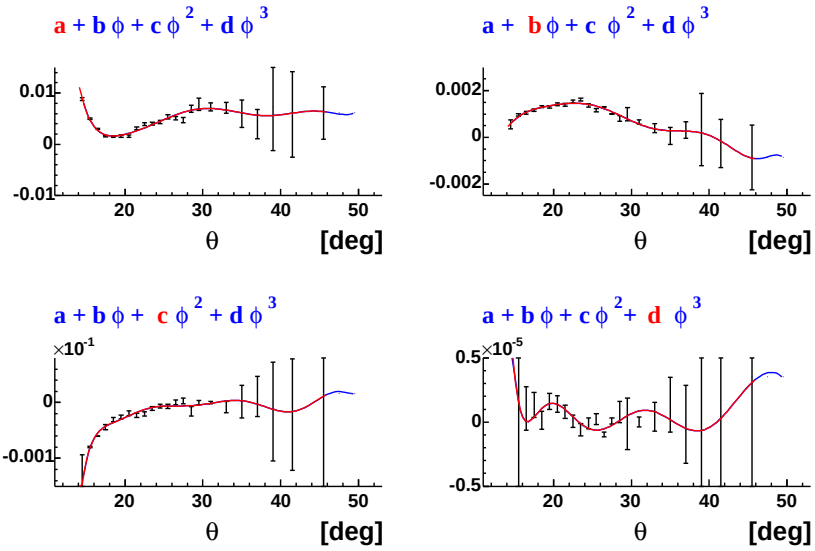

Figure 3.35: Fits of the third order polynomial parameters as a function of θ for sector 3.

The overall correction is

$$\Delta p = a(\theta) + b(\theta)\,\phi + c(\theta)\,\phi^2 + d(\theta)\,\phi^3$$

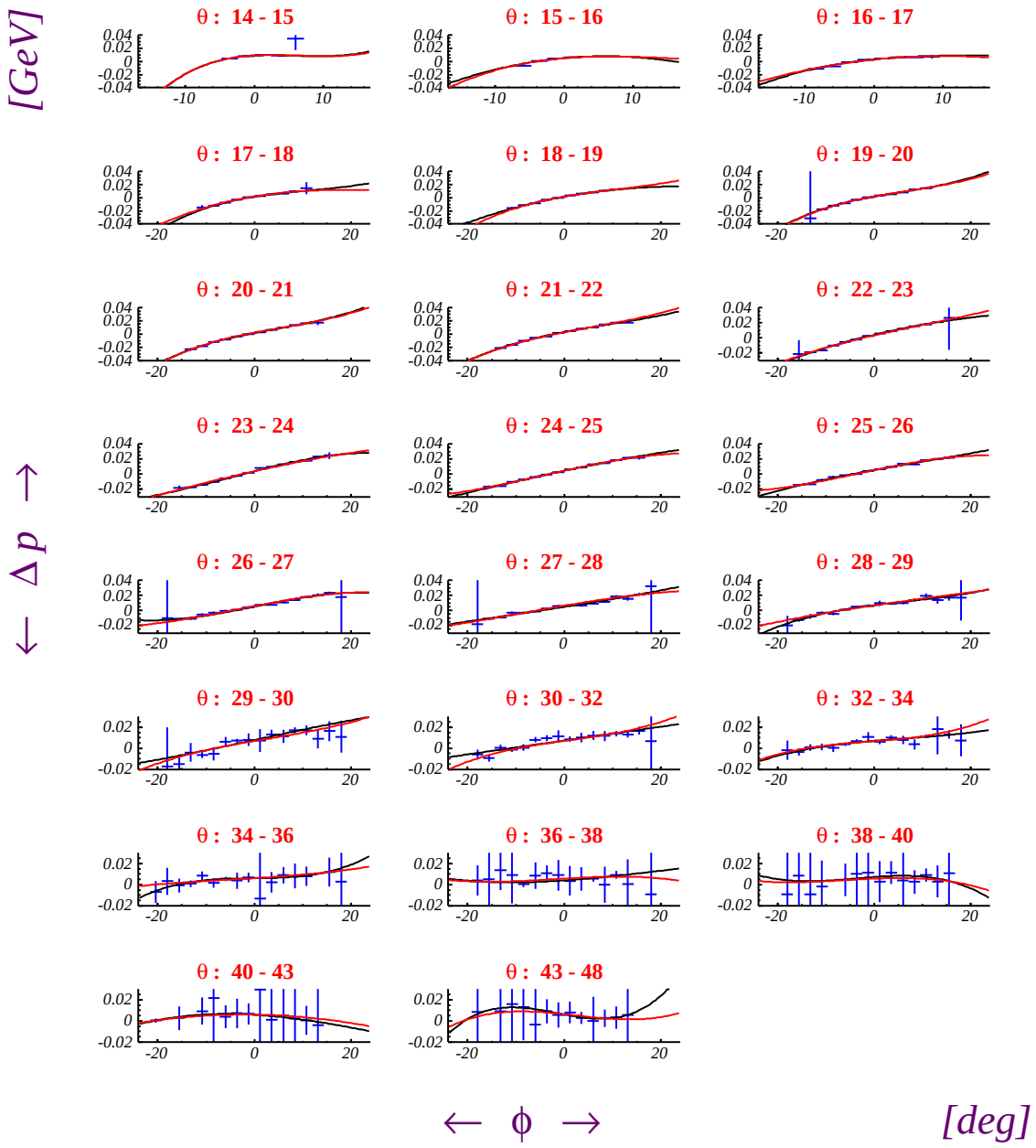

Figure 3.36: Fits of the Δp distributions for different θ slices as a function of ϕ. The black curve is the local fit to the distribution while the red one is the function coming from the global parameters 3.4. The procedures make sure that these two curves are close to each other.

The result of the correction for sector 1 is shown in Figure 3.37. One can see that the distortion disappeared and the W distribution is now centered at the mass of the proton. Similar effects are seen for all sectors.

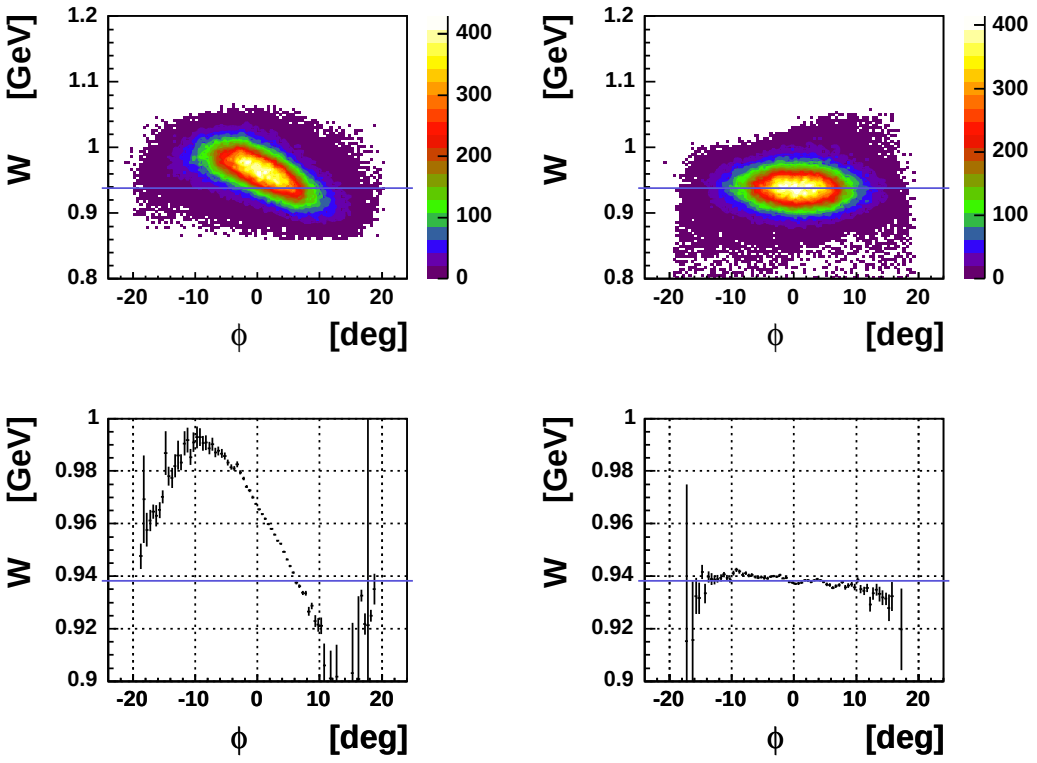

Figure 3.37: The W versus ϕ distribution for electrons in sector 1 before (left) and after (right) momentum correction. The bottom plots are the means of the top distributions sliced along W.

3.10 Bethe Heitler processes

Figure 3.38 shows the (e, P) missing mass M_X^2 versus W distribution for the whole e1-6 period after particle ID, vertex fiducial cuts and kinematic corrections. The elastic and Bethe Heitler (B.H.) events, illustrated in Figure 3.39, are clearly seen at $M_X^2 = 0$, with the characteristic increase of the cross section at high W. Also shown are the $S_{11}(1535)$ resonance decaying in η, the $P_{13}(1720)$ resonance decaying in ρ and the subject of this analysis, the $\Delta_{33}(1232)$ resonance decaying in π^0.

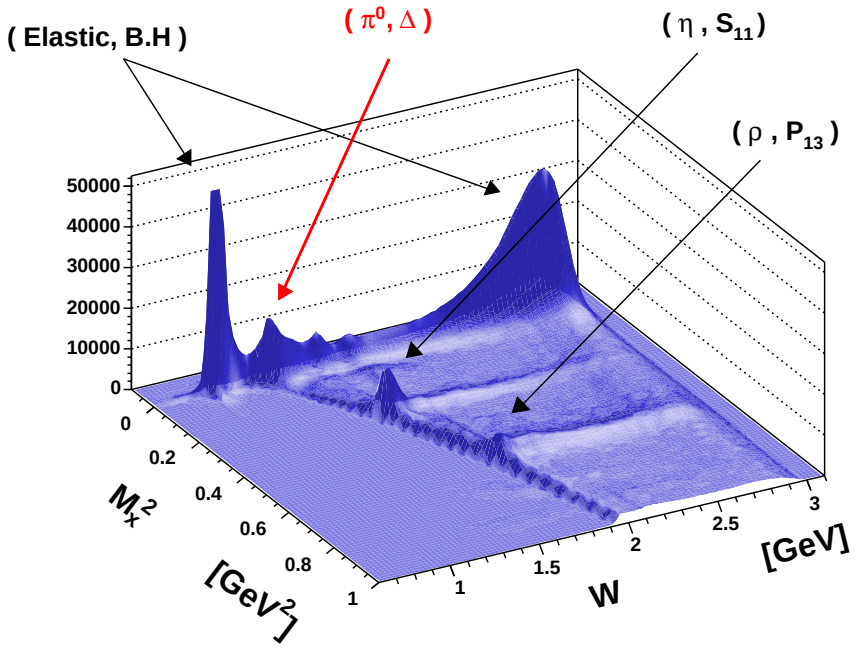

Figure 3.38: Missing mass M_X^2 versus W after particle ID, vertex fiducial cuts and kinematic corrections for the whole e1-6 data. Clearly visible are the elastic and B.H. events, the $S_{11} \rightarrow \eta$, the $P_{13} \rightarrow \rho$ and of course the $\Delta_{33} \rightarrow \pi^0$ events.

To isolate the $p(e, e'p)\pi^0$ reaction a missing mass technique alone cannot separate the B.H. processes from the π^0 events efficiently because of the limited resolution. What follow is the investigation of the kinematic cuts used to remove the B.H. events from the inelastic data.

An important assumption used to identify B.H. events is the so called *peaking approximation*. It means that the direction of the emitted photon in reaction like the ones shown in Figure 3.39 a) and b) is the same as the electron. Therefore the electron does not change direction when radiating a photon, although it can change energy. This approximation describes well most electron B.H. events [21].

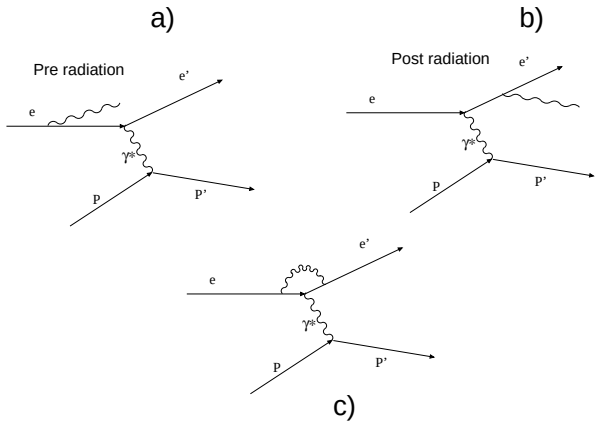

Figure 3.39: Bethe Heitler events contributing to the (eP) final state leaking into the π^0 missing mass.

The variables used for the separation are:

- $\boldsymbol{M_x}$: missing mass squared of the final state (eP).
- $\boldsymbol{\Delta\theta = \theta^P_{meas} - \theta^P_{calc}}$: θ^P_{meas} is the measured proton angle and θ^P_{calc} is the proton angle calculated from the outgoing electron energy and angle (see Section 3.9.2). In the peaking approximation, $\Delta\theta$ is independent of **pre-radiation** processes line the ones in Figure 3.39 a) and it assumes the value zero for elastic and B.H. events.
- $\boldsymbol{\Delta\theta_2 = \theta^P_{meas} - \theta^P_{calc2}}$: θ^P_{meas} is the measured proton angle and θ^P_{calc2} is the proton angle calculated from the incoming electron energy and outgoing electron angle (see Section 3.9.2). In the peaking approximation, $\Delta\theta_2$ is independent of **post-radiation** processes line the ones in Figure 3.39 b) and it assumes the value zero for elastic and B.H. events.

- $\phi_P^{c.m.}$: the azimuthal angle of the proton in the resonance center of mass, equal to π for B.H. events in the peaking approximation.

The contamination is W dependent, so eight bins in W have been considered from 1.08 to 1.48 GeV. Three cuts have been used in series as described below.

The $\phi_P^{c.m.}$ of the elastic events narrows in ϕ and broadens in M_x^2 as W increases as it is shown in Figure 3.40 where it is plotted against the missing mass M_x^2. The first cut, represented by the black curve in Figure 3.40, is composed by:

- A circle whose radius and center vary with W.
- A hyperbole $y = \pi \pm \frac{a}{x - x_0}$ whose a and x_0 vary with W.

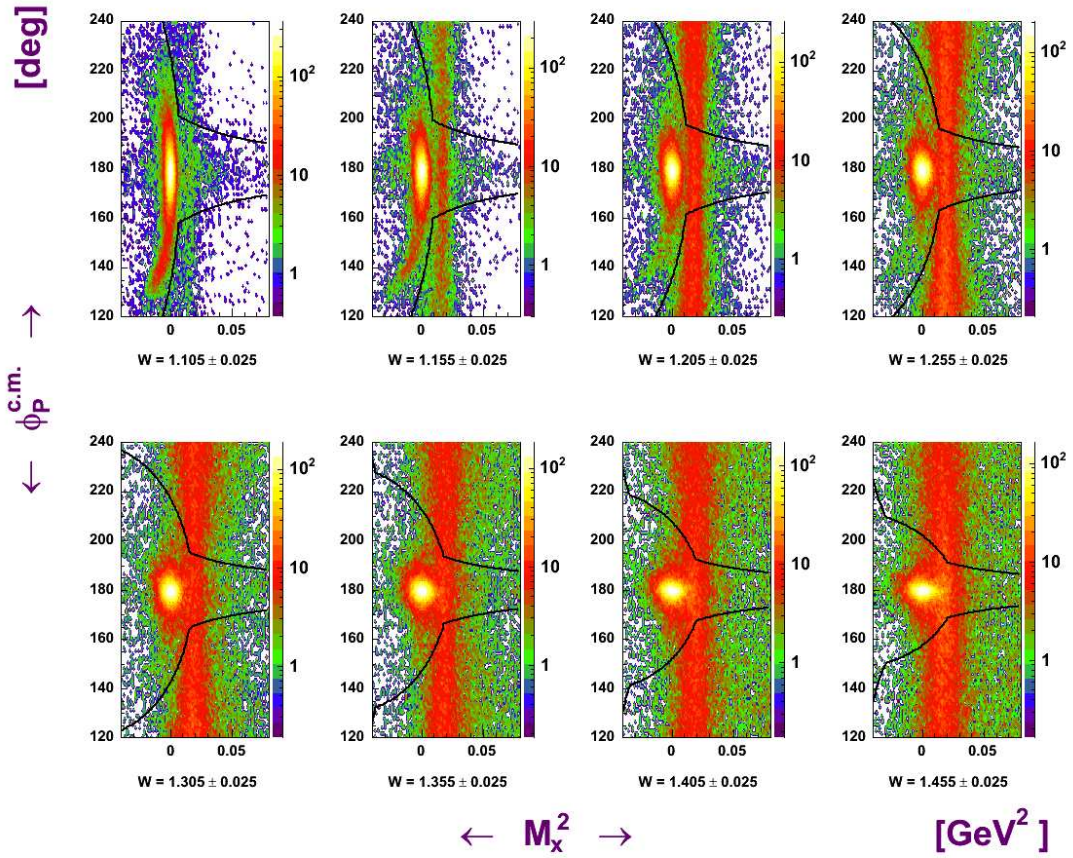

Figure 3.40: $\phi_P^{c.m.}$ versus missing mass M_x^2 for different W values.

One can immediately notice that the cut used eliminate some π^0 around $\phi_P^{c.m.} = 180^0$. These events (and the ones eliminated with the second and third cut below) will be recovered with the MonteCarlo simulation because the exact same cut will be applied (see section 4.3). The closer to data the model used for the simulation, the more accurate will be this recovery.

In Figure 3.41 is plot the missing mass M_x^2 versus $\Delta\theta$ distribution. One can see the pre-radiative events showing at $x = 0$ and leaking in the π^0 events (horizontal band at $M_x^2 \simeq M_{\pi^0}^2 = 0.0182\text{GeV}^2$. The (moving with W) spot on the left refers to post radiation events.

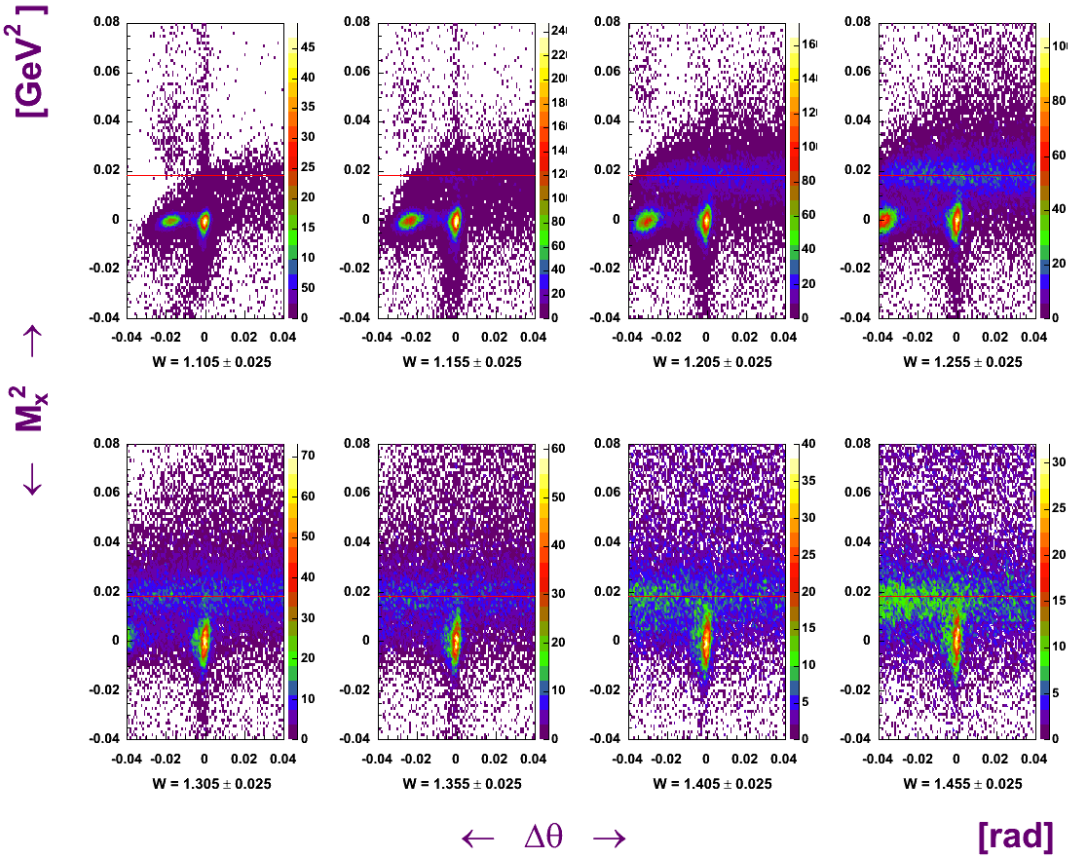

Figure 3.41: missing mass M_x^2 versus $\Delta\theta$ for different W values before the $\phi_P^{c.m.}$ versus missing mass M_x^2 cut. The pre-radiative elastic events peak at $x = 0$, while the other spot on the left refers to post radiation. The horizontal line is at the π^0 mass.

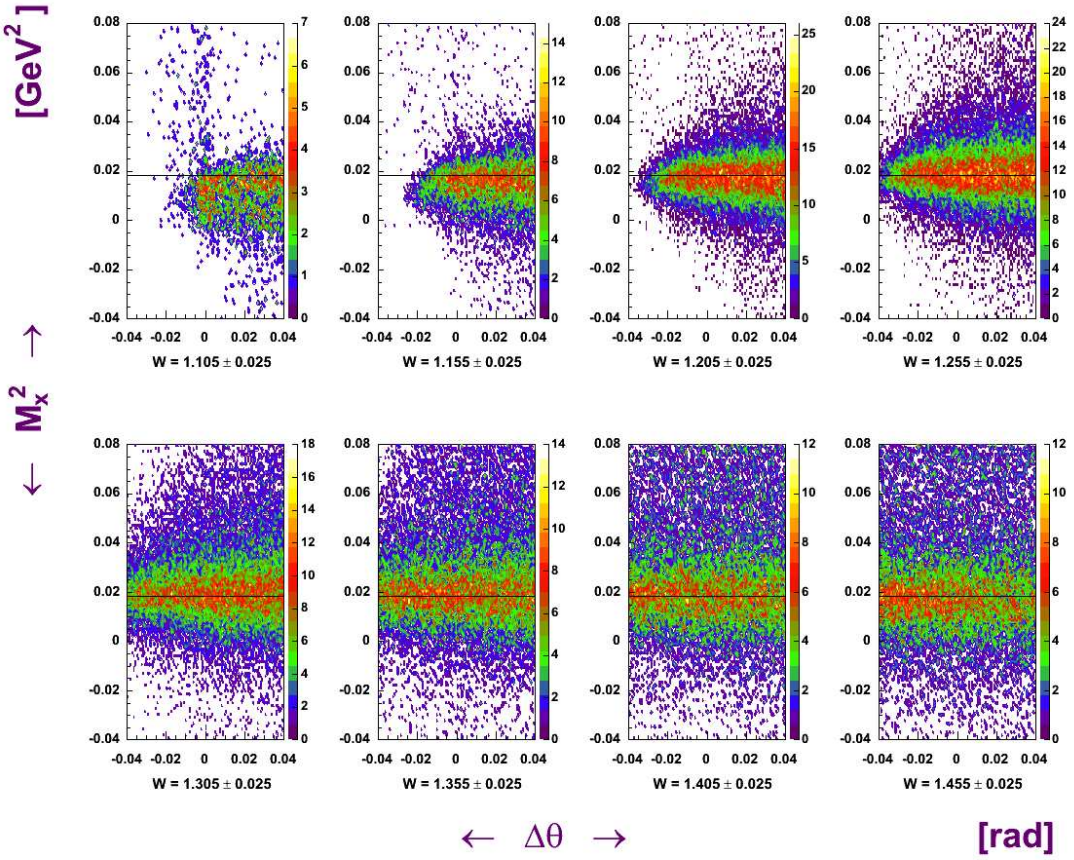

Figure 3.42: missing mass M_x^2 versus $\Delta\theta$ for different W values <u>after</u> the $\phi_P^{c.m.}$ versus missing mass M_x^2 cut. The horizontal line is at the π^0 mass.

Figure 3.42 shows the effect of the first cut on the missing mass M_x^2 versus $\Delta\theta$ distribution. Most of the pre and post radiative events are eliminated but some residual pre-radiative B.H. events at low W survives at low W

For this reason a second cut is introduced:

$$|\Delta\theta| < 0.01 \text{ rad} \quad \text{when} \quad W < 1.21 \text{ GeV} \tag{3.5}$$

Some residual post radiative B.H. events survive the first and second cut. This can be seen in Figure 3.43 where missing mass M_x^2 is plotted versus $\Delta\theta_2$: a small band shows up at $\Delta\theta_2 \simeq 0$, particularly at low W.
The third cut considered, involving missing mass M_x^2 versus $\Delta\theta_2$, is:

$$M_x^2 < a + b\,\Delta\theta_2$$

where a, b vary with W.

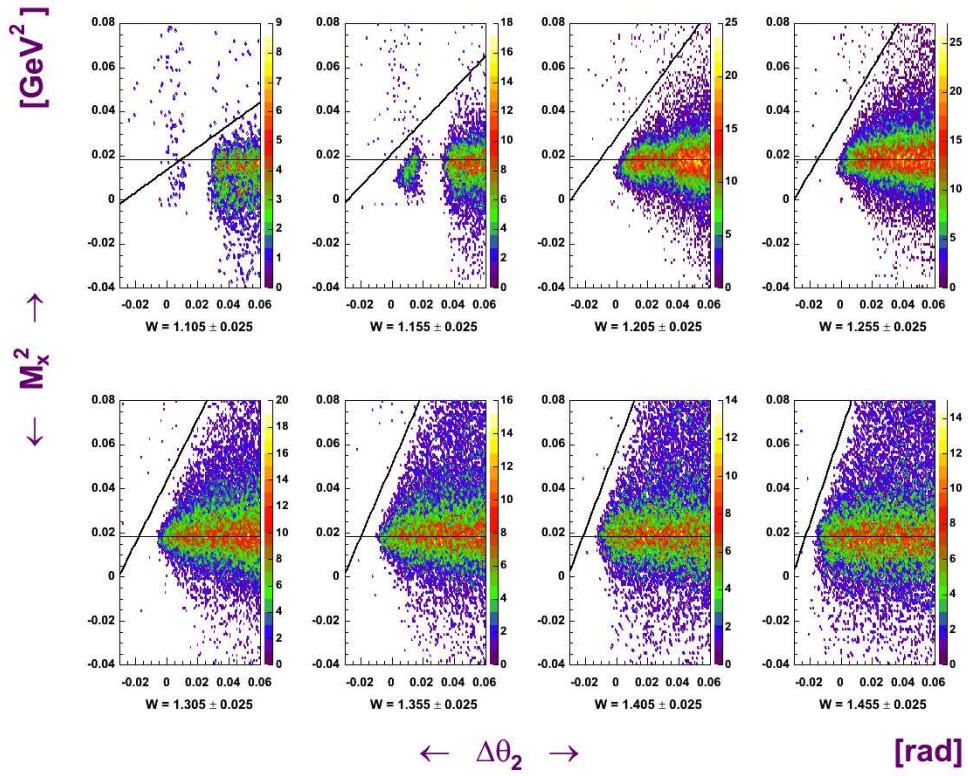

Figure 3.43: missing mass M_x^2 versus $\Delta\theta_2$ after the first two B.H. cuts. Residual post-radiative events are cut out with a straight line $y = a + bx$ whose parameters a and b vary with W. This plot shows also the effect of the second cut (3.5): at low W events with $\Delta\theta \simeq 0 \equiv \Delta\theta_2 \simeq 0.025$ disappeared. The horizontal line is at the π^0 mass.

After the three cuts described above a "clean" sample of π^0 events is ready for analysis. This is shown in Figure 3.44 where W and missing mass M_x^2 are plotted in blue for the events surviving the cuts.

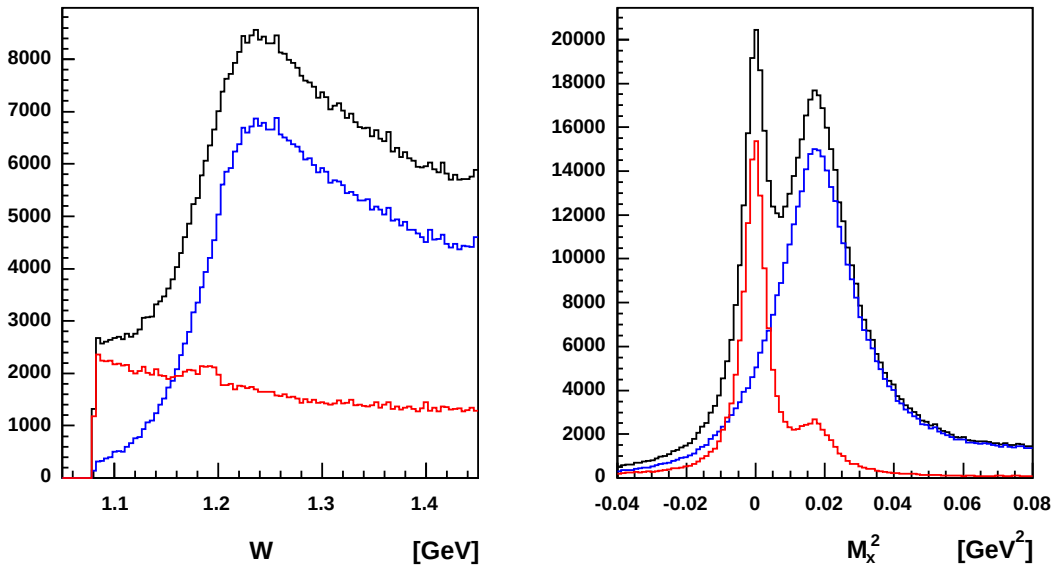

Figure 3.44: The effect of all the cuts on the W and missing mass M_x^2 distributions. Black line: before any cut. Red line: B.H events. Blue line: final π^0 events.

3.11 Čerenkov efficiency

CHAPTER 4
Acceptance

4.1 Geometrical acceptance

A geometrical acceptance is calculated using a Monte Carlo technique. Events are generated flat in the variables W, Q^2, $\cos\theta^*$, ϕ^*, ϕ_e, then the following quantities are calculated (see section 1.1 for the meaning of the quantities)

$$\nu = q_0 = \frac{W^2 + Q^2 - M_P^2}{2M_P} \Rightarrow E' = E - \nu$$

$$\theta_{e'} = acos(1 - \frac{Q^2}{2EE'})$$

$$p^*_{\pi^0} = p^*_P = \frac{\sqrt{(W^2 - (M_P + M_{\pi^0})^2)(W^2 - (M_P - M_{\pi^0})^2)}}{2W}$$

so that the proton four momentum in c.m. and the electron four momentum in the lab e'_μ are obtained. A Lorentz transformation from the resonance system to the lab system gives the proton four momentum in the lab P'_μ.

The e'_μ and P'_μ four vectors are then submitted to the same cut applied for real data that make use of four vector momentums, which are the fiducial cuts (sections 3.7 and 3.8) and the B.H. cuts (section 3.10) and the acceptance A is calculated for each bin described in 5.1:

$$A = A(W, Q^2, \cos\theta^*, \phi^*) = \frac{\#\ accepted\ events}{\#\ thrown\ events}\ (W, Q^2, \cos\theta^*, \phi^*)$$

This method is convenient because it is very fast: billions of events can be processed in only a few hours. However it doesn't take into account the detector response. Effects like bin migration, multiple scattering, finite momentum resolution, etc do not enter in this model. Yet, the geometrical acceptance could be a good approximation for a real acceptance calculation. Figure 4.1 show an example of acceptance distribution as a function of $\cos\theta^*$ and ϕ^*.

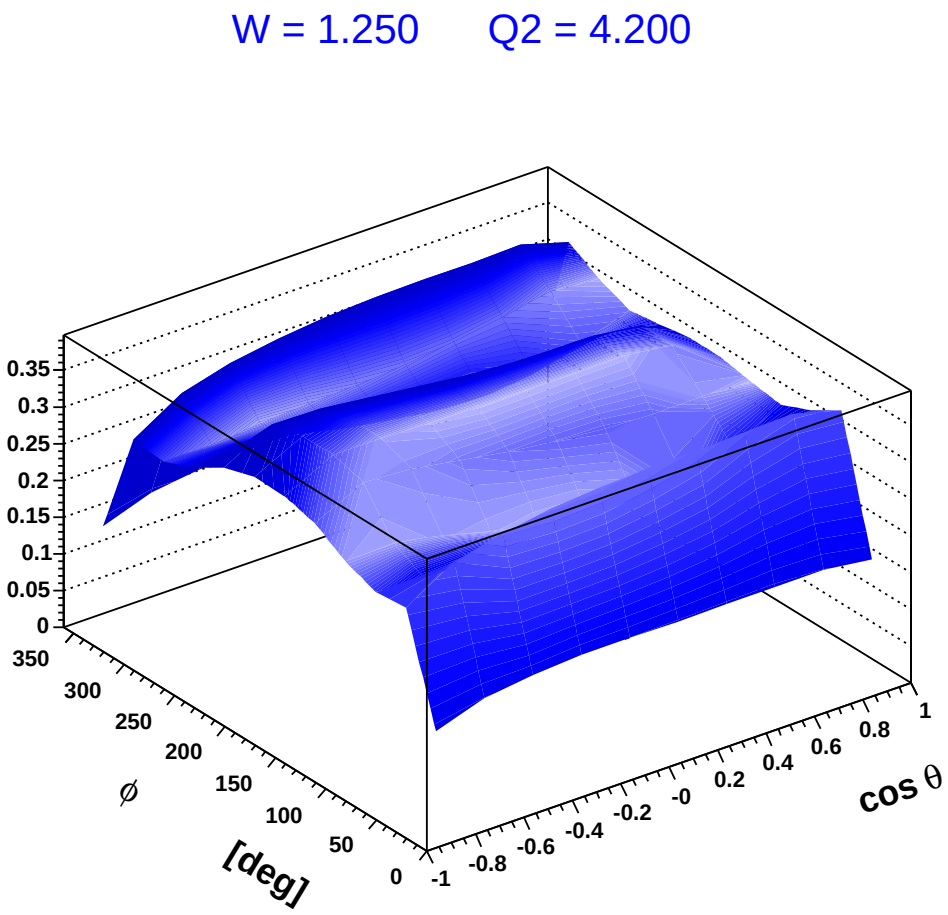

Figure 4.1: Geometrical acceptance for $W = 1.25 \pm 0.01$ GeV and Q^2 from 3.79 to 4.52 GeV^2 as a function of $\cos\theta^*$ and ϕ^*. The B.H. cut affects the distributions at $\phi^*_{\pi^0}$ extremes (0^0 and 360^0) because it cuts out events with $\phi^*_P \sim 180^0$ (the pions and the proton have opposite momentum in the c.m.).

4.2 MonteCarlo simulation

A realistic acceptance calculation must take in account the CLAS detector geometry, efficiency and resolution. A program that simulate the response of CLAS is **GSIM** (**G**EANT **Sim**ulation) based on the GEANT 3 libraries developed at CERN. What follows are the steps to achieve the desired simulation.

4.2.1 Drift Chamber smearing

4.2.2 Time of flight smearing

The GSIM simulation of the Time of Flight detector presents finer resolution than for real data. This is shown in Figure 4.2 where the TOF proton mass M calculated as in Section 3.5 is plotted for real data and MonteCarlo events. Since the proton identification is based on M, it is important that the simulation reproduces this quantity precisely.

It turns out that the mean position of M differs from data and simulation due to a not perfect calibration. This is not important because the cuts can be shifted as well. However the simulation should show the same resolution if one wants to

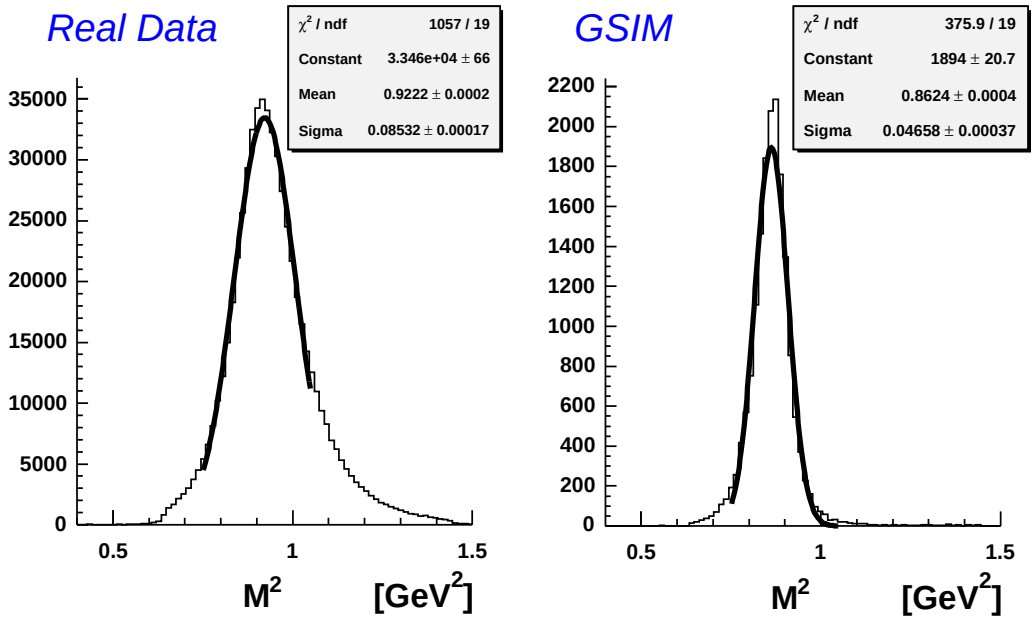

Figure 4.2: Time of flight mass M^2. Left: real data π^0 events. Right: MonteCarlo maid 2000 simulation. The mean position is different due to not perfect calibration. The MonteCarlo show a finer resolution: $\sigma_{REAL} = 0.085$ GeV^2 while $\sigma_{GSIM} = 0.047$ GeV^2.

make sure that the background is handled in the same way as the real data. In order to smear the GSIM TOF a realistic σ from a calibration study [30] shown in

Figure 4.3 was used. The function shown in the plot makes sure that the response of the MonteCarlo TOF resembles the real data case.

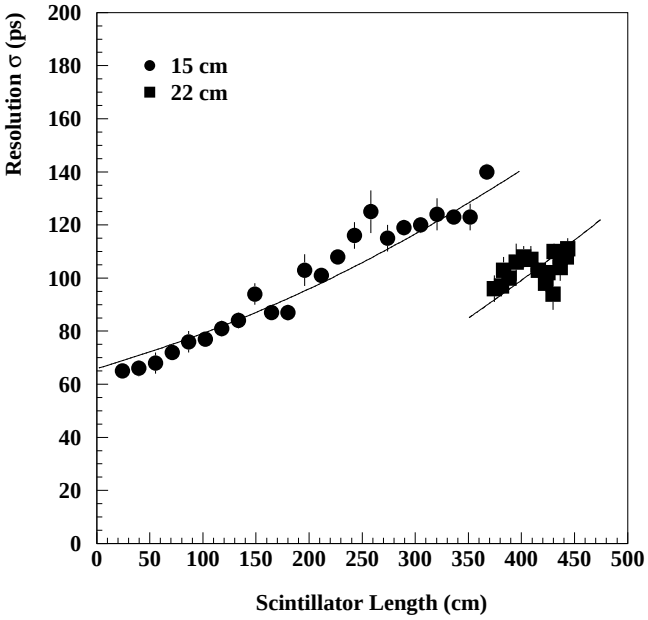

Figure 4.3: The timing resolution as determined from cosmic ray tests (see [30] for details). The curve represent the resolution (for two different paddle sizes) used to smear the MonteCarlo TOF response.

In order to perfectly match the real data and MonteCarlo TOF resolution 11 simulations of 20,000 events each were performed. In each simulation the function in Figure 4.3 was multiplied by a trial number f (from 0.5 to 1.4) and used to smear the TOF signal. In each case the resulting TOF mass was fitted with a gaussian and the obtained σ are plotted versus the multiplicative number f in Figure 4.4 where the real data σ is also plotted. One can clearly see that σ is proportional to f.

The value $f = 1.35$ matches the real data resolution and that is the value used throughout all the GSIM simulation.

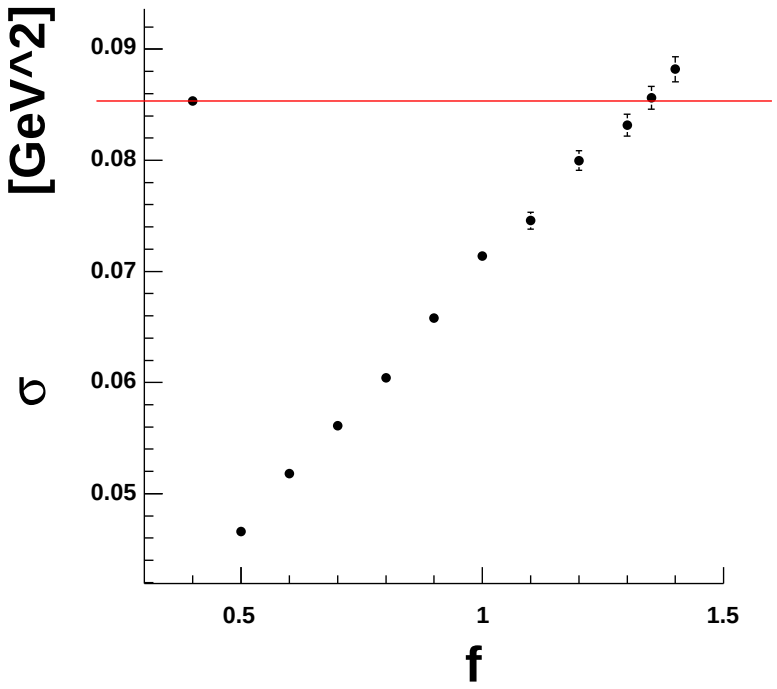

Figure 4.4: σ as a function of the smearing factor f. The first point is the real data resolution (red line). The real resolution is matched when $f = 1.35$.

4.2.3 Drift chamber inefficiencies

The Drift chamber present inefficiencies whose the MonteCarlo simulation must properly take into account for a correct acceptance calculation. As the D.C. is repaired or fails with time, each experiment have a different drift chamber phenomenology. Actually even during the same experiment a new "hole" may appear in the middle of the run. What follow is the description of the work apt to exploit at once the D.C. inefficiency and its time dependency: the calculation of a global D.C. efficiency.

Each CLAS sector has the same drift chamber configuration, shown in table 4.1: 3 separate regions containing a total of 34 layers of sense wires. Region 1 has four layers, region 2 and 3 have six layers each.

Layer	1	2	3	4	5	6	7	8	9	10	11	12
Region 1	130	130	130	130	0	0	142	142	142	126	121	120
Region 2	184	185	186	187	188	189	189	189	190	191	192	192
Region 3	192	192	192	192	192	192	192	192	192	192	192	192

Table 4.1: Number of wires in each layer. Region 1 has only 4 layers, so layers 5 and 6 are phantom.

Figure 4.5 show the occupancy of the drift chamber in sector 6 for the e1-6 experiment. There are nearly no counts in layers 34-35-36 and wire number ≈ 150. This is an example of a "hole". During tracking, a hole could affect track reconstruction because a minimum number of wires are required to define a track.

Wires that count significantly more than neighboring ones are "hot". Track reconstruction is basically undisturbed by them[1]. A third pathology is represented by wires that count less than neighboring ones but not *substantially less*. For example, a wire can count an average of 70% relative to its neighbours. Such wires can

[1]This is an empirical statement.

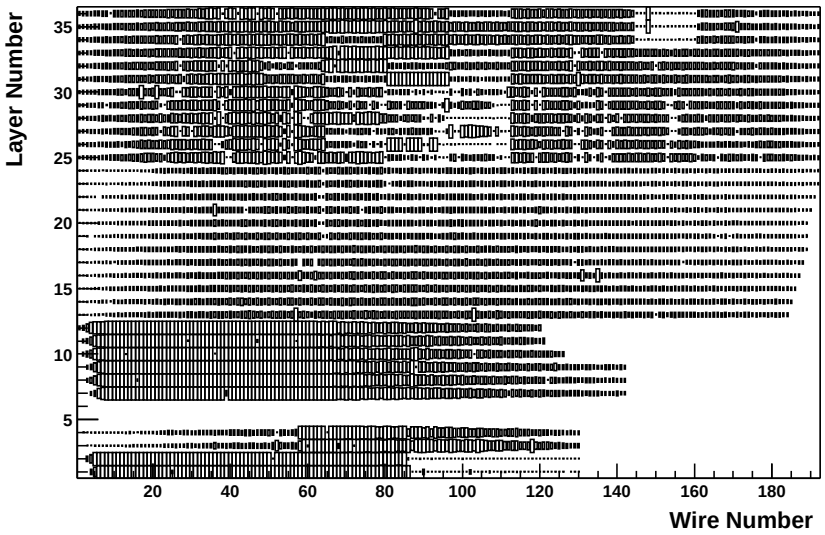

Figure 4.5: Drift chamber occupancy distribution for sector 6. A hole is visible in layers 34-35-36 and wire number $\approx$ 150.

be considered "warm" wires. Warm wires could be correlated due to common electronics. For example they could be attached to the same (defective) ADB board[2], so that all wires in that board have *the same efficiency at the same time*. Correlated wires affect tracking in that a group of wires might miss at the same moment, preventing the creation of a track segment. Treating warm wires systematically as holes results in the loss of particle tracks. Another pathology is represented by wires that are alive during part of the run and dead during another part of the run.

In order to calculate the efficiency of a wire, the whole e1-6 period has been considered. If a wire results having 50% efficiency it could mean that

- its efficiency is 50%.
- the wire was alive for hald the experiment and dead for the other half.

so that the time dependancy problem of the D.C. has been been solved.

For each $w(i, S)$ of the $36,000$ wires, i being the wire index and S its sector, a sample of 18 wires have been considered: its next neighbors in the same sector

[2]An ADB board is a power supply unit. With a $60Hz$ varying gain of threshold it might give a correlated efficiency.

$w(i-1,S)$ and $w(i+1,S)$ and the corresponding wires in all the other sectors $w(i,S')$, $w(i-1,S')$, $w(i+1,S')$. Table 4.2 shows one example of such a sample.

Layer	Sector 1	Sector 2	Sector 3	Sector 4	Sector 5	Sector 6
i_o	670080	674517	681877	678828	676214	2207
$i_o - 1$	736412	734450	738558	746698	739865	5281
$i_o + 1$	678419	665103	685710	105299	410887	677456

Table 4.2: Example of 18 wires sample from real CLAS data. For each of the 36,000 wires a similar sample is taken.

For each wire w_j in the sample, *Buddies* is the number of wires in the same sample whose occupancy is within 8% of w_j, as illustrated in Figure 4.6. Since usu-

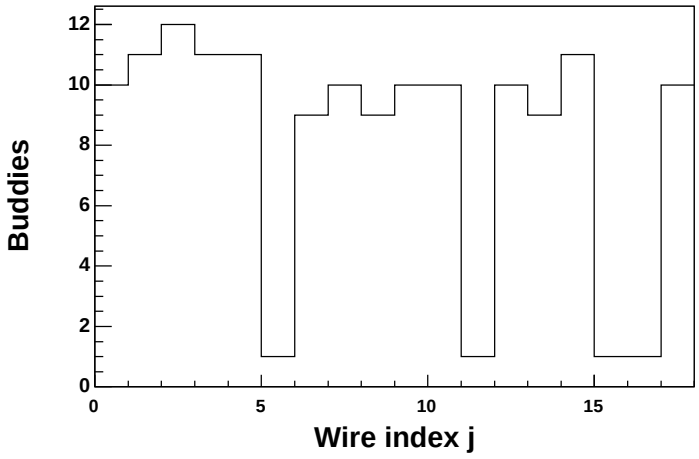

Figure 4.6: The next neighbor technique: the *buddies* histogram. Wire 3 has the maximum number of *Buddies*.

ally there are $\sim 5,000$ defective wires among the $36,000$, the probability that they maximize *buddies* is negligible. Therefore the sub-sample that maximize *buddies* is formed by good wires, whose averaged occupancy A represents a good expectation value for $w(i,S)$. In the example of table 4.2 and Figure 4.6 $A = 695191$.

The efficiency of $w(i,S)$ is in this case

$$E = Occupancy/Expectation = 670080/695191 = 0.96387$$

An efficiency table is incorporated in clas database and the GSIM MonteCarlo output is processed so that the simulated wire occupancy is a good representation of the real one [31]. Figure 4.7 shows the comparison of real and simulated efficiency for sector 5.

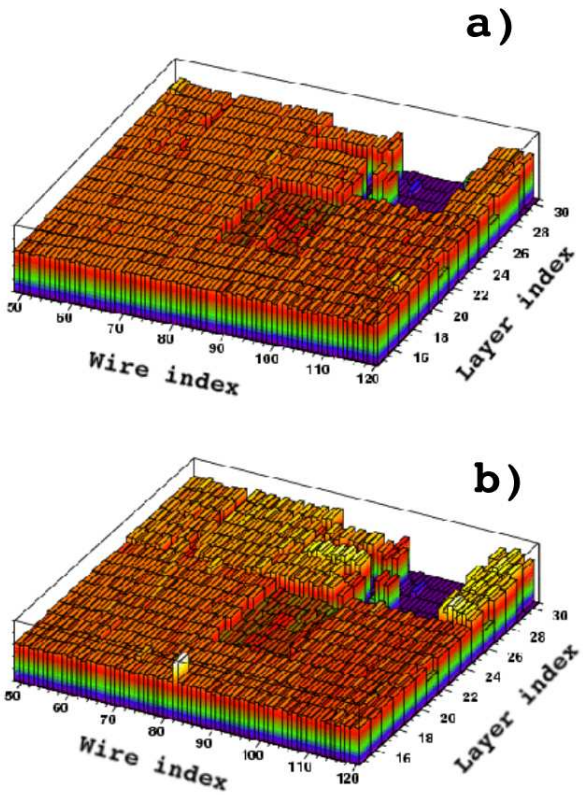

Figure 4.7: Comparison between real and simulated efficiency for sector 5. (a) simulation. (b) real data. The hole ()

4.3 Bethe Heitler events

CHAPTER 5
Analysis

5.1 Bins size

The choice of bins size in the variables W, Q^2, $\cos\theta^*$, ϕ^* is illustrated in Fig. 5.1 and Fig. 5.2. The bin sizes were chosen to uniformly agree with the parallel analysis by Park of π^+ production.

W is divided in 15 bins from 1.1 GeV to 1.4 GeV centered in $1.11, 1.13, ..., 1.39$ having $\Delta W = 0.02$. ΔQ^2 is variable and such that $\Delta Q^2/Q^2 \simeq 0.18$. The values are in table 5.1.

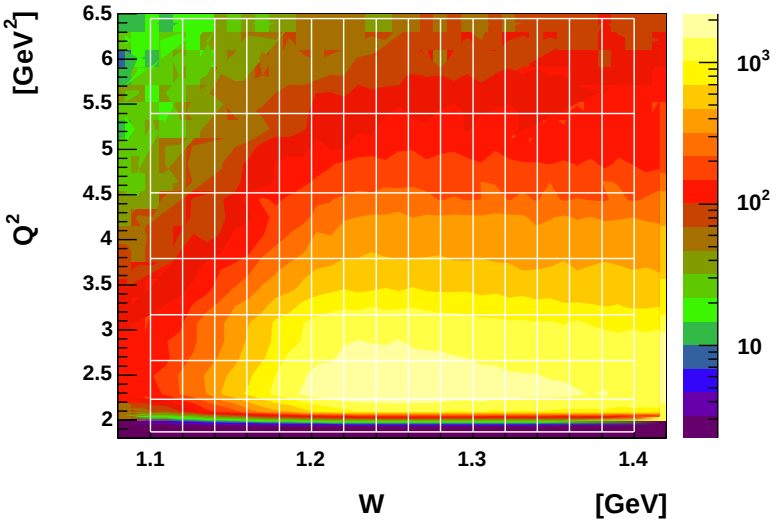

Figure 5.1: W and Q^2 binning for π^0 events. Notice the increasing ΔQ^2 size with Q^2.

Q^2	2.0	2.4	3.0	3.5	4.2	5.0	6.0
Q^2_{min}	1.87	2.23	2.66	3.17	3.79	4.52	5.40
Q^2_{max}	2.23	2.66	3.17	3.79	4.52	5.40	6.45

Table 5.1: The 6 parameter for each of the 6 sectors

$\Delta \cos\theta^* = 0.1$ and $\Delta\phi^* = 30^0$ so that there are 10 bins in $\cos\theta^*$ and 12 in ϕ^* as shown in Fig. 5.2.

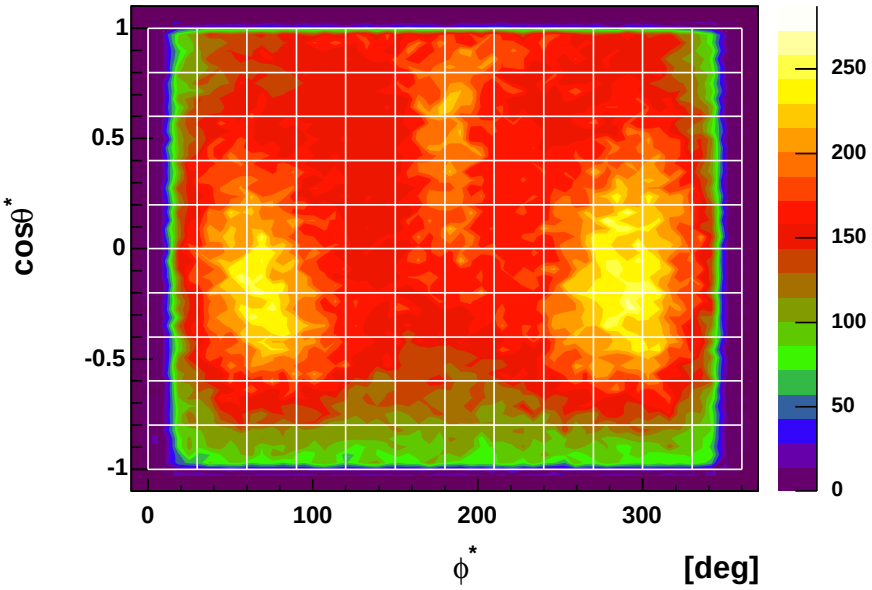

Figure 5.2: $\cos\theta^*$ and ϕ^* binning for π^0 events.

5.2 Bin averaging correction

When calculating the cross section an average in each bin occurs (see Figure 5.3. If the cross section distribution is linear in all variables inside that bin then the value at center is also the value obtained. This is not the case in the more realistic situation when the data distribution has some structure inside the bin.

To take in account this effect it is necessary to divide each bin in subdivisions, calculate the cross section in each subdivisions using a model, calculate the average A in that bin and compare A with the value at the center of the bin C. The resulting correction is

$$R = \frac{C = value\ at\ center}{A = average}$$

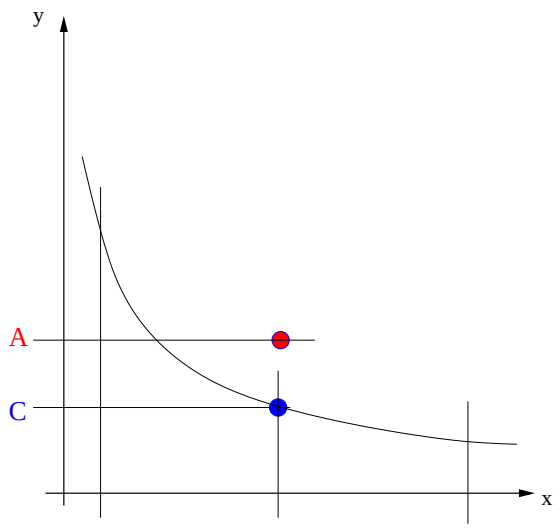

Figure 5.3: The bin correction. C is the value of the cross section at the center of the bin, while A is its average in that bin. The correction is $R = A/C$.

The model **maid 2000 extended** [11] is used to calculate the correction. Each of the $15 \times 7 \times 12 \times 10 = 12600$ bins is divided into $15^4 = 50625$ subdivisions (15 for each of the variables W, Q^2, $\cos\theta$, ϕ). This gives a total of ~ 600 million cross section points. The program used to calculate the cross section is *spp_int_e1*. The correction in each bin is

$$R_{w,\,q^2,\,\cos\theta,\,\phi} = \frac{C_{w,\,q^2,\,\cos\theta,\,\phi}}{A_{w,\,q^2,\,\cos\theta,\,\phi}}$$

Figure 5.4 illustrates the correction as a function of $\cos\theta$, ϕ for different Q^2 bins at the top of the $\Delta(1232)$ resonance.

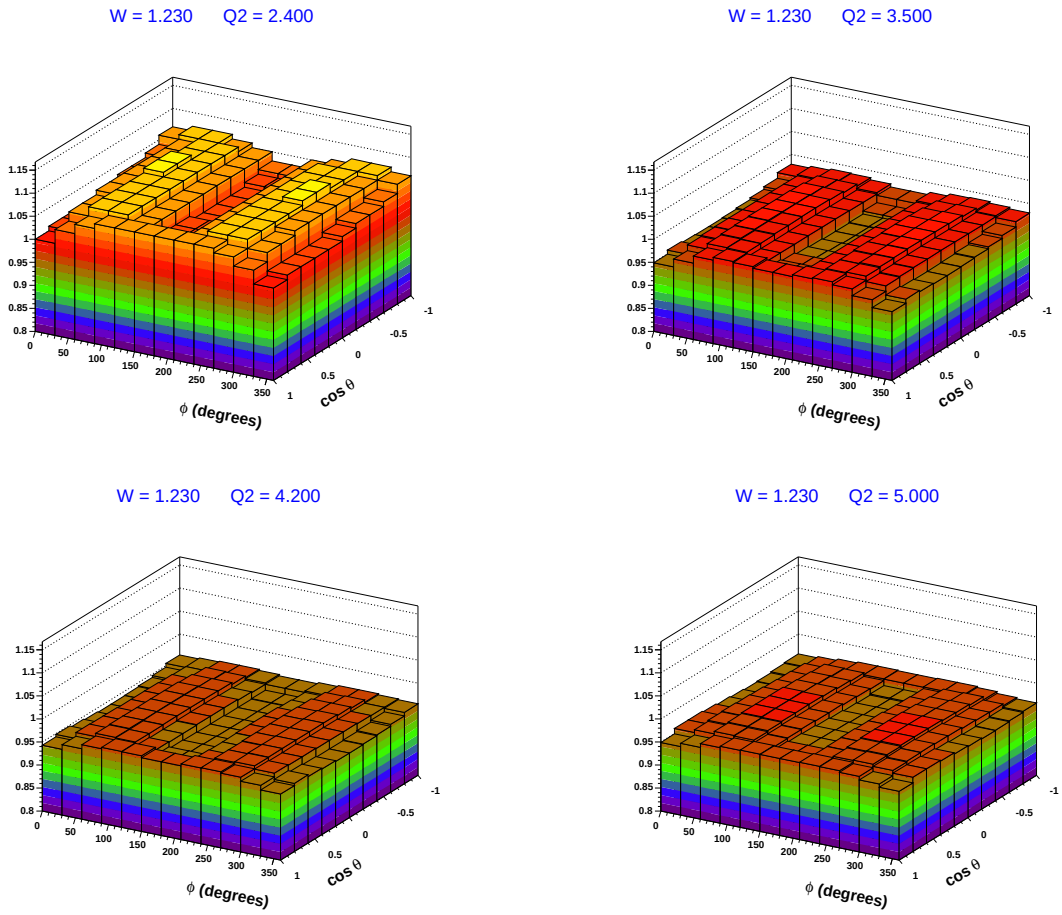

Figure 5.4: Bin averaging correction.

5.3 Radiative correction

In addition to the Born process in Figure 5.5 a) the following radiative processes contribute to the electroproduction cross section:

- the Bremsstrahlung, Figure 5.5 b) and c) where a photon is emitted by the incoming or outgoing electron.
- the vertex correction, Figure 5.5 d), where a photon is emitted by the incoming electron and absorbed by the outgoing electron.
- the vacuum polarization, Figure 5.5 e), where a e^+e^- pair is produced and annihilated by the virtual photon.

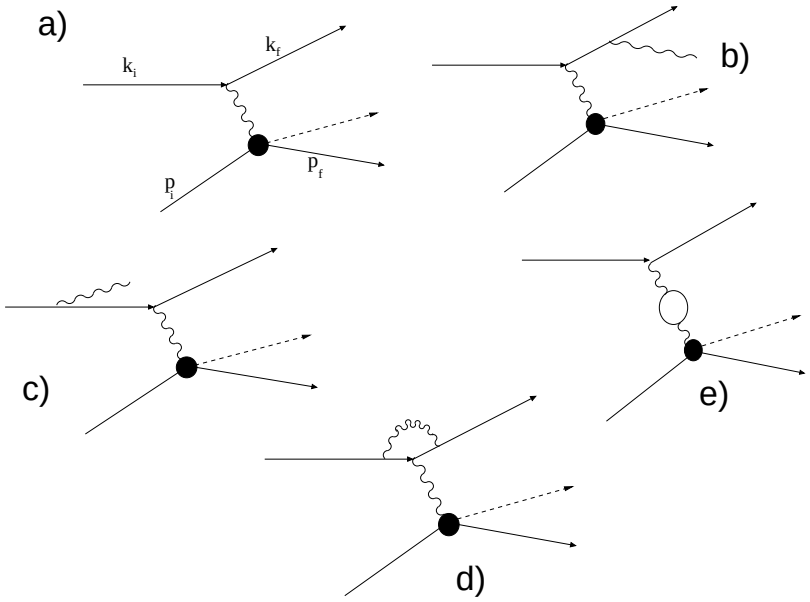

Figure 5.5: Feynman diagrams for the Born and radiative processes. a) Born electroproduction, b) and c) Bremsstrahlung d) vertex correction, e) vacuum polarization.

To account for the radiative processes the approach [2] is used which is based on a covariant method for infrared cancellation [5]. This method is preferred to the Mo and Tsai procedure [21] because:

1) It address *exclusive* electroproduction rather than inclusive, involving all four unpolarized structure functions. The Mo and Tsai formalism accounts only for two structure functions and it is independent from outgoing hadron angles.

2) The infrared cancellation is independent of the unphysical parameter Δ (energy of soft photons) necessary in the Mo and Tsai procedure.

The matrix element of the unradiative process Figure 5.5 a) can be written as

$$M^2 = \frac{e^4}{Q^4} L_{\mu\nu} W^{\mu\nu} \tag{5.1}$$

where $L_{\mu\nu}$ and $W^{\mu\nu}$ are the leptonic and hadronic tensors:

$$L_{\mu\nu} = \frac{1}{2} Tr\,(\not{k}_f + m)\gamma_\mu(\not{k}_i + m)(1 + i\gamma_5\xi)\gamma_\nu \tag{5.2}$$

$$W^{\mu\nu} = \eta^{\mu\nu} H_1 + \tilde{p}_i^\mu \tilde{p}_i^\nu H_2 + \tilde{p}_f^\mu \tilde{p}_f^\nu H_2 + (\tilde{p}_i^\mu \tilde{p}_f^\nu + \tilde{p}_f^\mu \tilde{p}_i^\nu) H_4 + (\tilde{p}_i^\mu \tilde{p}_f^\nu - \tilde{p}_f^\mu \tilde{p}_i^\nu) H_5 \tag{5.3}$$

In (5.2) and (5.3) ξ is the electron polarization vector, the index i (f) refers to incoming (outgoing) particles and the transformation $\tilde{a}^\mu \rightarrow a^\mu - \frac{aq}{q^2} q^\mu$ ensures electromagnetic gauge invariance. The contraction (5.1) can be written as

$$L_{\mu\nu} W^{\mu\nu} = 2 \sum_{i=0}^{5} \theta_i H_i \tag{5.4}$$

where the θ_i are linears combination of the usual Lorents invariants defined from the electrons 4-momenta and the H_i are linear combinations of the unpolarized (σ_T, σ_L, σ_{LT}, σ_{TT}) and polarized ($\sigma_{LT'}$) structure functions.

The leptonic tensor for the radiative processes illustrated in Figure 5.5 b), c), d) and e) is

$$L^R_{\mu\nu} = \frac{1}{2} Tr\,(k_f + m)\Gamma_{\mu\alpha}(k_i + m)(1 + i\gamma_5\xi)\hat{\Gamma}_{\alpha\nu} \tag{5.5}$$

where the tensor $\Gamma_{\mu\alpha}$ contains the photon information k_γ^μ and $\hat{\Gamma}(k) = \Gamma(\not{k})$.

The contraction of $L_{\mu\nu}^R$ with $W^{\mu\nu}$ gives the matrix element for the radiative processes:

$$M_R^2 = -\frac{2e^6}{\tilde{Q}^4} L_{\mu\nu}^R W^{\mu\nu} = -\frac{2e^6}{\tilde{Q}^4 R_w} \sum_{i=0}^{5} \theta_i H_i \tag{5.6}$$

where $\tilde{Q^2} = -(q - k_\gamma)^2$ and $R_w = W^2 - (p + q - k_\gamma)^2$. One can see the involvement of all the structure functions.

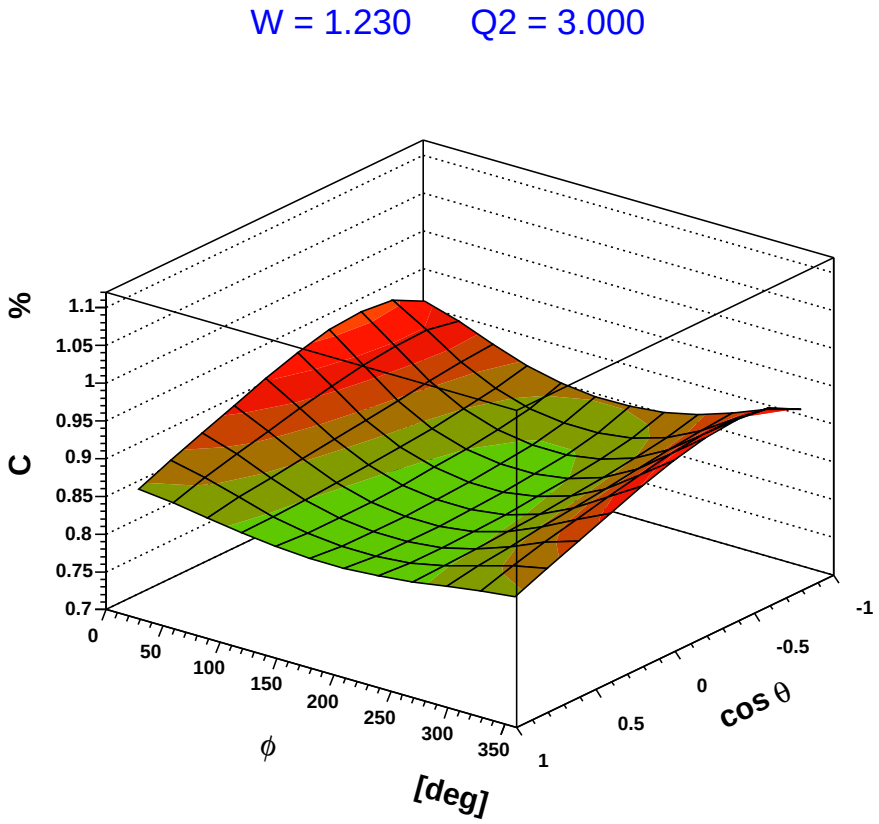

Figure 5.6: Radiative correction as a function of $\cos\theta^*$ and ϕ^* for $W = 1.23$ GeV and $Q^2 = 3$ GeV^2.

A program named *exclurad* has been developed to calculate the matrix element (5.6) using existing models (lime MAID or DMT) for the structure functions. This program gives the radiative correction C as the ratio of the radiative and unradiative four fold cross section:

$$C(W, Q^2, \cos\theta^*, \phi^*) = \frac{\sigma_{RAD}}{\sigma_{UNRAD}}$$

and its output has been used as the radiative correction in this analysis. Figure 5.6 shows the correction as a function of $\cos\theta^*$ and ϕ^* for $W = 1.23$ GeV and $Q^2 = 3$ GeV^2.

5.4 Absolute normalization of the cross section

During the data acquisition the electric charge impinging on the target was saved in the data stream as accumulated charge corrected for live-time by a Faraday cup reading located in the beam dump. This is a particular event in the data stream called *scaler* event. It consist of a counter which output F_{CUP} is proportional to the accumulated charge by the relation:

$$Q(Coulomb) = \frac{F_{CUP}}{9264.0 \cdot 10^9}$$

Since one run was typically divided in several files, it is possible that the last Faraday cup reading does not correspond to the accumulated charge for the run because of corrupted i/o (for example one file can be lost). This is a rare eventuality but must be taken into account.

To calculate the Faraday cup for a run the difference between one scaler reading and the next is calculated and saved

$$\Delta F_{CUP} = F^{i'}_{CUP} - F^{i}_{CUP}$$

only when $i' = i+1$ (otherwise $\Delta F_{CUP} = 0$). The ΔF_{CUP} obtained is then summed over all scaler events.

For the e1-6 running period the total Faraday cup reading was $F_{CUP} = 2.06816e+11$ for a total charge

$$Q = 0.022325 \text{ Coulomb}$$

Assuming a constant current $c = 7\,nA$ this gives a running time $t = Q/c \sim 3.2 M\text{sec} \sim 37$ days. The number of accelerated electrons was

$$n_e = Q/e = 1.3934 \cdot 10^{17}$$

where e is the electron charge. The number of target nuclei per cm^2 can be calculated with the formula:

$$n_P = \frac{L\,\rho\,N_A}{a.m.u.}$$

where $L = 5$ cm is the length of the target, $\rho = 0.0708$ g/cm^3 is the density of H_2 at 20K, $A = 6.022 \cdot 10^{23}$ mol^{-1} is the Avogadro number and $a.m.u. = 1.00794$ g/mol is the atomic mass unit of the hydrogen. This gives

$$n_P = 2.115 \cdot 10^{23}\text{cm}^{-2}$$

So the integrated luminosity for the e1-6 period was

$$L_{int} = 2.95 \cdot 10^{40}\text{cm}^{-2}$$

5.5 Extraction of the structure functions

As explained in Section 1.1 the π^0 differential cross section in the resonance center of mass assume the form

$$\frac{d\sigma}{d\Omega^*_{\pi^0}} = \frac{2Wp^*_{\pi^0}}{W^2 - m_P^2}\left(\sigma_T + \epsilon\sigma_L + \epsilon\sigma_{TT}sin^2\theta cos2\phi + \sigma_{LT}\sqrt{2\epsilon_L(\epsilon+1)}sin\theta cos\phi\right)$$

where ϕ and θ are the azimuthal and polar angle of the π^0 in the c.m. frame. π^0. The ϕ distributions are modulated only by the terms $\cos\phi$ and $\cos 2\phi$ while all the other terms vary with W, Q^2 and $\cos\theta$ (but not with ϕ). Therefore the structure functions can be extracted with a ϕ fit.

For each W, Q^2 and $\cos\theta$ bin the quantity in parenthesis is fitted with the functional form

$$y = a + b\cos\phi + c\cos 2\phi$$

The structure functions are then calculated with the formulas:

$$\begin{aligned}
\sigma_T + \epsilon\sigma_L &= a \\
\sigma_{LT} &= \frac{b}{\sin\theta\sqrt{2\epsilon(\epsilon_T+1)}} \\
\sigma_{LT} &= \frac{c}{\sin^2\theta\epsilon_T}
\end{aligned}$$

Figure 5.7 show the ϕ fits for $W = 1.1 \pm 0.01$ GeV and $Q^2 = 2.4$ GeV^2.

Figure 5.8 shows the χ^2/ν distribution for all the fits at different Q^2 values (black points) along with the expected χ^2/ν distribution (red line). There are 12 bins in ϕ and there are 3 fit paramters therefore

$$\nu = N - \text{constrains} = 9.$$

Figure 5.9 shows $\sigma_L + \epsilon\sigma_T$ resulting from the fit at $Q^2 = 2.4$ GeV^2.

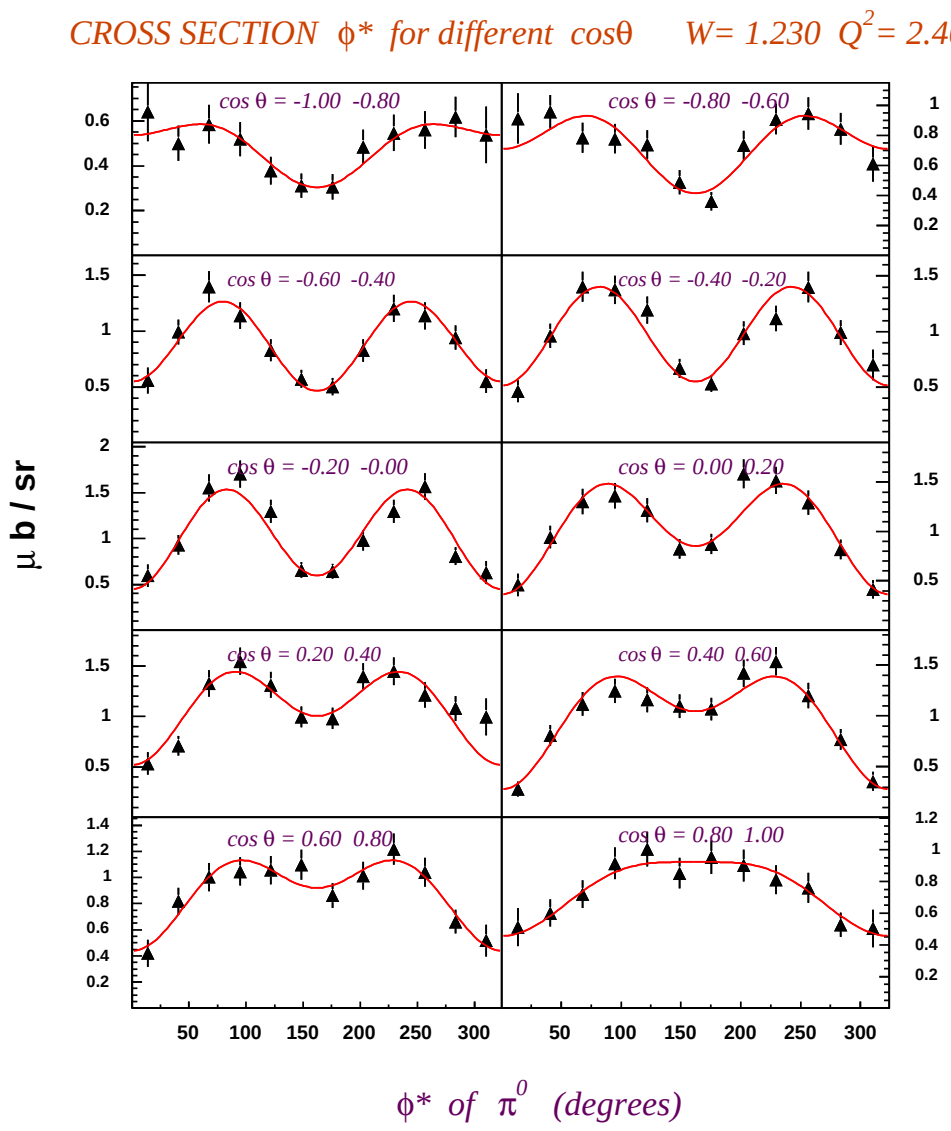

Figure 5.7: ϕ **fits of the cross section for different** $\cos\theta$ **values. The function used for the fit is** $y = a + b\cos\phi + c\cos 2\phi$ **and the structure functions follow from the paramters** a, b, c**.**

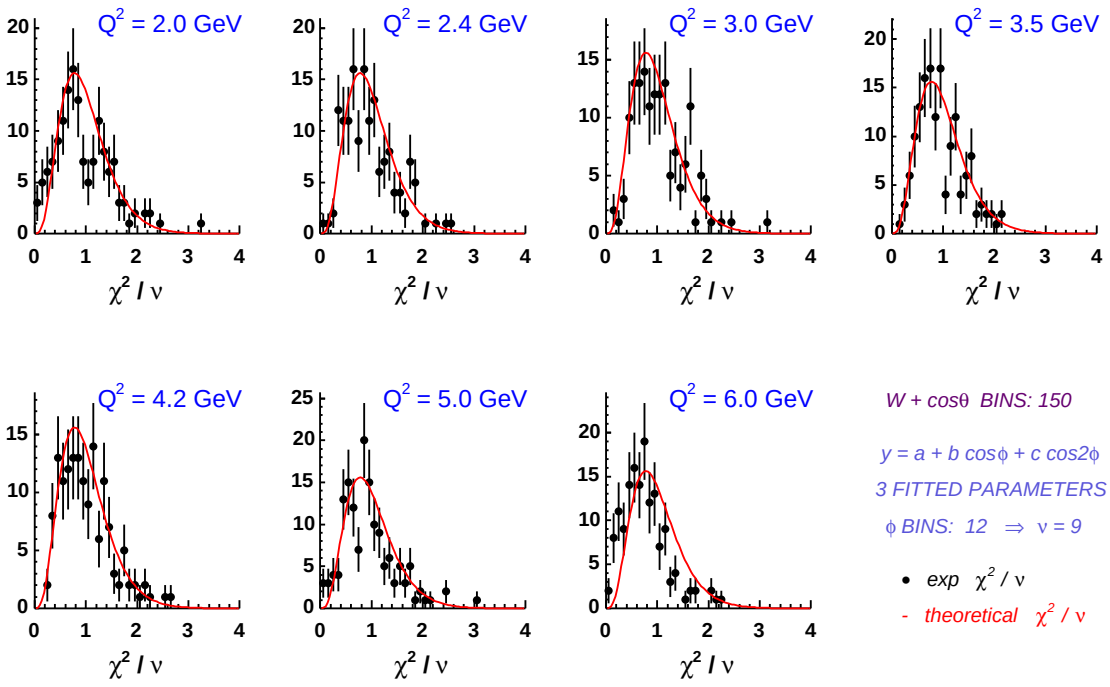

Figure 5.8: Reduced χ^2 distribution of the ϕ fits. The distributions show consistency with the expected χ^2 distribution for 150 fits (15 W bins and 10 $\cos\theta$ bins) and 9 degrees of freedom.

5.6 Legendre expansion

In order to extract the multipoles, the structure functions were fitted with orthogonal Legendre polynomials with ℓ up to d-waves:

$$\begin{aligned}
\sigma_T + \epsilon\sigma_L &= A_0 + A_1 P_0(cos\theta) + A_2 P_2(cos\theta) + A_2 P_3(cos\theta) + A_3 P_4(cos\theta) \\
\sigma_{TT} &= C_0 + C_1 P_0(cos\theta) \\
\sigma_{LT} &= D_0 + D_1 P_0(cos\theta) + D_2 P_2(cos\theta)
\end{aligned}$$

Figures 5.9, 5.10 and 5.11 show the fits for $\sigma_L + \epsilon\sigma_T$, σ_{TT} and σ_{LT} for different W at $Q^2 = 2.4$ GeV^2. Figure 5.12 shows the obtained and the expected χ^2/ν distributions for the various response functions.

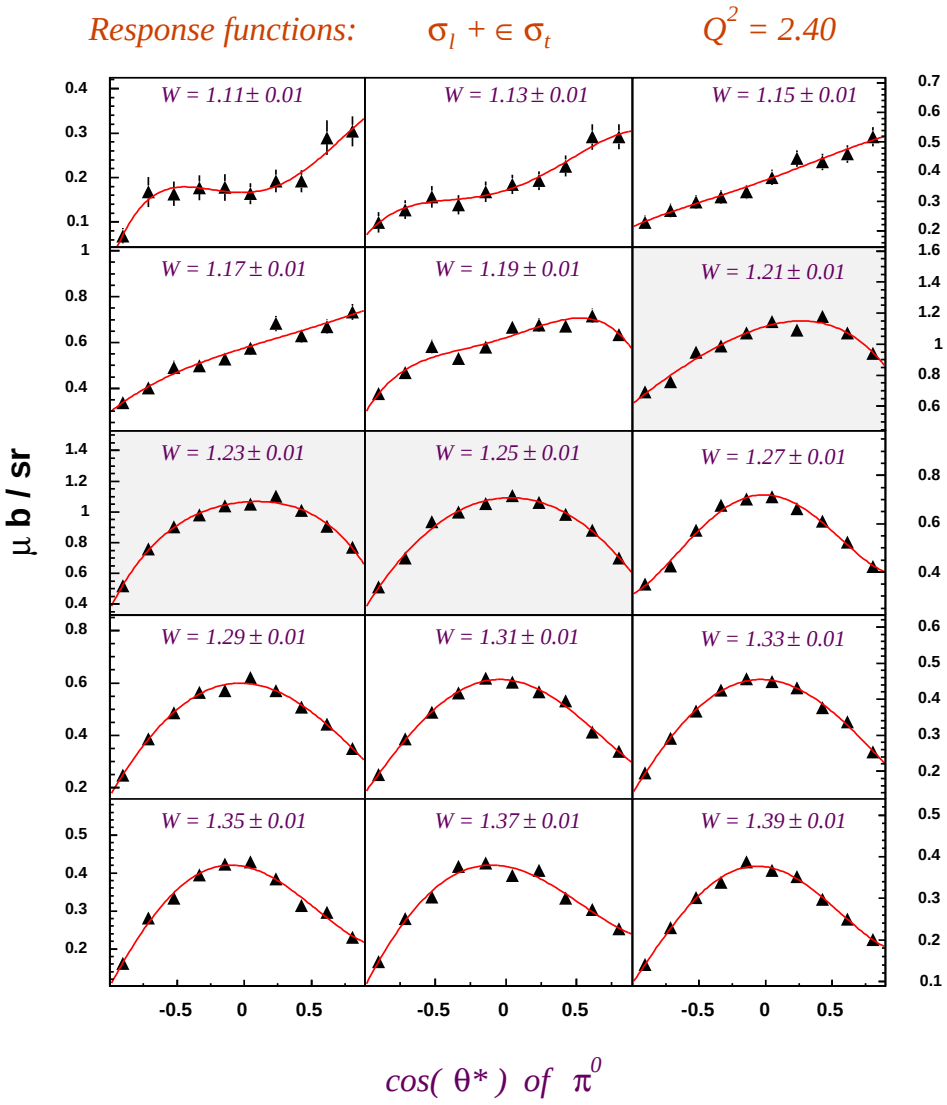

Figure 5.9: $\sigma_L + \epsilon\sigma_T$ **for different** W **at** $Q^2 = 2.4$ **GeV**^{2}**. The shaded histograms refer to ones used to extract** R_{EM} **and** R_{SM}**. The legendre expansion (red line fit) is:** $\sigma_T + \epsilon\sigma_L = A_0 + A_1 P_0(cos\theta) + A_2 P_2(cos\theta) + A_2 P_3(cos\theta) + A_3 P_4(cos\theta)$**.**
The shaded histograms refer to the Δ **region.**

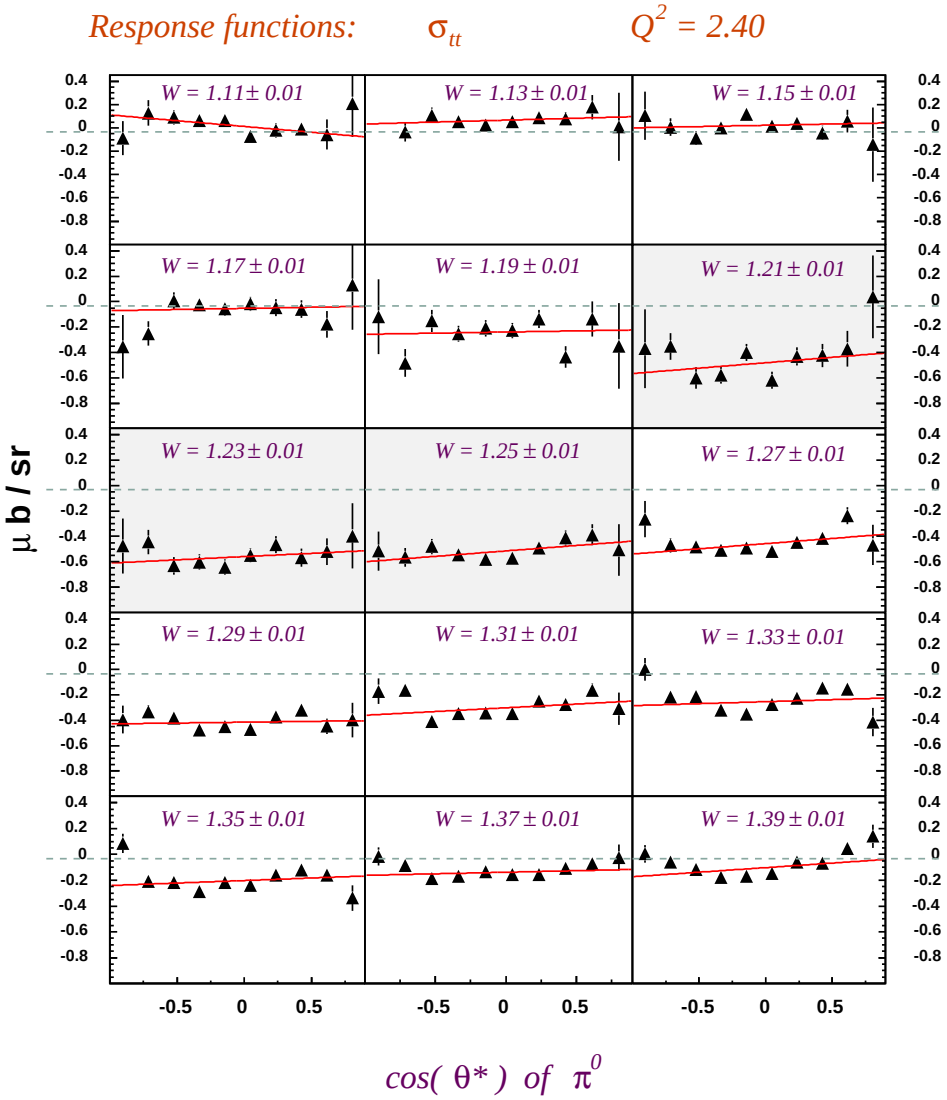

Figure 5.10: σ_{TT} **for different** W **at** $Q^2 = 2.4$ **GeV². The legendre expansion (red line fit) is:** $\sigma_{TT} = C_0 + C_1 P_0(cos\theta)$.
The shaded histograms refer to the Δ region.

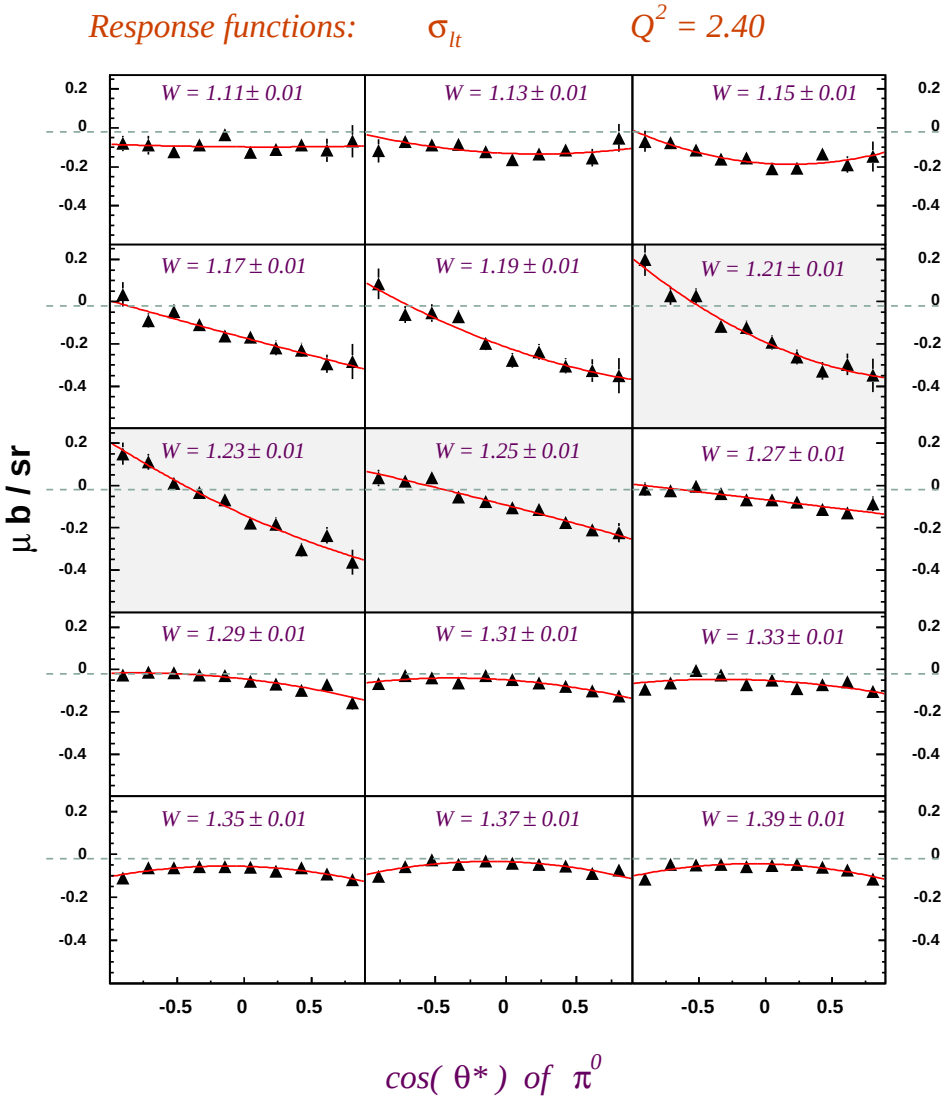

Figure 5.11: σ_{LT} for different W at $Q^2 = 2.4$ GeV^2. The legendre expansion (red line fit) is: $\sigma_{LT} = D_0 + D_1 P_0(cos\theta) + D_2 P_2(cos\theta)$. The shaded histograms refer to the Δ region.

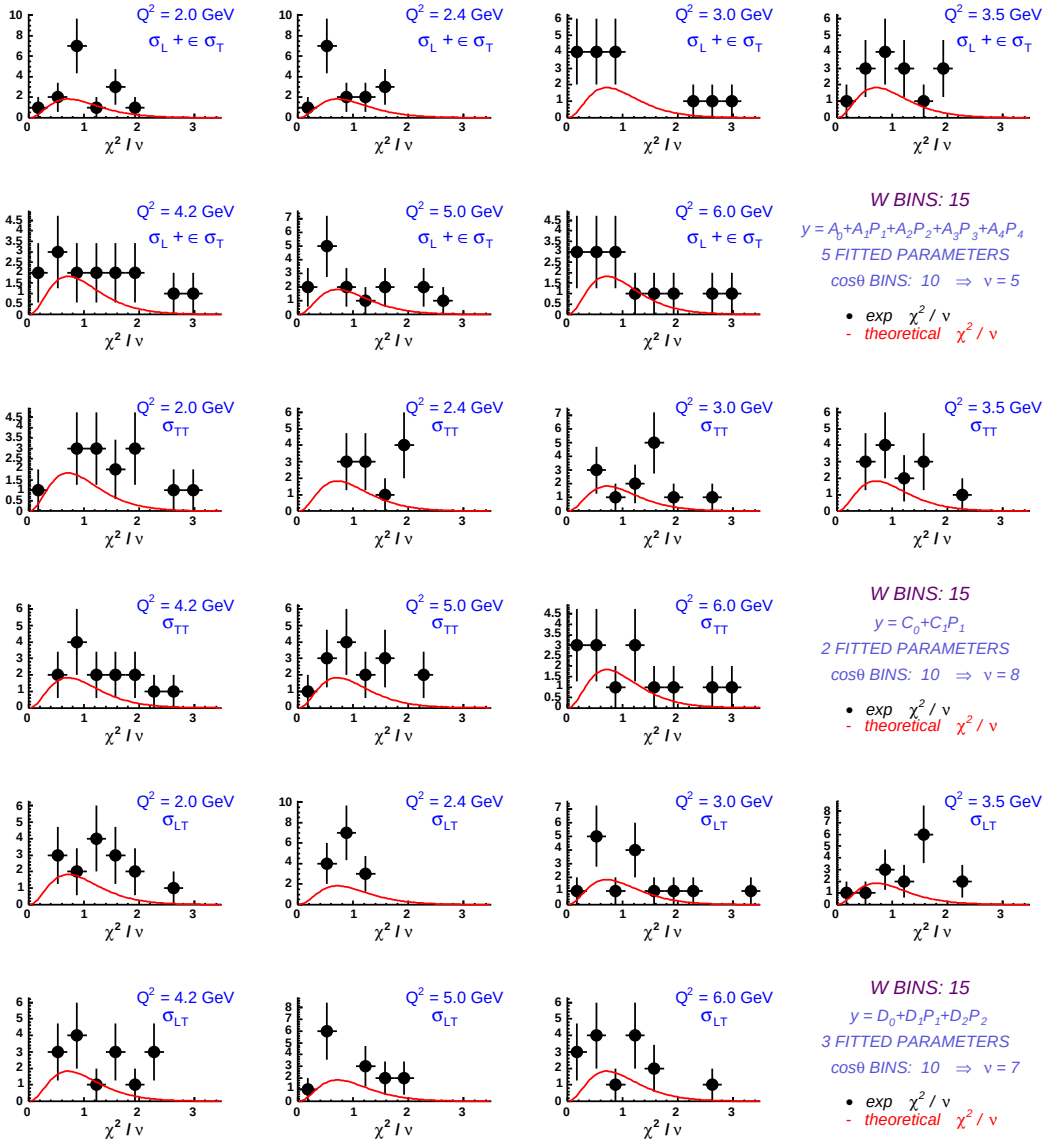

Figure 5.12: Reduced χ^2 distribution of the Legendre fits. The $\sigma_L + \epsilon\sigma_T$, σ_{TT} and σ_{LT} have respectively 5, 8, and 7 degrees of freedom. Each plot has only 15 points (there are 15 W bins) so the statistic of the χ^2/ν distributions is poor. The red line is the expected χ^2 distribution.

Figure 5.13 shows the coefficients of the Legendre expansion for $Q^2 = 2.4$ GeV^2. The coefficient A_0, proportional to M_{1+} and to the total c.m. cross section, shows the characteristic resonance behaviour at the peak of the Δ.

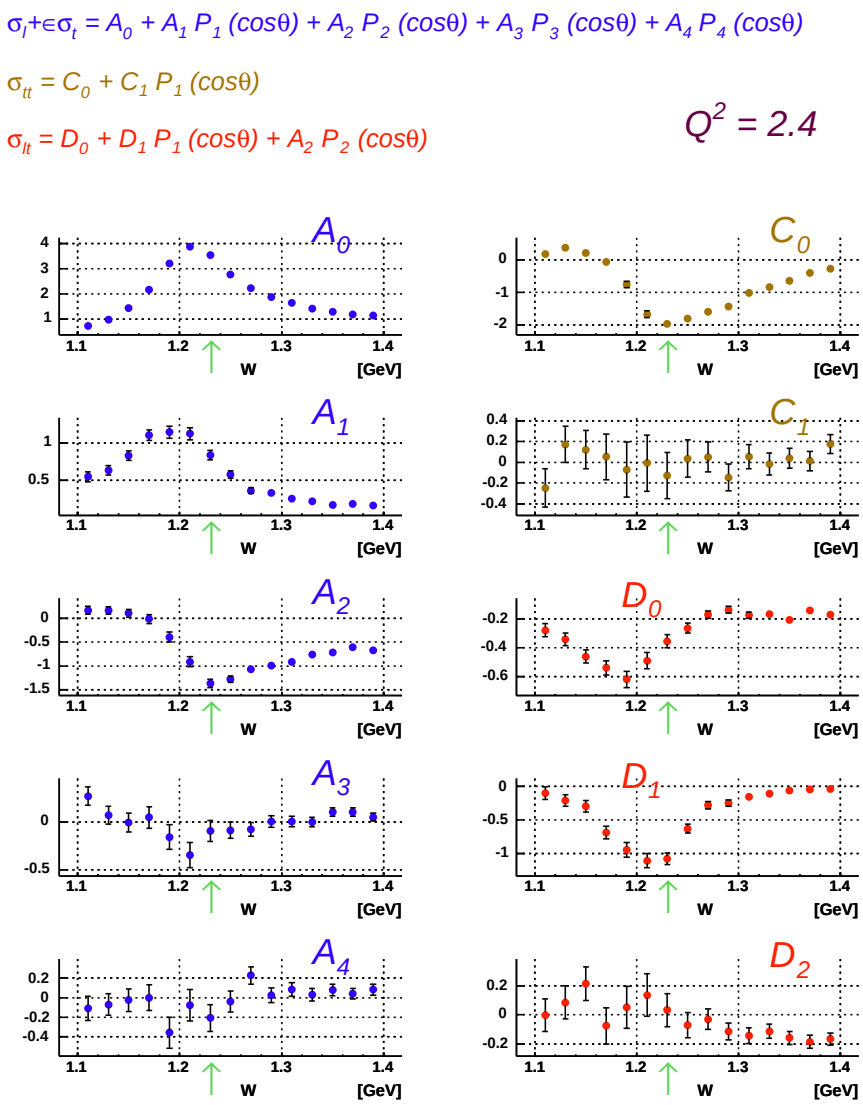

Figure 5.13: Legendre coefficients at $Q^2 = 2.4$ GeV^2. The green arrow shows the Δ mass position. The coefficient A_0 is proportional to M_{1+} and to the total c.m. cross section.

5.7 M_{1+} dominance.

The approximation made above of ℓ up to d-waves is a good approximation: one can see from Figure 5.13 that A_4, C_1, D_2 are rather small around the Δ compared to their respectives coefficients with smaller ℓ. In order to make a model independent extraction of the multipoles a further approximation is needed.

A large known signal A can be used to enhance and measure a small signal B by considering the product AB. Previous measurements (at Q^2 up to 4 GeV^2) confirmed that E_{1+} and S_{1+} are small compared to M_{1+}. Furthermore all models that apply in this range of Q^2 show that M_{1+} is the multipole that has the greatest strength.

The M_{1+} dominance approximation consists in considering only the multipoles that interfere with M_{1+}. With this approximation the relation between the Legendre coefficients and the electromagnetic multipoles is [25]:

$$\begin{aligned} |M_{1+}|^2 &= A_0/2 \\ Re(E_{1+}M_{1+}^*) &= (A_2 - 2B_0/3)/8 \\ Re(S_{1+}M_{1+}^*) &= D_1/6 \\ Re(E_{0+}M_{1+}^*) &= A_1/2 \\ Re(S_{0+}M_{1+}^*) &= D_0 \\ Re(M_{1-}M_{1+}^*) &= -(A_2 + 2(A_0 + C_0))/8 \end{aligned} \tag{5.7}$$

The multipoles are considered at $W = 1.21, 1.23, 1.25$ and the average of these values is used as the final result.

5.8 Effect of M_{1+} dominance and $\ell \leq 2$ approximation

The M_{1+} dominance assumption and the limited order ($\ell \leq 2$) in the Legendre expansion of the structure functions introduce an uncertainty in the extraction of the multipoles. In order to evaluate such uncertainty two models (MAID, DMT) were used to generate the cross sections σ_{MAID} and σ_{DMT}. These models provide the multipoles $E_{\ell\pm}$, $S_{\ell\pm}$, $M_{\ell\pm}$ with ℓ up tp 5.

The generated cross section were fitted as described in Section 5.5 to extract

the structure functions. The structure functions were fitted with orthogonal Legendre polynomials with ℓ up to d-waves as in Section 5.6. The approximation (5.7) was used in order to extract the multipoles.

Figure 5.14 and Figure 5.15 show the model and extracted multipole ratios for $Q^2 = 3.5$ GeV^2. See Appendix D for the plots at different value of Q^2.

One can see that DMT prescribes in the Δ region a smaller value of S_{1+} then MAID. E_{1+} remains negative and constant for MAID while it becomes positive in DMT between Q^2 of 3 and 4 GeV^2.

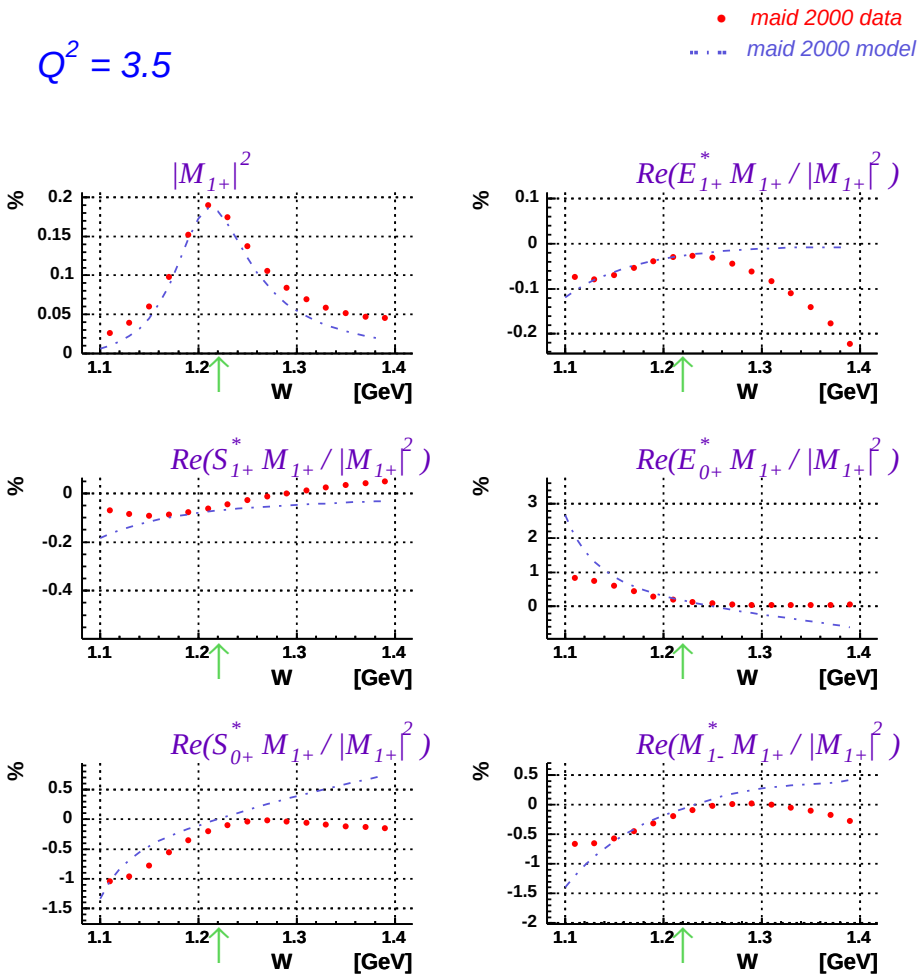

Figure 5.14: Comparison between the model and extracted multipole ratios for MAID 2000 at $Q^2 = 3.5$ GeV^2.

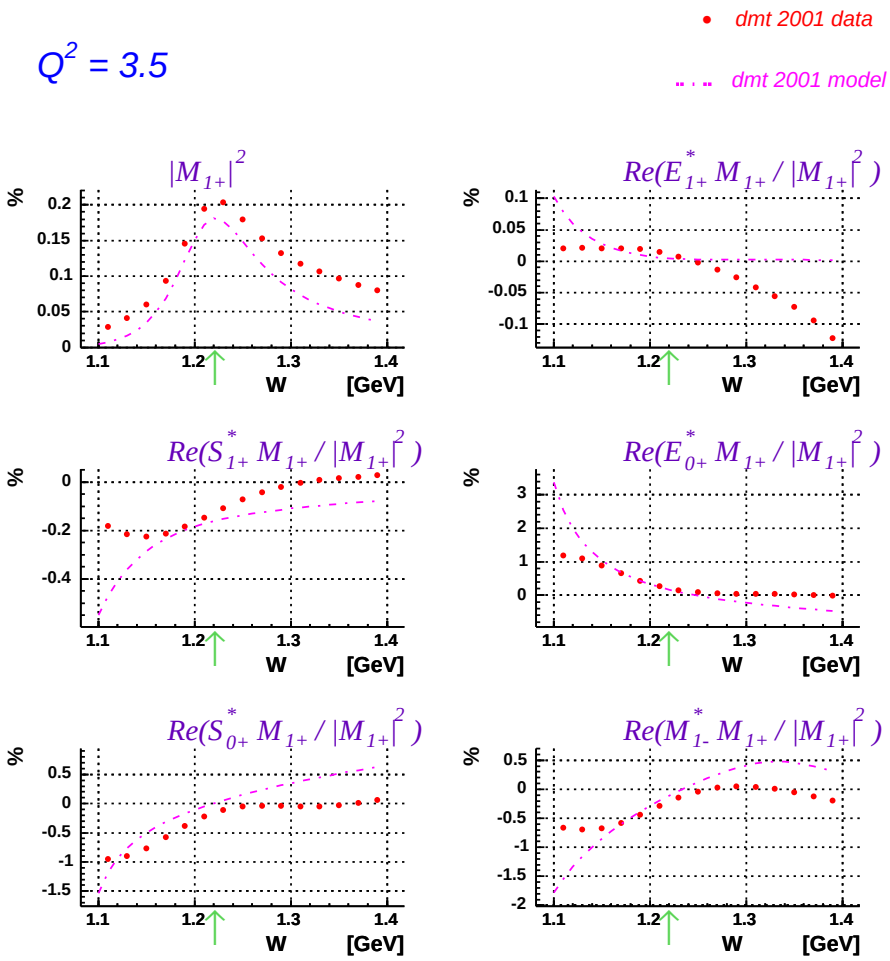

Figure 5.15: Comparison between the model and extracted multipole ratios for DMT 2001 at $Q^2 = 3.5$ GeV^2.

The extracted multipoles were averaged over the $W = 1.21, 1.23, 1.25$ bins and the difference with the model prediction at the Δ peak is illustrated in Figure 5.16 for E_{1+}/M_{1+} and in Figure 5.17 for S_{1+}/M_{1+}.

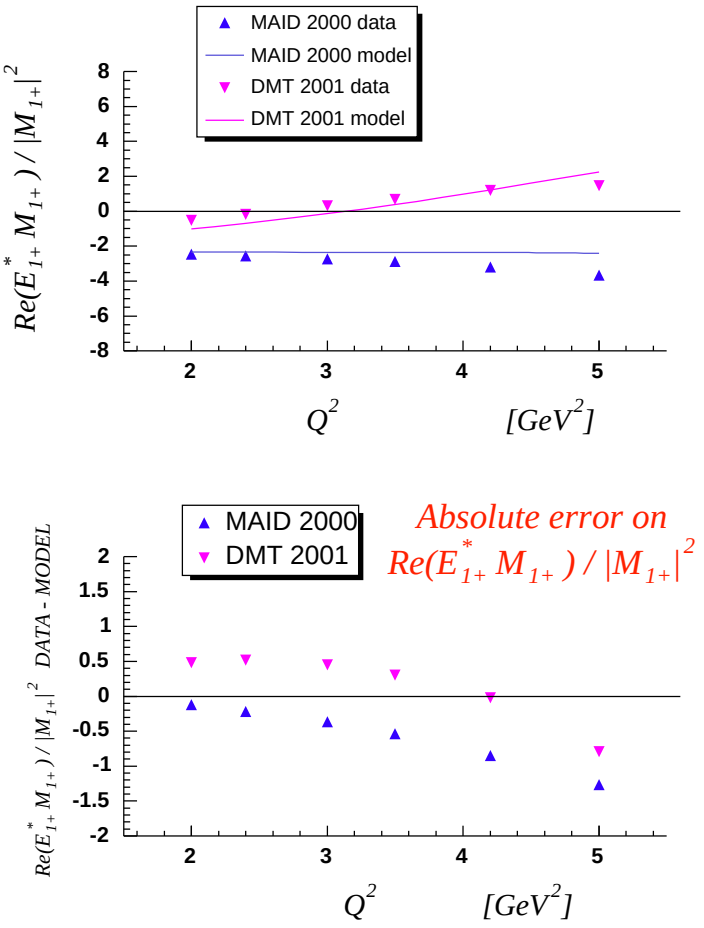

Figure 5.16: Model and extracted E_{1+}/M_{1+} as a function of Q^2. Top: the points are the value from the fit and the approximations described in the text. The lines are the model prediction. Bottom: absolute difference between between extracted value and model prediction.

When MAID is used the ratio E_{1+}/M_{1+} is always underestimated, starting at $\sim 0.2\%$ at $Q^2 = 2$ GeV^2 and up to $\sim 1.2\%$ at $Q^2 = 5$ GeV^2. When DMT is used

a rather constant overestimation by $\sim 0.5\%$ of E_{1+}/M_{1+} up to $Q^2 = 3.5$ GeV^2 is obtained. At $Q^2 = 4.2$ the value extracted is the same as in the model but at $Q^2 = 5$ E_{1+}/M_{1+} seems underestimated by $\sim 0.8\%$.

As regarding S_{1+}/M_{1+}, the extraction from both models yelds a rather significant overestimation increasing in value with Q^2.

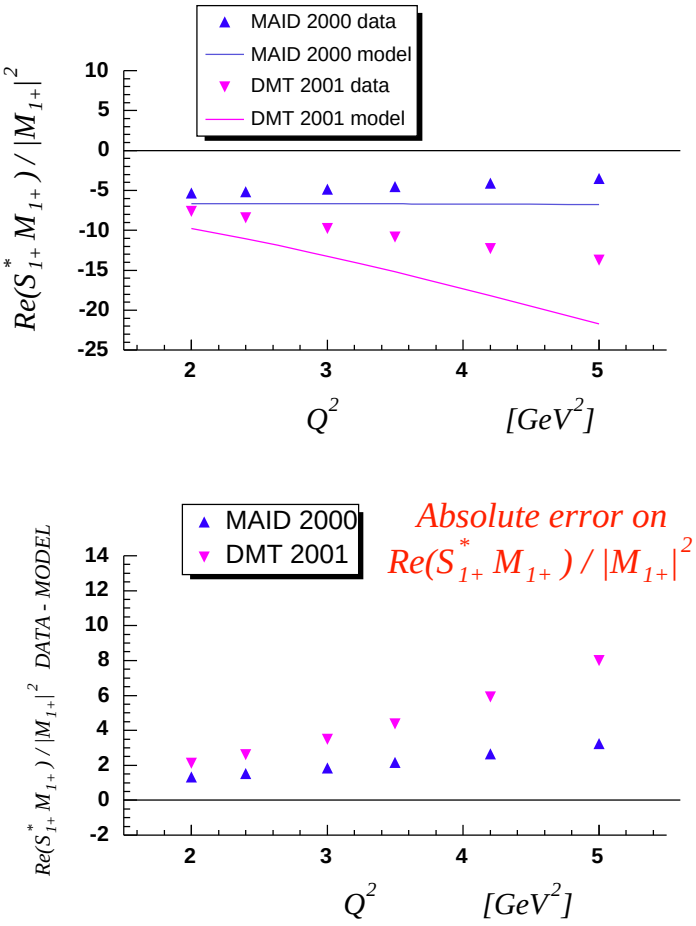

Figure 5.17: Model and extracted S_{1+}/M_{1+} as a function of Q^2. Top: the points are the value from the fit and the approximations described in the text. The lines are the model prediction. Bottom: absolute difference between between extracted value and model prediction.

We can conclude that the extraction of ratio E_{1+}/M_{1+} is not affected signif-

icantly except at $Q^2 = 5$ GeV^2 where it could be underestimated by $\sim 1\%$. On the other hand the ratio S_{1+}/M_{1+} is always overestimated by a significant value increasing with Q^2.

5.9 for R_{EM} and R_{SM}

The result for the ratios R_{EM} and R_{SM} are shown in Table 5.2

Q^2 (GeV^2)	R_{EM} (%)	R_{SM} (%)
2.0	-1.2 ± 0.8	-8.4 ± 0.8
2.4	-0.4 ± 0.4	-8.7 ± 0.5
3.0	0.8 ± 0.5	-8.1 ± 0.5
3.5	0.7 ± 0.6	-6.6 ± 0.7
4.2	1.5 ± 0.8	-8.8 ± 1.1
5.0	5.2 ± 1.3	-12.3 ± 1.8
6.0	4.0 ± 2.5	-10.3 ± 4.1

Table 5.2: The 6 parameter for each of the 6 sectors

R_{EM} is shown in Figure 5.18 along with the prediction from DMT 2001 and MAID 2000 models. Previous data from CLAS and Hall C are also plotted.

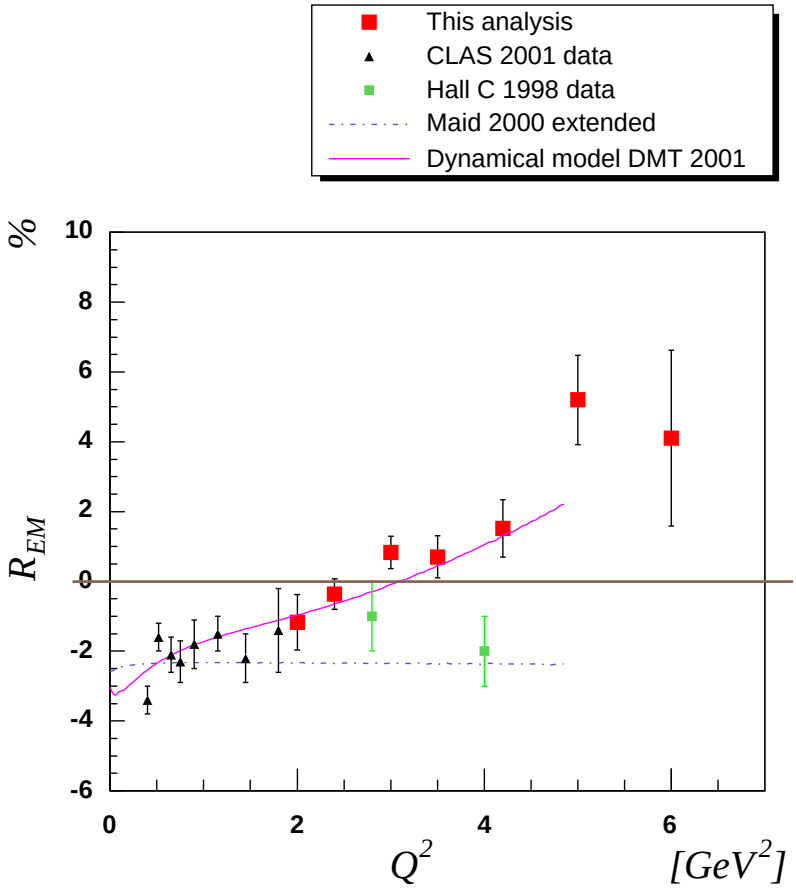

Figure 5.18: Result for R_{EM} as a function of Q^2.

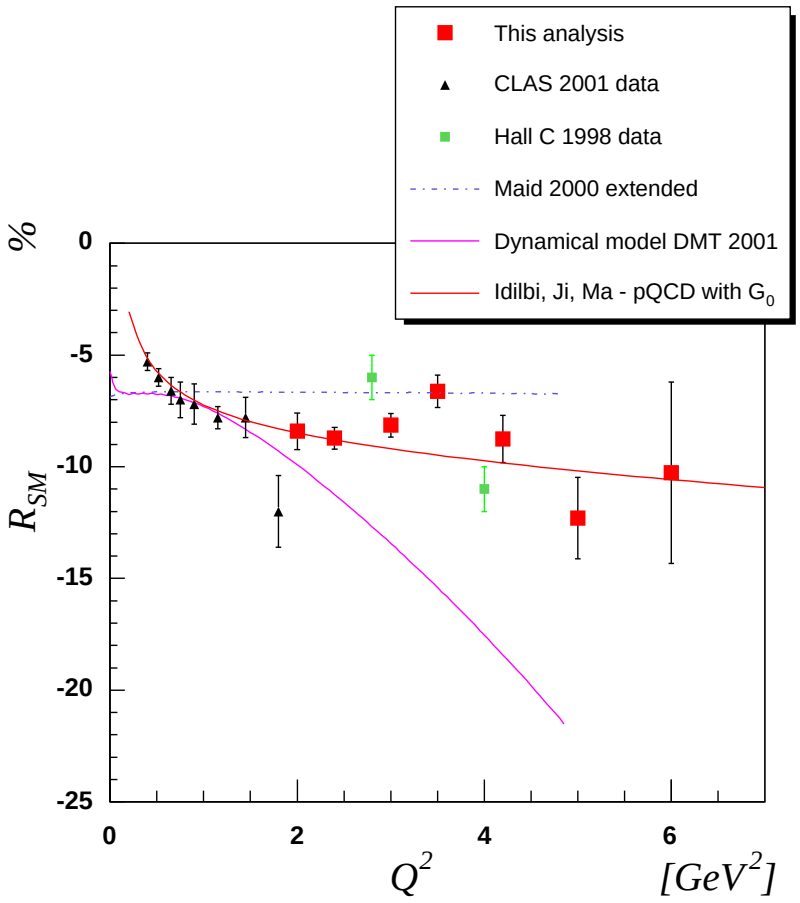

Figure 5.19: Result for R_{SM} as a function of Q^2.

5.10 Result for G_M^*

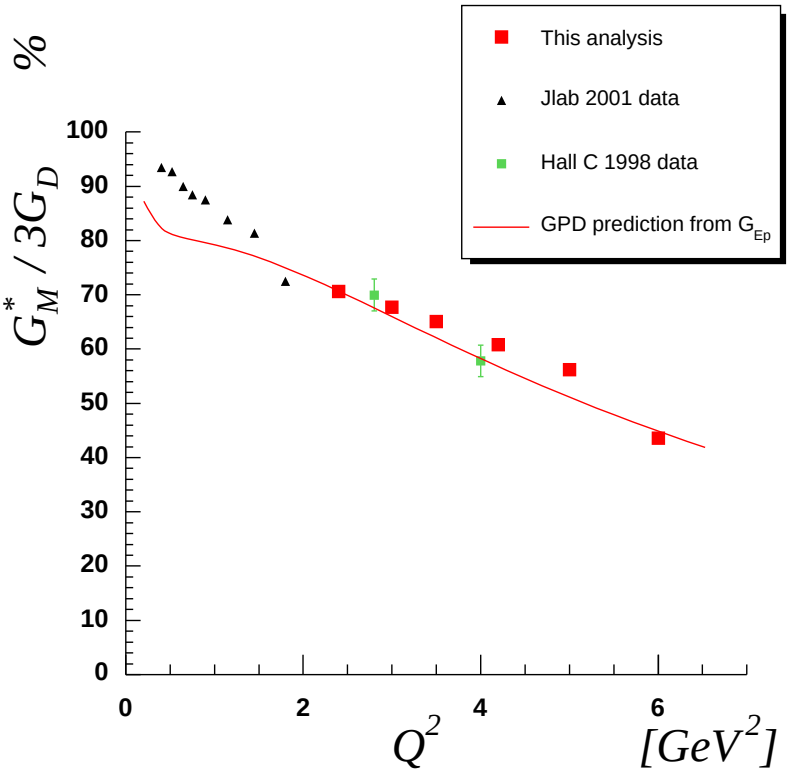

Figure 5.20: Result for R_{SM} as a function of Q^2.

LITERATURE CITED

[1] G. Adams et al., *Nucl. Instrum. Meth.* **A465** *414-427 (2001)*

[2] A. Afanasev, I. Akushevich, V. Burkert, K. Joo, *PiN Newslett.* **16***, 343 (2002)*

[3] M. Amarian et al., *NIM A* **460** *(2001) 239*

[4] M. Anselmino, *Rev. Mod. Phys.* **65***, (1993) 1199*

[5] D.Y. Bardin, N.M. Shumeiko, *Nucl. Phys. B* **127***, 242 (1977)*

[6] G.F. Chew et al., *Phys. Rev.* **106** *(1957) 1345-1337*

[7] F. Close, Z. Li, *Phys. Rev.* **D42***, (1990) 2194*

[8] L.A. Copley, G. Karl, E. Obruk, *Phys. Lett.* **B29***, (1969) 117*

[9] R.M. Davidson, N.C. Mukhopadhay, R. Wittman, *Phys. Rev. Lett* **56***, (1986) 804*

[10] R.M. Davidson, N.C. Mukhopadhay, R. Wittman, *Phys. Rev.* **D43***, (1991) 871*

[11] D. Drechsel, O. Hanstein, S.S. Kamalov, L. Tiator, *Nucl. Phys.* **A645** *(1999) 145-174*

[12] K.S. Egiyan, *CLAS NOTE 99 - 007*

[13] R. Feuerbach, *PhD thesis*

[14] R.P. Feynman, *Phys. Rev.* **D3***, (1971) 2706*

[15] O. Hanstein, *Nucl.Phys.* **A632** *(1998) 561*

[16] N. Isgur, G. Karl, *Phys. Rev.* **D18***, (1978) 4187*

[17] S.S. Kamalov, S.N. Yang, D. Drechsel, L. Tiator, *Phys. Rev. Lett.* **83** *(1999) 4494*

[18] Valeri Koubarovski, *private communication.*

[19] Valeri Koubarovski, *private communication.*

[20] C. W. Leeman, D. R. Douglas, G. A. Krafft, *Ann. Rev. Nuc. Part. Sci., 51:413-450 (2001)*

[21] Mo and Tsai, *Rev. Mod. Phys.* **41** *(1969)*

[22] B. Niczyporuk, *CLAS NOTE 91 - 001*

[23] R. Niyazov and L.B. Weinstein, *CLAS NOTE 01 - 013*

[24] Kijun Park, *private communication.*

[25] A.S. Raskin, T.W. Donnelly, *Ann. Phys.,* **C63***, 78 (1989)*

[26] T. Sato, T.S. Lee, *nucl-th/0010025*

[27] T. Sato, T.S Lee, *Phys. Rev.* **C54***, (1996) 2660*

[28] T. Sato, T.S Lee, *Phys. Rev.* **C63***, (2001)*

[29] A. Silva, D. Urbano, T. Watabe, M. Fiolhais, K. Goeke, *hep-ph/9905326*

[30] Elton Smith et al., *NIM A* **432** *(1999) 265*

[31] M. Ungaro, Ji Li, *CLAS NOTE 03 - 006*

[32] R.L. Walker, *Phys. Rev.* **182** *(1969) 1729-1748*

[33] M. Warns, H. Schroder, W. Pfeil, H. Rollnik, *Z.Phys. C* **45** *(1990) 627*

APPENDIX A
Summary of cuts used

A.1 Electron particle id cuts

A.1.1 Čerenkov signal cut

Denoting with nphe the ECPB variable, i.e. $10x$ number of photoelectrons:

$$nphe > 25$$

A.1.2 Total energy in calorimeter and lower momentum cut

Denoting with p the momentum of the candidates and with E their total energy released in the calorimeter:

$$Ymin \leq E/p \leq Ymax$$

where

$$Ymax = 0.395332 - 0.044357p + 0.0193197p^2 - 0.00272412p^3$$
$$Ymin = 0.137908 + 0.084991p - 0.0245721p^2 + 0.00276102p^3$$

These cuts comes from [18].
Furthermore

$$p >= 0.63884$$

from [12].

A.1.3 Inner - Outer energy in calorimeter cut

A.1.4 Electron fiducial cuts

A.1.5 Proton fiducial cuts

APPENDIX B
Plots of data processing

B.1 Vertex corrections

B.2 Angle corrections

APPENDIX C
Structure functions

APPENDIX D

Effects of M_{1+} dominance and $\ell \leq 2$ approximation

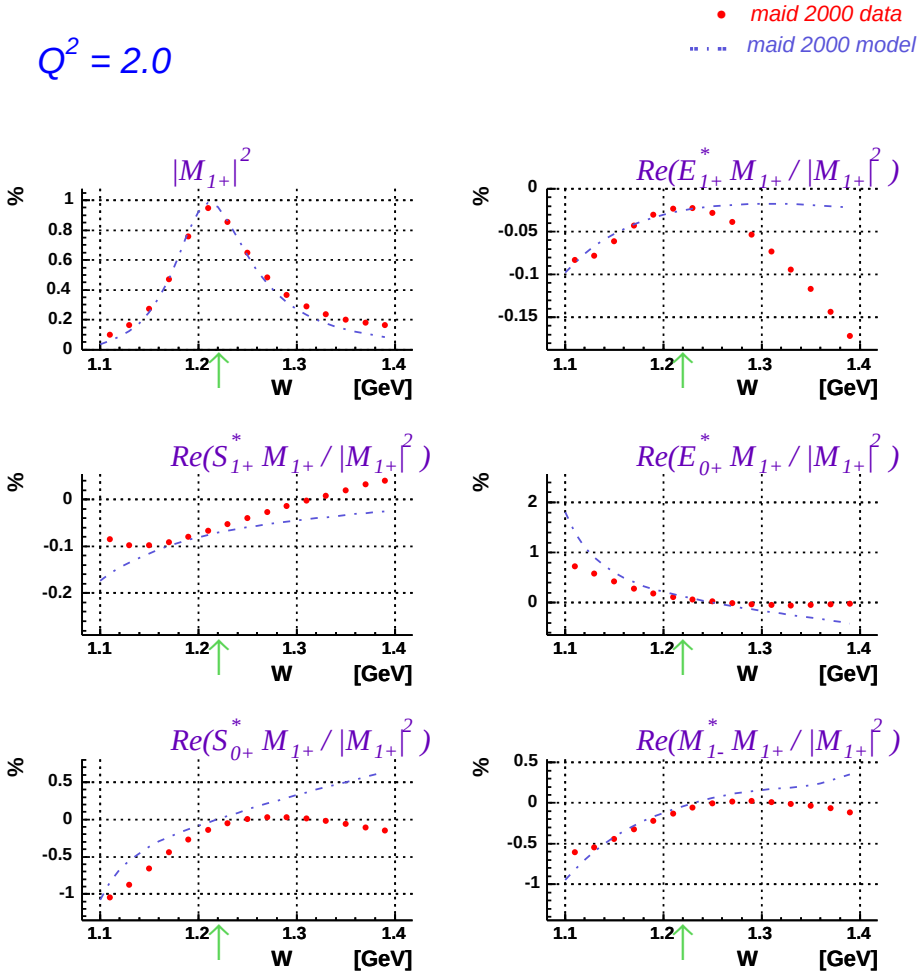

Figure D.1: Comparison between the model / extracted multipoles ratios for maid 2000 at $Q^2 = 2.0$ GeV^2.

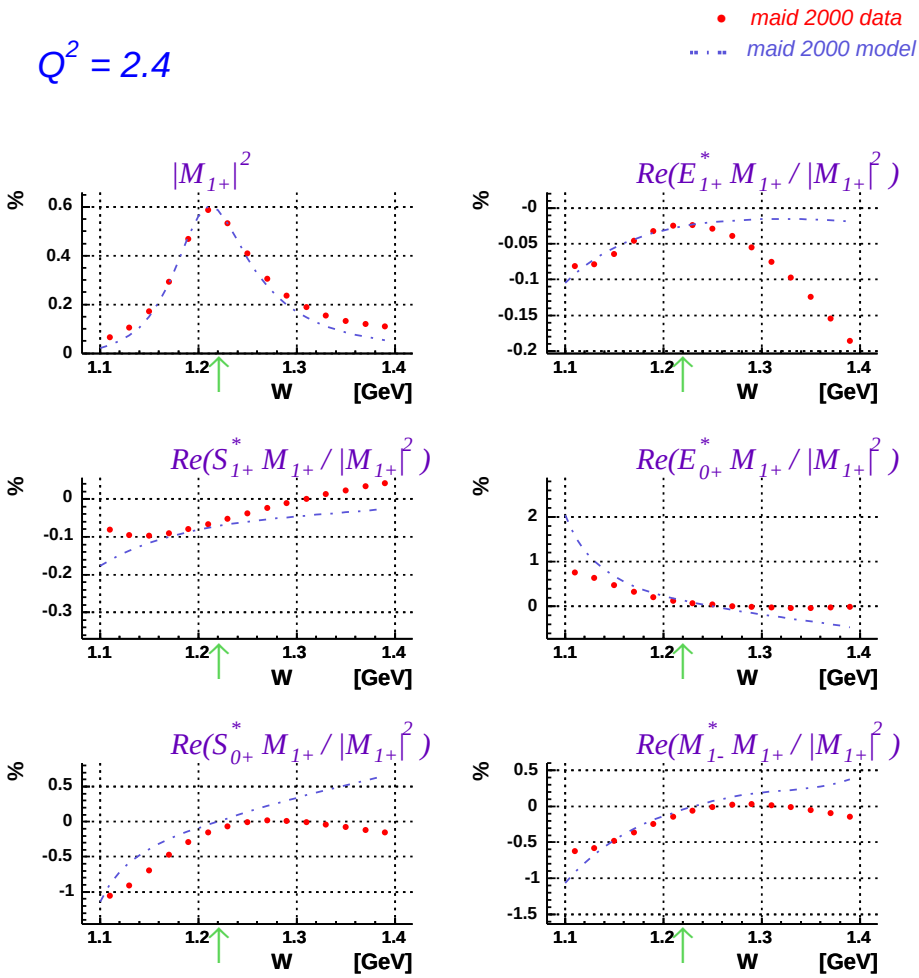

Figure D.2: Comparison between the model / extracted multipoles ratios for maid 2000 at $Q^2 = 2.4$ GeV².

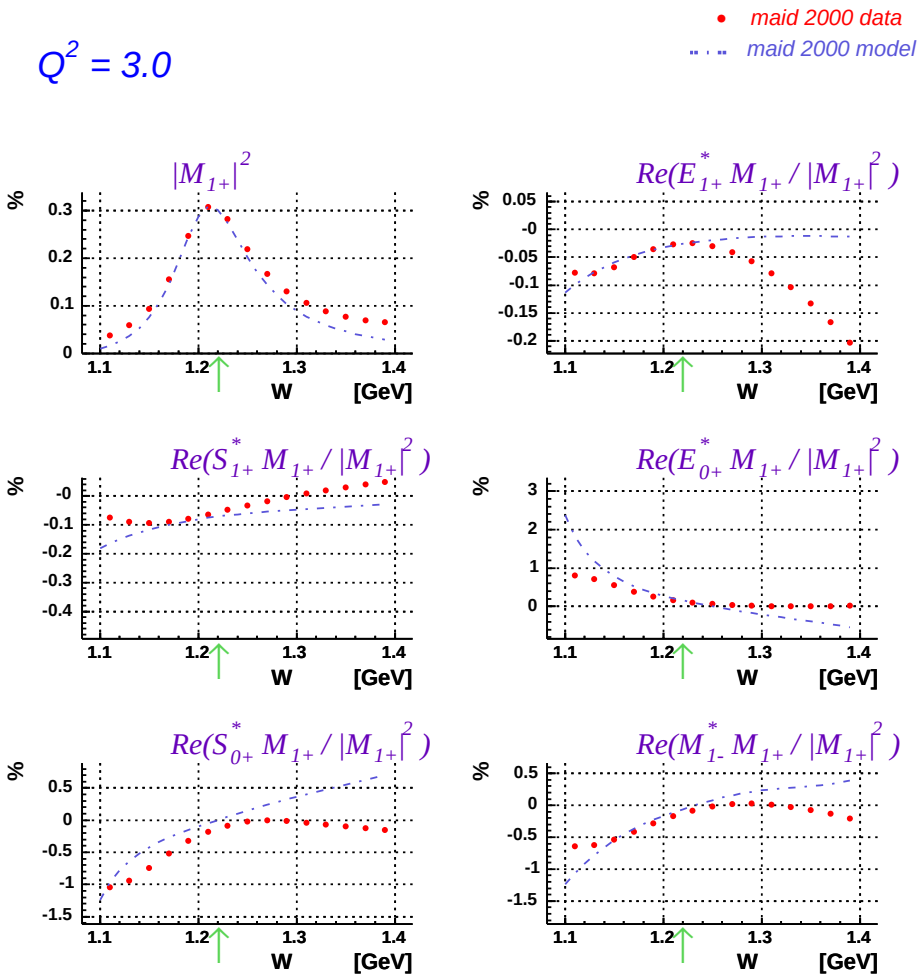

Figure D.3: Comparison between the model / extracted multipoles ratios for maid 2000 at $Q^2 = 3.0$ GeV².

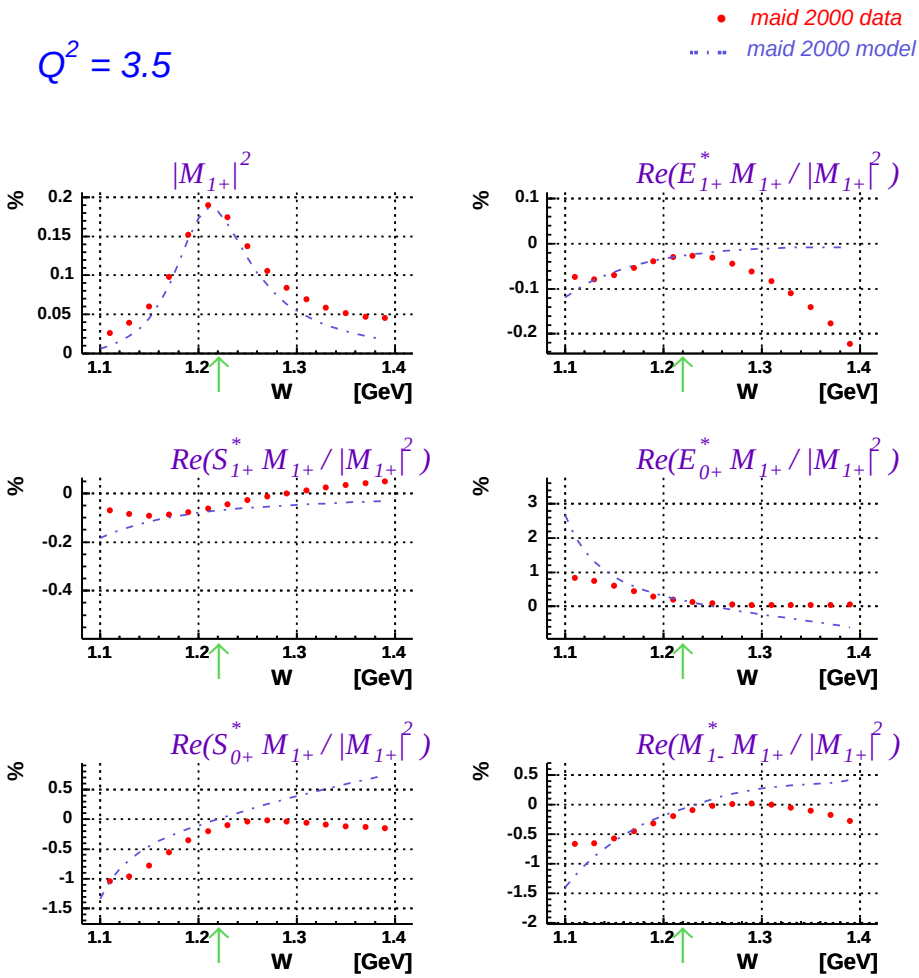

Figure D.4: Comparison between the model / extracted multipoles ratios for maid 2000 at $Q^2 = 3.5$ GeV².

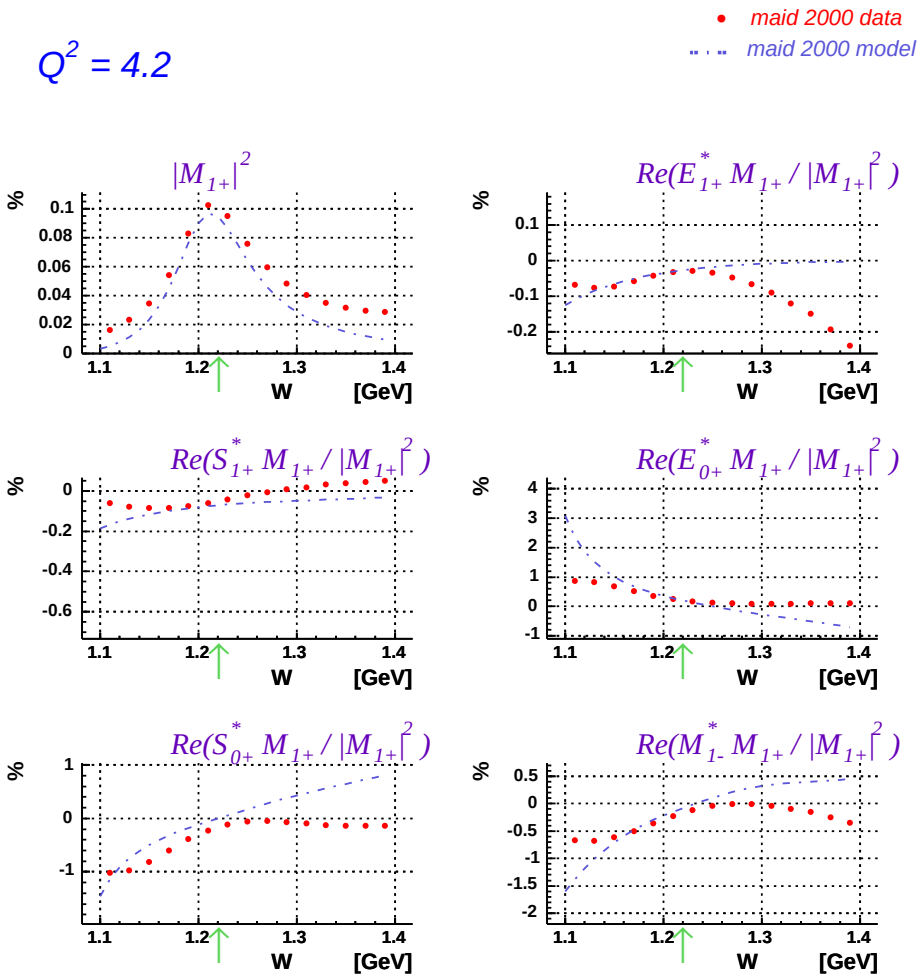

Figure D.5: Comparison between the model / extracted multipoles ratios for maid 2000 at $Q^2 = 4.2$ GeV².

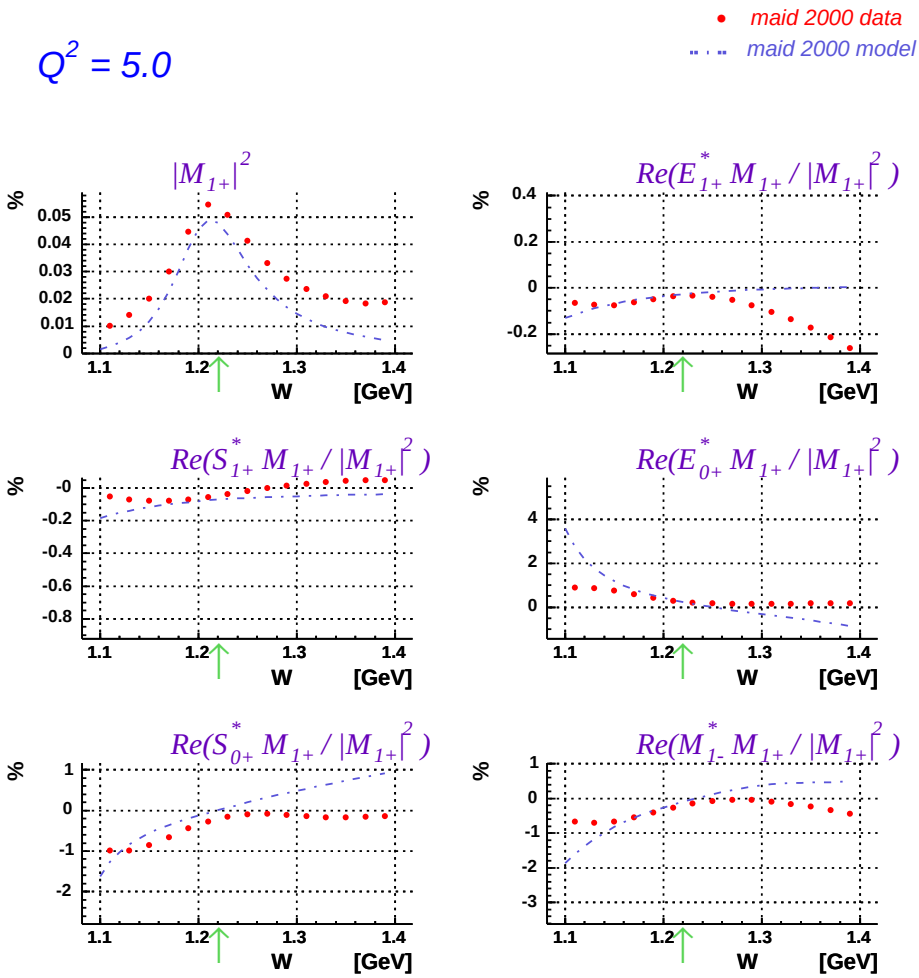

Figure D.6: Comparison between the model / extracted multipoles ratios for maid 2000 at $Q^2 = 5.0$ GeV².

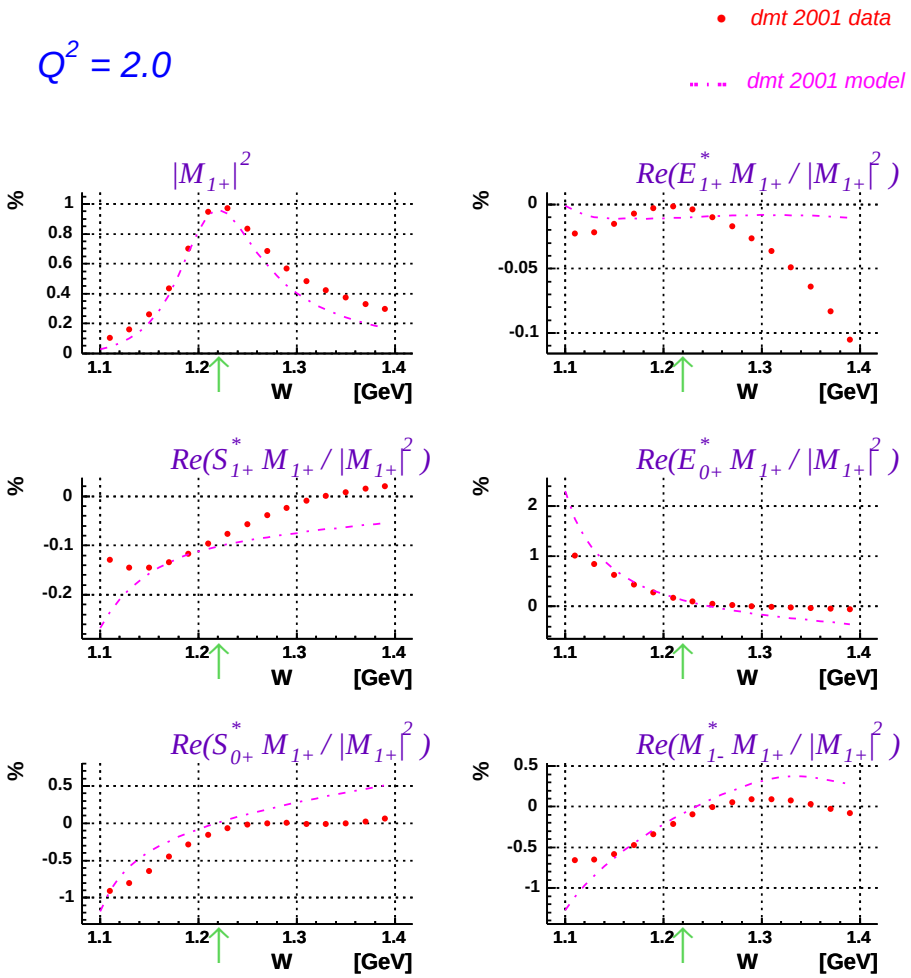

Figure D.7: Comparison between the model / extracted multipoles ratios for maid 2000 at $Q^2 = 2.0$ GeV².

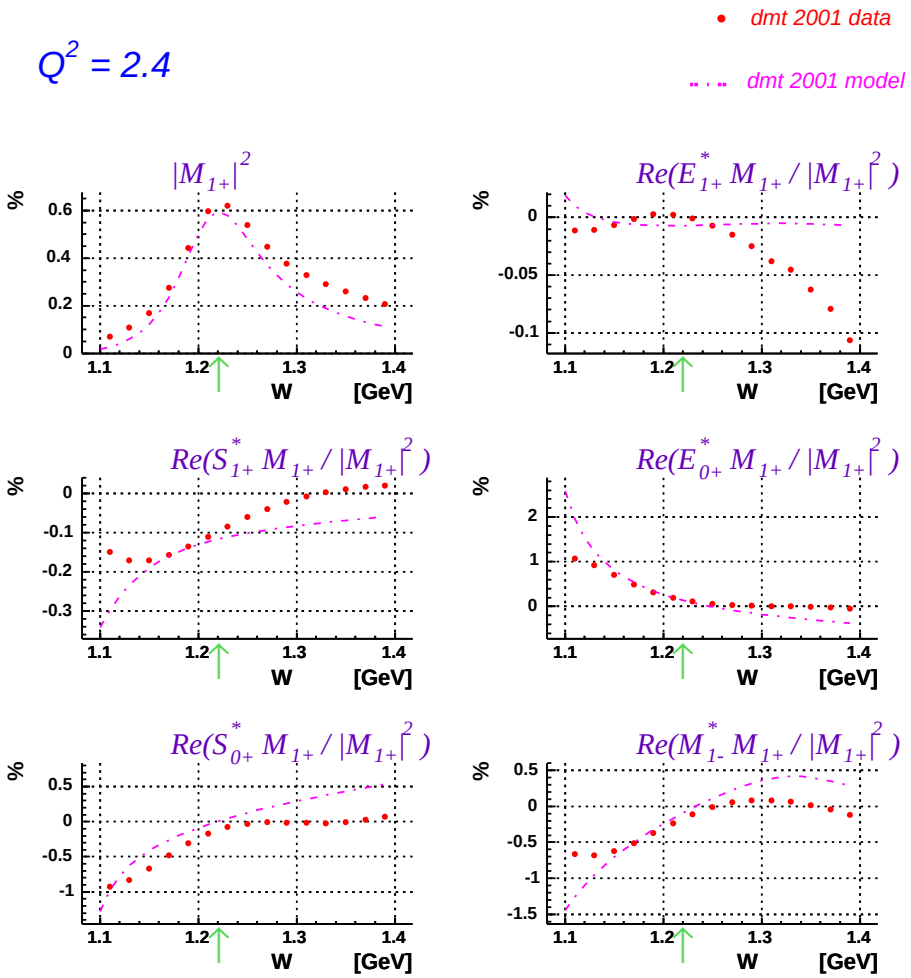

Figure D.8: Comparison between the model / extracted multipoles ratios for maid 2000 at $Q^2 = 2.4$ GeV².

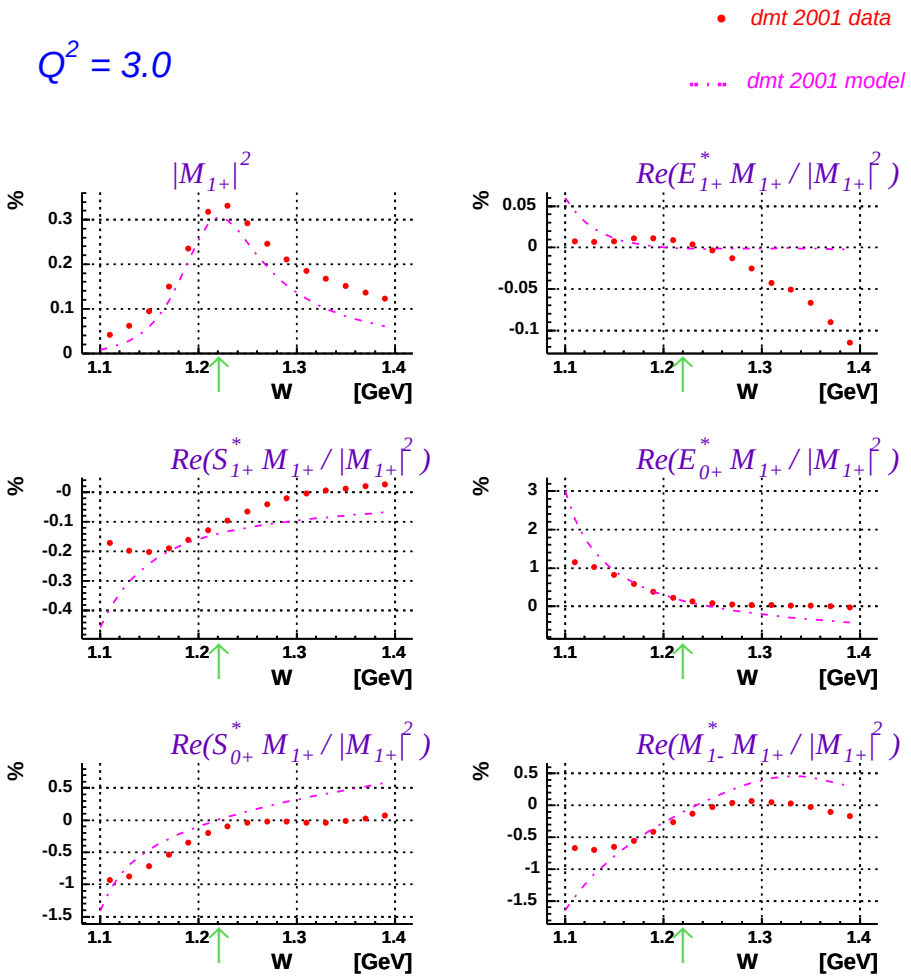

Figure D.9: Comparison between the model / extracted multipoles ratios for maid 2000 at $Q^2 = 3.0$ GeV².

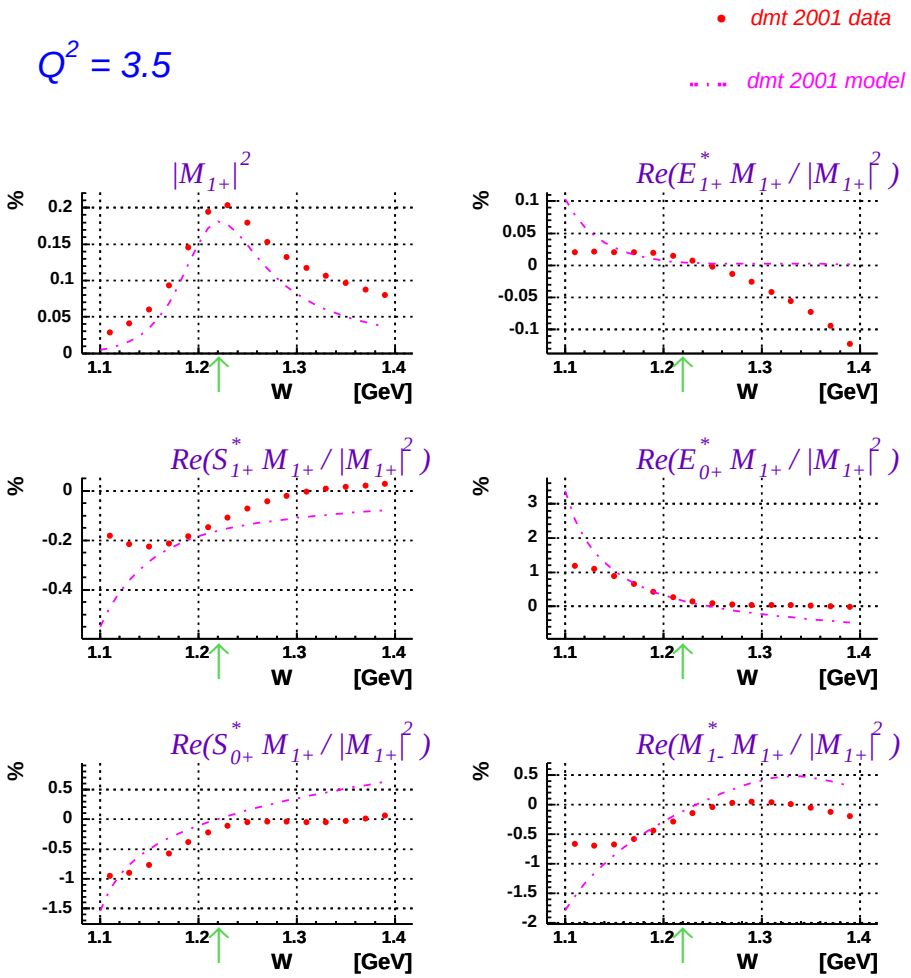

Figure D.10: Comparison between the model / extracted multipoles ratios for maid 2000 at $Q^2 = 3.5$ GeV^2.

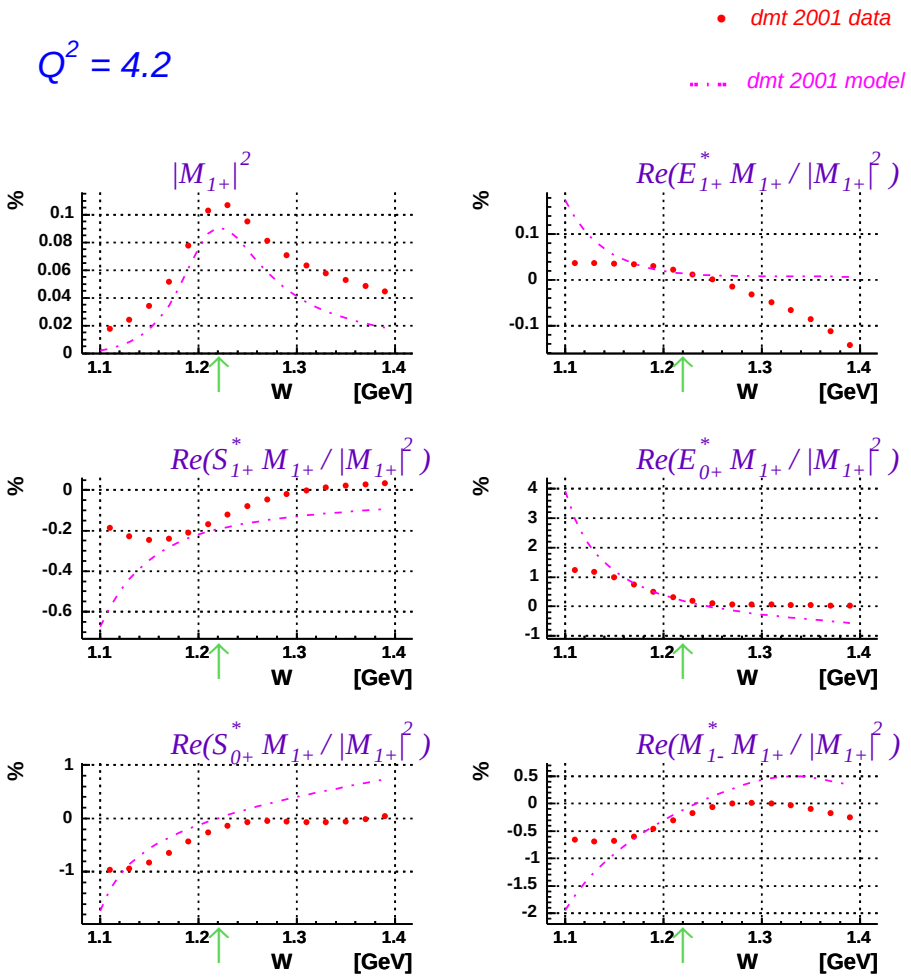

Figure D.11: Comparison between the model / extracted multipoles ratios for maid 2000 at $Q^2 = 4.2$ GeV^2.

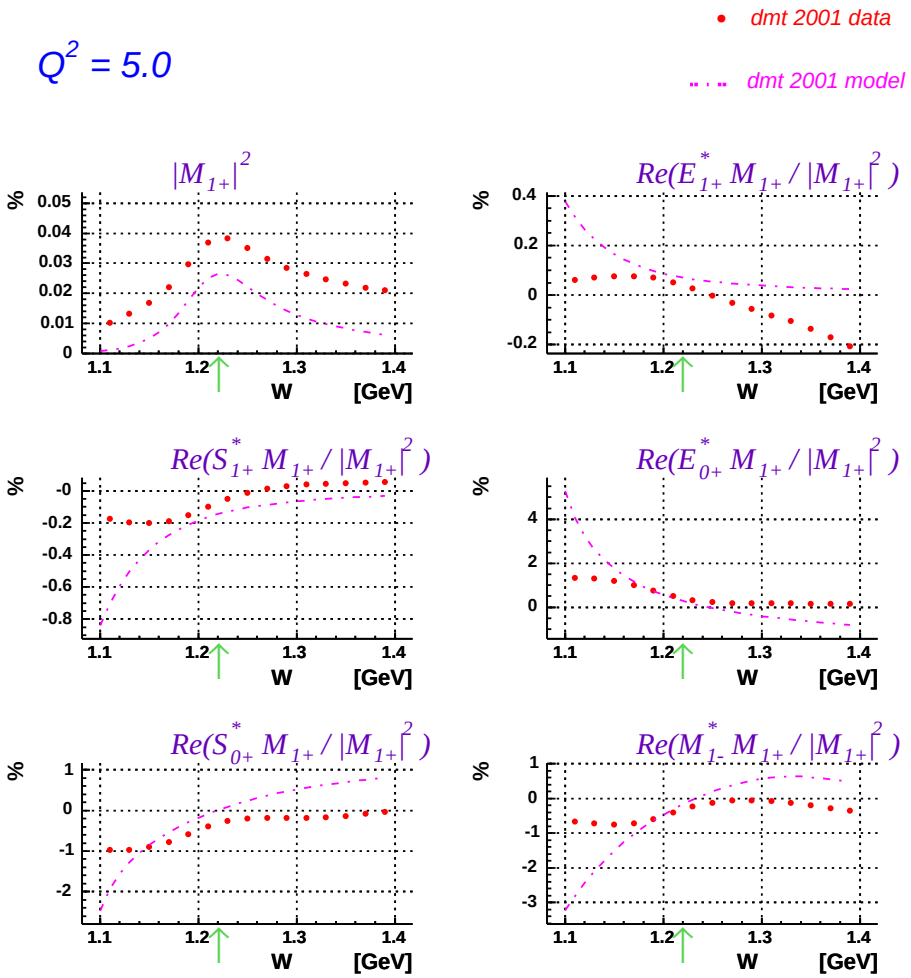

Figure D.12: Comparison between the model / extracted multipoles ratios for maid 2000 at $Q^2 = 5.0$ GeV^2.